DESIGN OF MULTI-AXIAL LOAD CELL TO MEASURE THE FORCES AND MOMENTS ACTING ON ENGINE MOUNTS

by

Kaveh Shahidi

B.S., Mechanical Engineering,

Urmia University , 2009

Submitted to the Institute for Graduate Studies in
Science and Engineering in partial fulfillment of
the requirements for the degree of
Master of Science

Graduate Program in Mechanical Engineering

Boğaziçi University

2014

ACKNOWLEDGEMENTS

First of all, I am grateful to THE ALMIGHTY GOD for letting me to complete this thesis. I would like to thank to my father Kazem, my mother Nazli and my brother and sister, Koosha and Pegah, whom I owe my life and without their self-devotion, continuous support and encouragement I would not be able to achieve my goals. I love you all!

I would like to express the deepest appreciation to my thesis advisor, Assoc. Prof. Nuri Ersoy for his guidance and support throughout my research and thesis. I would also like to thank my co supervisor, Umud Esat Öztürk (CAE Tools and Methods team supervisor at FORD-OTOSAN company), Assoc. Prof. Çetin Yılmaz, Assoc. Prof. Serdar Soyöz and Assist. Prof. Halil Baştürk for sharing their knowledge and taking part in my thesis jury.

In addition, I would like to thank to the Ford Otomotiv Sanayi A.Ş. and the Product Development Powertrain CAD/CAE Department, specially to Lütfi Uçar (Durability CAE Engineer), Onur Zobi (Durability Test Engineer) and Ümit Bağdat (Durability Test Engineer) who have lent their helping hand in this venture and TÜBİTAK for supporting me since March 2013.

I also thank to Yiğit Emre Bilmiş, Berat Kaan Karataş and Emirhan Özkan for their previous work and knowledge which I used throughout this thesis.

I owe my thanks to my dearest colleagues and friends for their friendship, support and encouragement; Ata Sarrafi, Sina Parsnejad, Mahta Zakaria, Ulduz Sobhi Avshar and Hossein Mazaheri who were with me in my both cheerful and tough moments. I also would like to thank all the Composite Lab members specially to Kenan Çinar for his full support and guidance, Fatih Ertuğrul Öz, Onur Yüksel, Yakup Okan Alpay and Anıl Uzal.

ABSTRACT

DESIGN OF MULTI-AXIAL LOAD CELL TO MEASURE THE FORCES AND MOMENTS ACTING ON ENGINE MOUNTS

A new load cell has been designed and manufactured which is able to measure the three components of force and three components of moment. Strain gages are conveniently located on highly stressed areas. The mechanical behavior of the load cell is described by means of Finite Element Method that allow a quick preliminary design focused on the given technical specifications. In order to obtain the final elastic element geometry, several different geometries have been considered for application and analyzed whether if they satisfy strain and stress requirements. Fatigue strength analysis and error analysis of the proposed design alternatives have been carried out in order to provide a load cell which is both simple and is capable of sensitively measuring multi-axial loads along a wide dynamic range of load levels. The load cell has a high accuracy reading capability with a very high degree of decoupling between readings along the respective axes, with a low cross-talk. An accurate, efficient balance calibration system is also designed and manufactured. The load cell is then used successfully in a vehicle to measure the loads acting on engine mounts.

ÖZET

MOTOR YATAĞINA ETKİYEN KUVVETLERİ VE MOMENTLERİ ÖLÇEN ÇOK-YÖNLÜ BİR YÜK HÜCRESİ TASARIMI

Üç Kuvvet ve üç moment bileşenlerinin her birini ölçebilecek yeni bir yük hücresi tasarımı ve imalatı gerçekleştirilmiştir. Gerinim ölçerler yüksek gerilime uğramış bölgelere uygun bir biçimde yerleştirilmiştir. Yük hücresinin mekanik davranışı, belli teknik şartnamelere odaklanılarak hızlı bir ön tasarıma imkan sağlayan, Sonlu Elemanlar Yöntemi ile tanımlanmıştır. Yük hücresinin son elastik eleman geometrisini elde etmek için birçok farklı geometri göz önüne alınmış ve gereken gerinme ve gerilme değerlerini karşılayıp karşılamadıkları analiz edilmiştir. Hem basit, hem de geniş bir dinamik yük aralığındaki çok-eksenli yükleri hassas bir biçimde ölçebilecek yük hücresi yüksek hassasiyette ölçüm yapabilmekte, her bir ekseni çok yüksek düzeyde ayrışmış, çok düşük çapran etkileşime sahip bir şekilde ölçebilmektedir. Aynı zamanda hassas ve etkin bir denge kalibrasyon sistemi tasarlanmış ve imal edilmiştir. Yük hücresi bir aracın motor takozlarına gelen kuvvetler ölçmek içinbaşaralı bir şekilde kullanılmıştır. Bir yük hücresi elde etmek için önerilen tasarım seçeneklerine yorulma dayanımı ve hata analizleri uygulanmıştır.

TABLE OF CONTENTS

LIST OF FIGURES

LIST OF TABLES

LIST OF SYMBOLS

C	Capacitance
C_L	Load factor
C_G	Gradient(size) factor
C_S	Surface factor
C_T	Temperature factor
C_R	Reliability
E	Modulus of Elasticity
M	Moment
R	Resistor
S_y	Yield strength
S_u	Ultimate strength
SF_{yield}	Safety factor against yielding
S_n	Correct endurance limit
S'_n	Endurance limit
ϵ	Strain
ν	Poisson's ratio
σ	Stress

LIST OF ACRONYMS/ABBREVIATIONS

ASTM	American Society for Testing and Materials
BHN	Brinell Hardness Number
CNC	Computer Numerical Control
DOF	Degree of Freedom
FEA	Finite element analysis
FO	Ford Otosan Company
ICP	Integrated circuit piezoelectric sensor
LHS	Left hand side load cell
MATLAB	Multi-paradigm numerical computing environment
NCODE	Software for fatigue and durability solutions
NTEP	National Type Evaluation Program
ODB	Abaqus output database
OIML	International Organization of Legal Metrology
QT	Quench and Tempered Steel
RMSD	Root mean square deviation
RMSE	Root mean square error
RHS	Right hand side load cell
RS-232	Standard for serial communication transmission of data
SAE	Society of Automotive Engineers
SG	Strain Gage
SN-CURVE	Wöhler curve
TEDS	Transducer electronic data sheets
USB	Universal Serial Bus
WEDM	Wire Electro Discharhe Machine

1. INTRODUCTION AND BACKGROUND

1.1. What is a Load Cell

A load cell is a transducer that converts a load acting on it into an electronic signal that can be a change in voltage, current or a frequency depending on the type of the load cell.

Load cells are made using different methods such as inductive, capacitive or resistive. Load cells use different operating principles such as fluid pressure, piezoelectric effect or elasticity. Figure 1.1 shows different types of load cells.

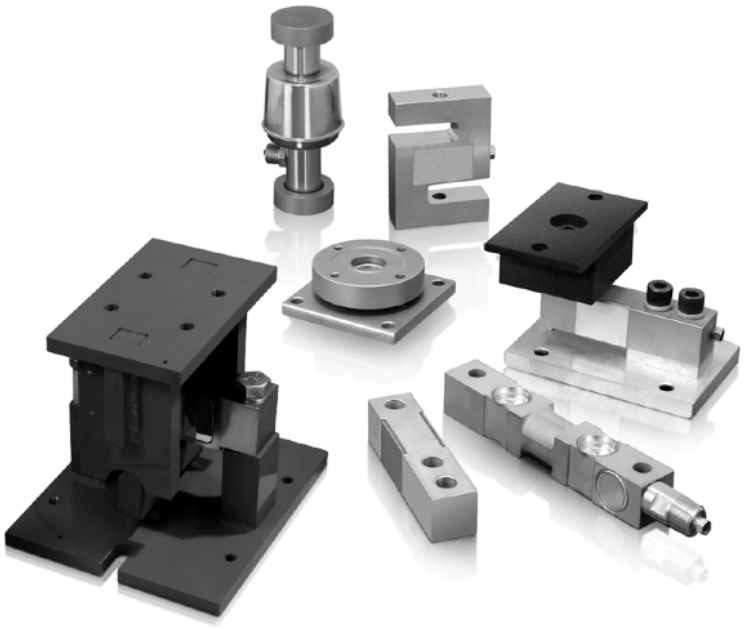

Figure 1.1. Different types of Load-Cells [1].

1.2. Types of Load Cells

Load cells differ according to their types and performance. Overall, load cells can be categorized in three main types, mechanical, strain gage and other. Hydraulic

and pneumatic load cells are examples of mechanical load cells.

Hydraulic load cells operate depending on the principle of balancing a force by a counter force. The force applied on the load cell changes the pressure contained in the device. The magnitude of the unknown force is then obtained through measurement of the change in pressure of the fluid. A schematic of hydraulic load cell is shown in Figure 1.2. The force is applied on the fluid which is mostly oil, contained in a closed chamber, through a thin diaphragm and resulting change in pressure is measured by an appropriate pressure transducer [2, 11, 12]. Output of the sensor is linearly related to applied force. Since there is no electricity required for this type of load cell, hydraulic load cells are preferred for hazardous applications and are considered in remote locations, as they do not require a power supply [13].

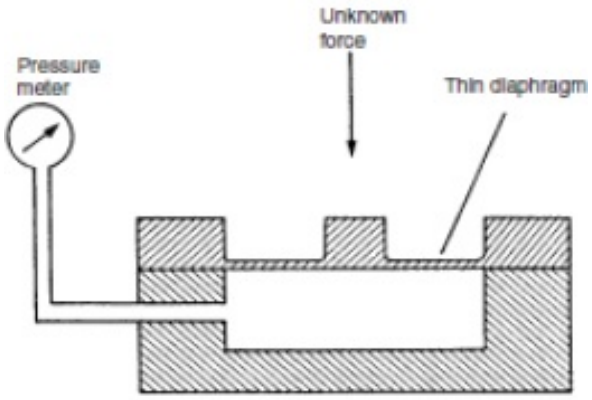

Figure 1.2. Schematic illustration of hydraulic load cell [2].

Similar to hydraulic load cell, pneumatic load cells works on the principle of counter-balance force as well. But this case, instead of oil, air is used inside the chamber. By measuring the change in pressure of air, the magnitude of the unknown force is obtained [2, 13]. Figure 1.3 presents a simplified schematic of a pneumatic force sensor where P_o represents the output pressure and P_s represents the air supply pressure. Pneumatic load cells are sometimes used where intrinsic safety and hygiene are desired.

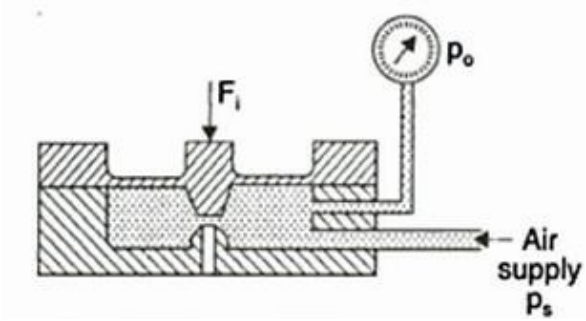

Figure 1.3. Schematic illustration of pneumatic load cell [2].

The working principle of strain gage load cells is based on determining the deformation of an elastic element due to applied force. The deformation of the elastic body is measured through strain gages which give electrical signals as a function of induced strain, caused by the change in resistance of a strain gage. Some of the strain gage load cells are bending beam, shear beam and canister load cells. Strain gage load cells dominate the weighing industry and offer accuracies from within 0.03 to 0.25 % full scale which are suitable for almost all industrial applications. Some of the characteristics of these types of load cells are mentioned below:

(i) Highly precise
(ii) Little influence due to temperature changes
(iii) Small size compared to other types of load cell designs
(iv) Long operating life
(v) Ease in production due to small number of components
(vi) Excellent fatigue characteristics

2. MULTI-AXIAL LOADCELLS : A LITERATURE REVIEW

A load cell is used in order to combine the output signals of strain gages to measure components of an applied load. A multi axis load cell produces multi independent analog outputs. The purpose of this thesis is to design and manufacture a strain gage based load cell having a simple, lightweight physical structure and also being able to function over a wide range of dynamic load levels depending on the dynamic nature of the task being performed. The load cell will be installed in the engine mounts of a vehicle, and will measure the continuous load signals as the vehicle runs on a test track.

An approach to develop force sensors for measuring a six-component load cell has been explained in various related patents and articles [3, 14, 14–21, 21–23] some of which will be briefly discussed in this chapter.

2.1. Patent Review

Load cells for determining loads and moments along axes are discussed in patents [4, 24–28]. The common design of these patents include a central hub connected to an outer ring with bridges or spokes on which various strain gages are installed. In each of the patents the performance and characteristics of the load cell design have been improved.

These load cells have inner and outer members that are joined with bridges on which the strain measuring gages are mounted on. The first of the designs has disadvantages when compared with the latter designs, for example, it only measures moments only about two axes and is not compact like the other designs.

The basic principle of these load cells is that they measure loads and torques along various axes, typically X, Y and Z, with the help of sensors or strain gages

mounted on bridges that connect the outer body of the load cell to the hub in the middle. It is to be noted that in theory, the load along a specific axis will not give an output on any other axes, however in physical tests this is not true and a cross-talk of usually 1-5 % output will be observed and this could add up to 25 % overall. So in order to compensate this cross-talk two different methods are used, the first one being to tune the load cell mechanically or electrically to reduce the cross-talk which is very time consuming and not practical.

The second method involves manipulating the load cells output data mathematically. Applications used in this method are "cross coupling coefficients" and "inverse matrix method". The inventor of these load cells has used the cross coupling method in order to reduce the cross-talk.

When a load is applied to the load cell, the strain gage related to that load will respond accordingly. So by applying different loads and recording each channel's response, an output profile can be created. In the cross coupling method used in the patented designs mentioned above, equations are created to describe the cross talk performance. So eventually by solving these series of equations and using the theory of superposition, the true loading condition is determined.

A description of how this method is used and how the equations come about are explained briefly. A six axis load cell is calibrated by applying a specific load in line with one of the axis. Most multi-axis load cells are used as wheel-force transducers. Multi Axis Load Cells can accurately measure three components of force in three directions and three components of moment about each force direction. These sensors provide multiple bridges that precisely measure the applied force from one of the directions when installed and used according to specifications.

In order to better understand this a free body diagram of a load cell under three forces and three moments along different axes are shown in Figure 2.1.

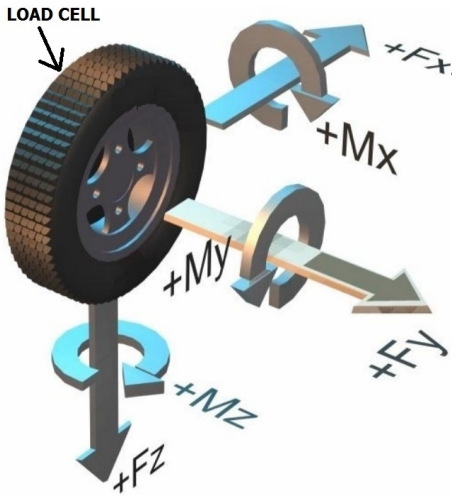

Figure 2.1. A free body diagram of a load cell.

The output received is shown below:

$$O = K_i.F_j \tag{2.1}$$

Function above is the result of this procedure where O, the channel output, is equal to the sensitivity (mV/V per unit load), K_i times the applied load, F_j. This is done for the rest of the five channels. The transfer functions are shown below

$$O_{FX} = K_1.F_X \tag{2.2}$$

$$O_{FY} = K_7.F_Y \tag{2.3}$$

$$O_{FZ} = K_{13}.F_Z \tag{2.4}$$

$$O_{MX} = K_{19}.M_X \tag{2.5}$$

$$O_{MY} = K_{25}.M_Y \tag{2.6}$$

$$O_{MZ} = K_{31}.M_Z \tag{2.7}$$

By dividing the output by the load the transfer function for each channel will be determined. By using the superposition method, the transfer functions are combined to yield the output equations.

$$O_{FX} = K_1.F_X + K_2.F_Y + K_3.F_Z + K_4.M_X + K_5.M_Y + K_6.M_Z \tag{2.8}$$

$$O_{FY} = K_7.F_X + K_8.F_Y + K_9.F_Z + K_{10}.M_X + K_{11}.M_Y + K_{12}.M_Z \tag{2.9}$$

$$O_{FZ} = K_{13}.F_X + K_{14}.F_Y + K_{15}.F_Z + K_{16}.M_X + K_{17}.M_Y + K_{18}.M_Z \tag{2.10}$$

$$O_{MX} = K_{19}.F_X + K_{20}.F_Y + K_{21}.F_Z + K_{22}.M_X + K_{23}.M_Y + K_{24}.M_Z \tag{2.11}$$

$$O_{MY} = K_{25}.F_X + K_{26}.F_Y + K_{27}.F_Z + K_{28}.M_X + K_{29}.M_Y + K_{30}.M_Z \tag{2.12}$$

$$O_{MZ} = K_{31}.F_X + K_{32}.F_Y + K_{33}.F_Z + K_{34}.M_X + K_{35}.M_Y + K_{36}.M_Z \tag{2.13}$$

These equations describe the outputs in terms of the loads applied. The unknowns are the loads which can be found by solving this set of linear equations.

A patent [3] has been issued on a six component load cell that is capable of measuring all six components simultaneously. This design shown in Figures 2.2 and

2.3 has a sensing unit for measurement which consists of an upper and a lower ring, which individually have connectors, locking hole and other parts yet are connected to each other making a single block load cell. The measurement unit has a beam in the shape of a cross, which has both vertical and horizontal slots. Strain gages are mounted on the cross shaped beam as shown in Figure 2.2. It is to be noted that the slots reduce the error of bending moment components to a value of 2 % and less.

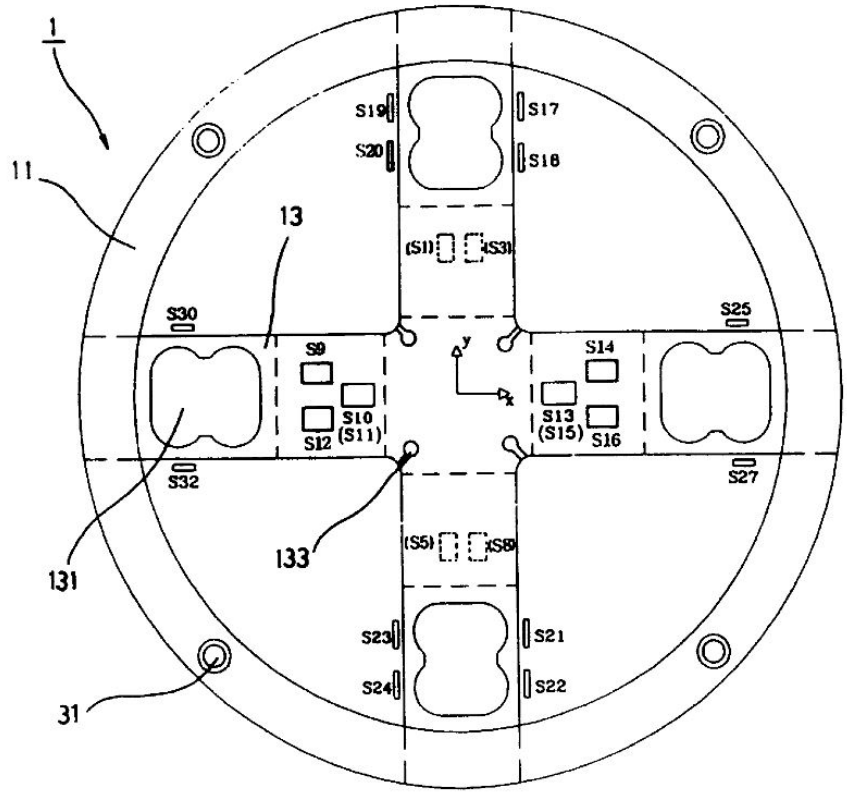

Figure 2.2. A perspective view of the load cell [3].

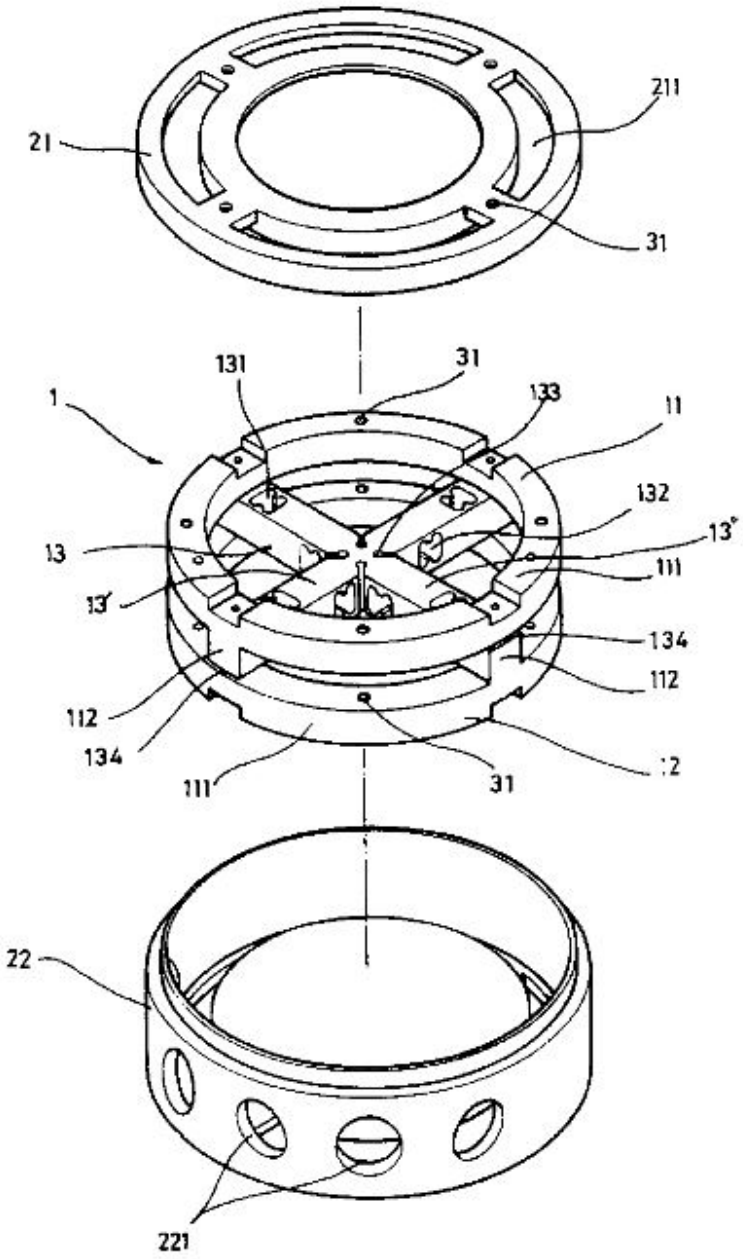

Figure 2.3. A representation of the design load cell with upper and outer cases [3].

Figure 2.4 shows one of the bridges along in which loads are applied. Figure 2.5 is a perspective view of the load cell with 8 strain gages.

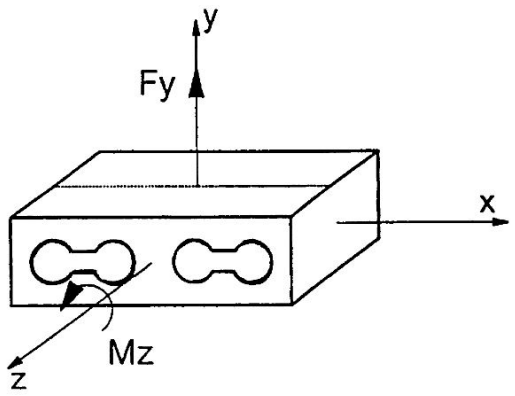

Figure 2.4. The axis along in which loads are applied [3].

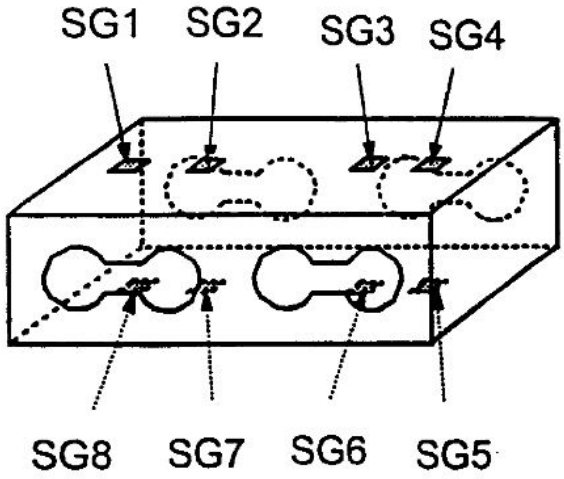

Figure 2.5. A perspective view of the sensing unit of the load cell with 8 strain gages [3].

Table 2.1 shows the position of sensitive strain gages corresponding to the forces and moments. Strain gages 1, 4, 5 and 8 are used for sensing the force F_y, while the strain gages 2, 3, 6 and 7 are used for sensing the moment M_z. The output signals F_y

and M_z are expressed as follows:

$$F_y : E_o/E_i = K/4(SG1 - SG5 + SG4 - SG8) \tag{2.14}$$

$$M_z : E_o/E_i = K/4(SG2 - SG3 + SG6 - SG7) \tag{2.15}$$

Where K is a constant. In the F_y load cell, the force F_y results in an output signal E_o/E_i of 500 $\frac{\mu.m}{m}$, while the moment M_z results in an output signal E_o/E_i of 0 $\frac{\mu.m}{m}$. In this way the signals due to F_y and M_z can be separated.

Table 2.1. The position of strain gage.

	e1	**e2**	**e3**	**e4**
F_x	S19	S17	S24	S22
F_y	S30	S32	S25	S27
F_z	S11	S10	S15	S13
M_x	S1	S5	S3	S8
M_y	S9	S14	S12	S16
M_z	S20	S23	S21	S18

Figure 2.6 shows a design of a wheel force load cell [4], which is suited to be installed and used on light commercial automobiles but not on large vehicles such as trucks. The reason for this is due to the large diameter of the spindle where it leaves out a small space between the tire rim and the spindle.

Some of the advantages and disadvantages of this design have been mentioned accordingly. The wall portions where the strain gages are mounted have been thinned down to a certain degree in order to have a concentrated stress therein, also the load cell has been manufactured from a single body block which is a good advantage as well, but the patents don't seem to give specific detail in regards to this thickness reduction made. No frequency and fatigue test has been done on the load cell and no information has been given regarding accuracy. Basically what the design has concentrated more on is the simplicity of the design rather than the output data.

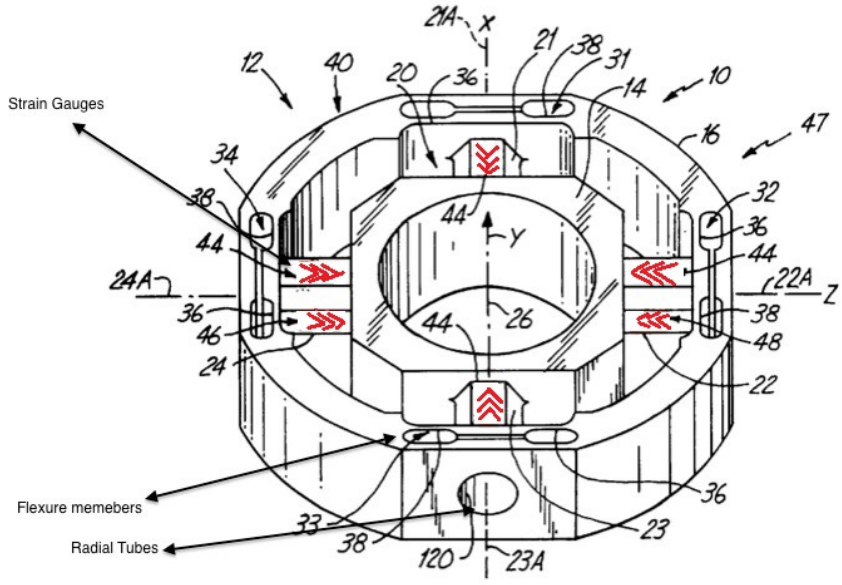

Figure 2.6. Top plan view of the load cell mounted to a tire rim [4].

Patent [5] shows a multi-axial load cell which has both inner and outer members that are connected by arms and are integral with the inner member and connected with the outer member. The loads are sensed when these arms are bent. The load cell is shown in Figure 2.7. The procedure of measurement of this load cell is the same as the load cells mentioned above.

Figure 2.8 illustrates an embodiment of this load cell. The position of the strain gages can be seen in this image. The strain gages used are designated with letters and numbers. The first letter “C” or “T” stands for compression and tension. The next letters stand for the axis which the measurement is done on X, Y, Z or M, that is, moment about the “Y” axis . The third letter indicates the tool end (A) or base end (B), and the numeral at the end shows the quadrant of the radial arm on which the strain gage is placed. This load cell is specifically designed to be used in tire testing machines.

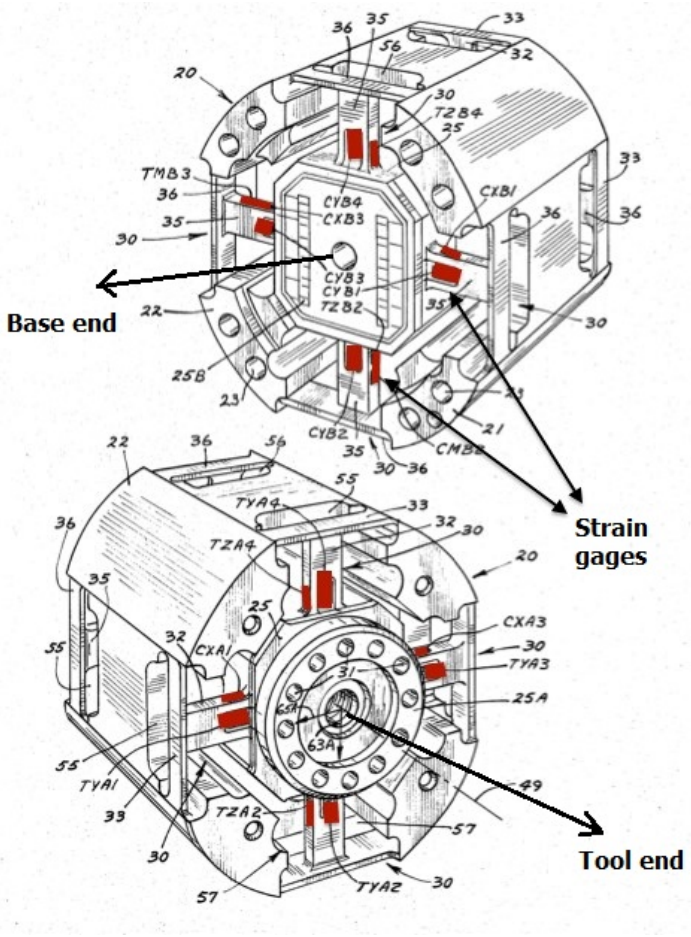

Figure 2.7. Perspective views of the multiple axis load sensitive transducers [5].

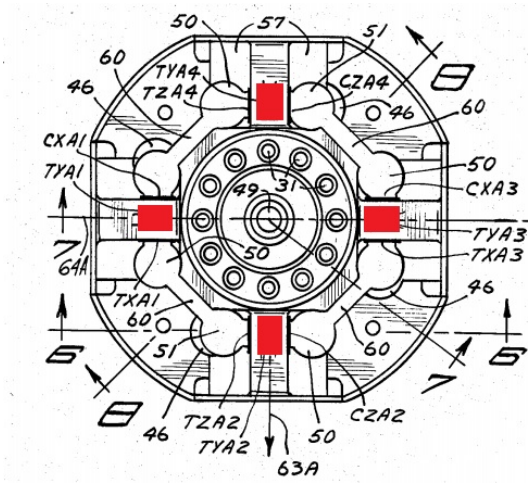

Figure 2.8. An embodiment of the load cell [5].

The strain gages for loads along X and Z axes, as well as those for loads along the Y axis are positioned at both ends of the load cell. This permits the determination of the average load along these axes and moments about the axes as well. The basic forces involved are F_y, which is independent of other outputs, and M_y which is also independent of other outputs and is not cross coupled. The moments about the Z and X axes and also the forces along them are calculated with the following equations:

$$M_z = (F_{AX} - F_{BX}).H \tag{2.16}$$

$$M_X = (F_{AZ} - F_{BZ}).H \tag{2.17}$$

$$F_X = \frac{F_{AZ} + F_{BX}}{2} \tag{2.18}$$

$$F_Z = \frac{F_{AZ} + F_{BZ}}{2} \tag{2.19}$$

Cross coupling occurs in moments about X and Z axis, it also occurs on forces along X and Z axis, however the slots minimize the cross coupling effects.

Several strain gages are placed on bridges, so in order to obtain the signals from these strain gages, Wheatstone bridges are formed as shown in Figure 2.9 and represented by R1-R4.

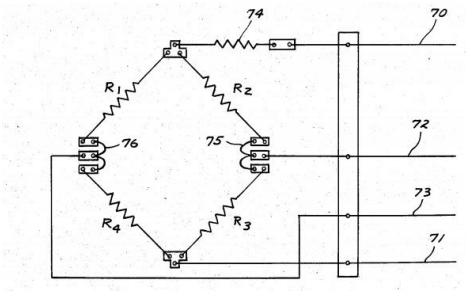

Figure 2.9. Wheatstone bridge to obtain output signals from strain gages [5].

The individual outputs from the bridge provides signals that indicate the various forces determined from loads and moments. Two strain gages for determining the force along Y axis are used on each arm to from the four arm bridge. It should be noted that both the tension and compression gages are in opposite arms of the bridge. Table 2.2 shows each of the individual bridges used with the strain gages corresponding to the respective resistors in order to obtain the output:

Table 2.2. Bridge outputs for forces and moments.

	Strain Gage Number					
Resistor	**Bridge Output equals F_{AX} X axis force at Tool end)**	**Bridge Output equals F_{BX} (X axis force at Base end)**	**Bridge Output equals F_{AZ} (Z axis force at Tool end)**	**Bridge Output equals F_{BZ} (Z axis force at Tool end)**	**Bridge Output equals F_Y (Y Axis Force)**	**Bridge Output equals M_Y (Moment about Y axis)**
R_1	TXA1	TXB1	TZA2	TZB2	TYA1 and TYA4 (In Series)	TMB1
R_2	CXA1	CXB1	CZA2	CZB2	CYB4 and CYB1 (In Series)	CMB2
R_3	TXA3	TXB3	TZA4	TZB4	TYA3 and TYA2 (In Series)	TMB3
R_4	CXA3	CXA3	CXB3	CZB4	TYA1 and TYA4 (In Series)	CMB4

Figures 2.10 and 2.11 show another design of load cell [6]. Strain gages are attached to the force sensing bridges in a way that at least one strain gage provides an output signal related to the force applied. The components of the load cell are expressed in a Cartesian or other coordinate system without needing to decouple the force components within the load cell. So it is designed in a way to overcome this decoupling problem.

Each strain gage has an output of only one component. So six output voltages are necessary, each one corresponding to the force or moment along or about one of the three axes.

The structure is simple in design, however the disadvantage of this load cell is that the shear strain gages and the extensional gages are mounted to the same beams as shown in Figure 2.10, which results in the trade off of gage sensitivity between them.

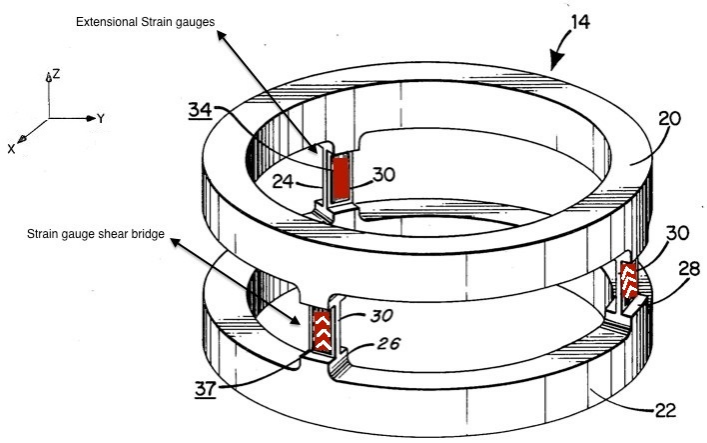

Figure 2.10. A simplified representation of the design load cell [6].

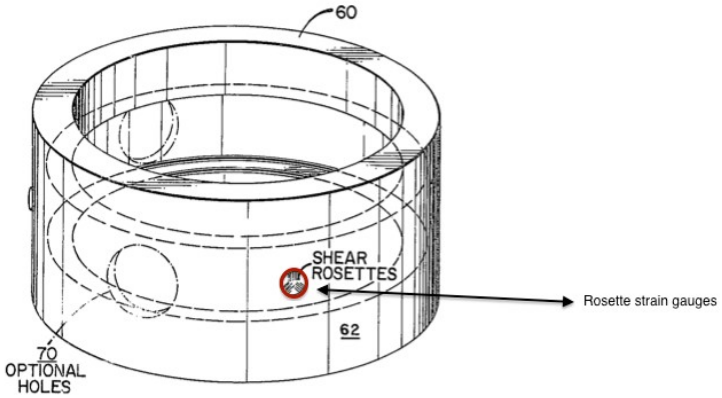

Figure 2.11. An embodiment of the load cell showing rosettes placed 120 degrees apart [6].

In Figure 2.10 the locations of strain gages on the bridges are shown. A unidirectional force F_x is applied to the load cell in x direction through the upper plate. Similar goes for forces and moments in other directions. As shown in Figure 2.11 three strain gage rosettes are placed 120 degrees apart. The rosettes are connected to yield two outputs each, shear and longitudinal extensions.

Figure 2.12 shows circuit diagram of the load cell which contains six strain gages. The output voltages V_1 through V_6 from these strain gages are applied to preprocessing electronics which convert each of the strain gage analog outputs into a digital representation for further processing.

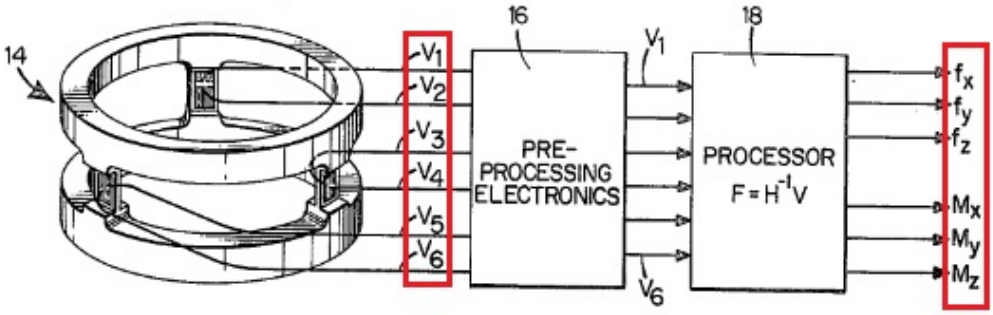

Figure 2.12. An embodiment of the load cell showing output voltages from strain gages [6].

After applying superposition to the strains output data resulting from input loads, the following matrix equation is written:

$$\{V\} = [H]\{F\} + \{B\} \tag{2.20}$$

Where {V} equals the output voltage vector, [H] is the transfer matrix, {F} equals the input force vector, and {B} is a vector representing any biases, for example resulting from gravity, or offsets in the load cell outputs.

When there are six strain gages, Equation 2.20 takes the form:

$$\begin{bmatrix} v_1 \\ v_2 \\ \dots \\ v_6 \end{bmatrix} = \begin{bmatrix} h_{11} & \dots & h_{16} \\ \dots & & \dots \\ h_{61} & \dots & h_{66} \end{bmatrix} \begin{bmatrix} f_1 \\ f_2 \\ \dots \\ f_6 \end{bmatrix} \tag{2.21}$$

In this case f_1 through f_6 are F_X, F_Y, F_Z and moments M_X, M_Y and M_Z. By calculating the inverse of the matrix [H], force from voltage readings can be determined:

$$\{F\} = [H]^{-1}(\{V\} - \{B\}) \tag{2.22}$$

When all six input loads $\{F_i\}$ have been applied and the corresponding $\{V_i\}$ recorded, they are then combined into a matrix [O] by grouping the six vectors $\{V_i\}$ into the columns O:

$$[O] = [\{V_1\}\{V_2\}...\{V_6\}] \tag{2.23}$$

and a matrix [L] by grouping the six vectors $\{F_i\}$ into the columns of [L] in the same order as the vectors $\{V_i\}$ form [O]:

$$[L] = [\{F_1\}\{F_2\}...\{F_6\}] \tag{2.24}$$

Then the following equation is written:

$$[O] = [H][L] \tag{2.25}$$

Since matrix [L] is a square matrix of 6x6, thus matrix [H] can be solved by:

$$[H] = [O][L]^{-1} \tag{2.26}$$

In this case matrix [L] takes the simple form:

$$[L] = \begin{bmatrix} f_1 & 0 & 0 & 0 & 0 & 0 \\ 0 & f_2 & 0 & 0 & 0 & 0 \\ 0 & 0 & f_3 & 0 & 0 & 0 \\ 0 & 0 & 0 & f_4 & 0 & 0 \\ 0 & 0 & 0 & 0 & f_5 & 0 \\ 0 & 0 & 0 & 0 & 0 & f_6 \end{bmatrix} \tag{2.27}$$

The values h_{11} through h_{61} of matrix [H] may then be easily determined by dividing each element of vector $\{V_1\}$ by f_1 and the same for the rest and so on.

2.2. Article Review

A new type of wrist load cell is presented by Chao and Chen [7]. The design shown consists of a cross member with sliding and rotating boundary conditions connected with the rigid rim as shown in Figure 2.13.

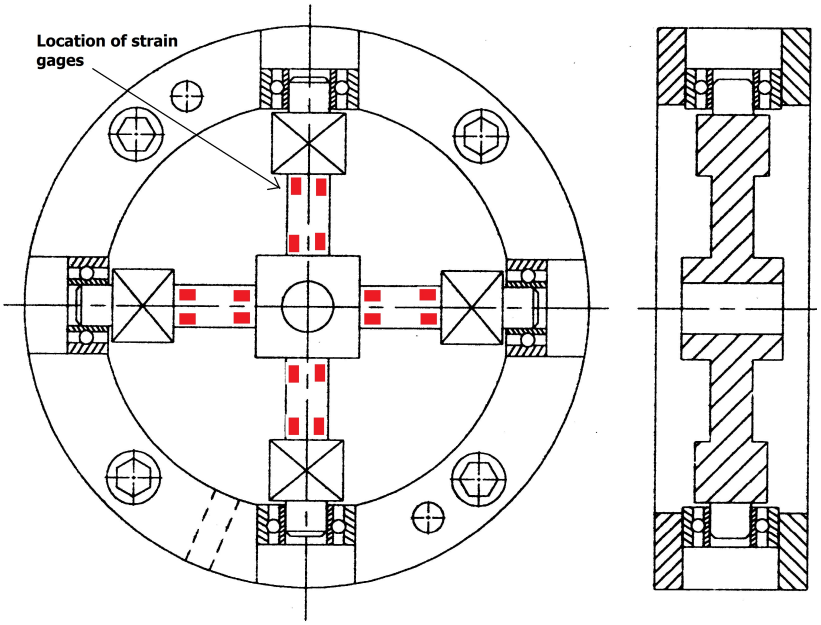

Figure 2.13. The assembly drawing of the novel six-axis wrist force sensor [7].

This design uses a new methodology which is employing a calibration matrix to decouple the load cell. The ball-bearings at the end of the bridges allow a flexibility condition at the rim, which causes the stress to decrease, and that results in an excellent decoupled calibration matrix. The bearings provide free rotation and sliding of the arms, which cause a reduction in cross coupling terms.

The method used is the "Inverse Matrix" method which is a technique that inverts the equations so that instead of having the outputs as a function of loads as described in the beginning of this chapter, the loads are in fact functions of the outputs. This theory is used in the decoupling of the load cell designed in this thesis.

The inverse matrix theory is used to compensate the outputs due to cross-talk errors. It involves gathering the measured data on the strain gages and using it to construct a matrix that can be used for identifying the true condition of the loading. We have a series of N equations, each with N variables as shown below:

$$O_1 = K_1.X_1 + K_2.X_2 + ...K_N.X_N \tag{2.28}$$

...

$$O_N = K_1.X_1 + K_2.X_2 + ...K_M.X_N \tag{2.29}$$

Where O_1-O_N are outputs and K_1....K_N are sensitivities and X_1-X_N are load components. By putting these equations in to matrix format we will have:

$$\{O\} = [\mathbf{K}].\{X\} \tag{2.30}$$

where

$$\{\mathrm{O}\}= \begin{bmatrix} O_1 \\ ... \\ O_N \end{bmatrix}$$

$$[\mathrm{K}]= \begin{bmatrix} K_1 & ... & K_N \\ ... & & \\ K_l & ... & K_M \end{bmatrix}$$

$$\{\mathrm{X}\}= \begin{bmatrix} X_1 \\ ... \\ X_N \end{bmatrix}$$

So when solved for {X} the equation takes the form:

$$\{X\} = [\mathbf{K}]^{-1}.\{O\} \tag{2.31}$$

where $\{K^{-1}\}$ is the inverse of the matrix {K}, and when the inverse matrix is multiplied by the output set, the result is the solution to the variable matrix X.

For the design proposed in Ref [7] the decoupling degree of the calibration matrix depends on the structure of the sensor body and on the total number of strain gages. Figure 2.13 shows the body of the design and 16 strain gages (shown in red) that are glued along the center lines on the sides of each of the four beams. Overall, eight Wheatstone bridges are needed so that the load cell can register strains corresponding to different loading conditions. In the force vector $\{\mathrm{F}\} = (F_x, F_y, F_z, M_x, M_y, M_z)$ the forces and moments are measured by 16 strain gages at given points on the elastic body, yielding the strain signal vector $\{\epsilon_s\} = (\epsilon_1, \epsilon_2, ..., \epsilon_n)$. Vectors F and ϵ_s are related by:

$$\{\epsilon_s\} = [C]\{F\} \tag{2.32}$$

Where [C] is an 6x6 strain matrix. When $\{\epsilon_s\}$ contains six elements, the solution for

F is:

$$\{F\} = [C]^{-1}\{\epsilon_s\} = [B]\{\epsilon_s\} \tag{2.33}$$

The Moore-Penrose inverse techniques can be employed to determine F.

$$\{F\} = [B]\{\epsilon_s\} = ([C]^T[C])^{-1}.[C]^T\{\epsilon_s\} \tag{2.34}$$

The article written by Joo, Na and Kang [8] introduces a new design and evaluation of a six-component load cell. A ring-type structured load cell has been designed using a parallel plate structure as the basic sensing element which can be used for measuring the force component, F_y, and moment M_y and T_y as shown in Figure 2.14. Then the investigation continues on a double Parallel Plate Structure (PPS) as shown in Figure 2.15.

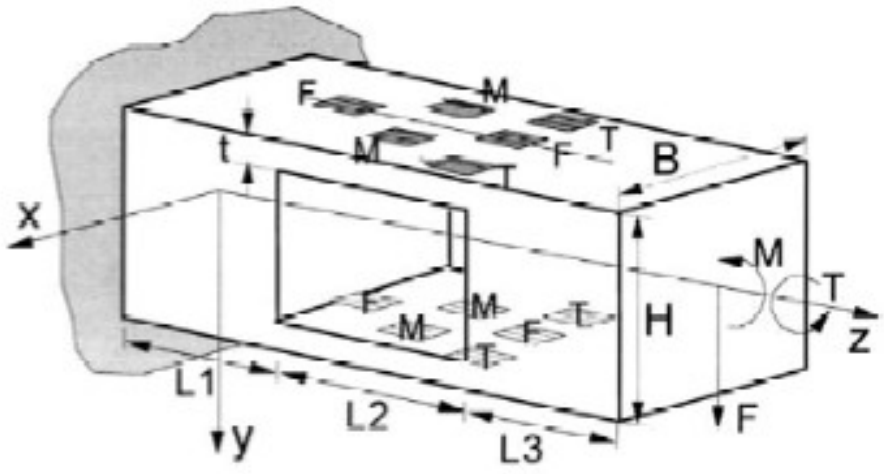

Figure 2.14. Shape of a single parallel plate structure (PPS) and the positions of strain gages for measuring three components of force and moments [8].

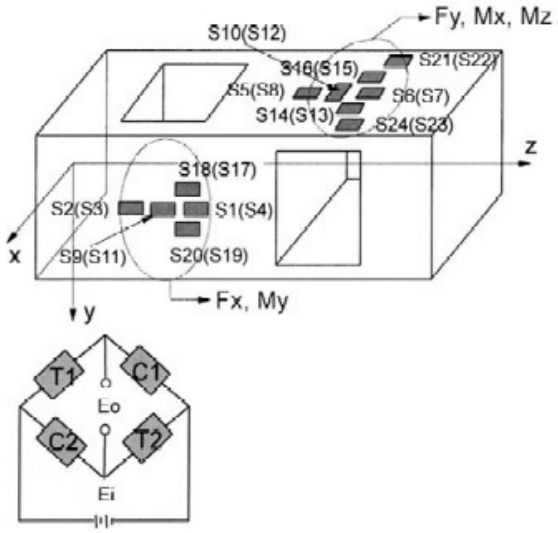

Figure 2.15. Double PPS, position of strain gages and the Wheatstone bridge circuit for measuring six-component force and moments [8].

As we can see from the image above the PPS could be used to measure F_x and M_y, and to measure F_y, M_x and M_z. Table 2.3 shows active strain gages for tension (T) and compression (C) corresponding to a particular load component.

Table 2.3. Active strain gages for tension (T) and compression (C).

	F_x	F_y	F_z	M_x	M_y	M_z
T_1	S1	S5	S9	S13	S17	S21
C_1	S2	S6	S10	S14	S18	S22
T_2	S3	S7	S11	S15	S19	S23
C_2	S4	S8	S12	S16	S20	S24

Also a finite element analysis has been performed to find the locations where the strain gages are meant to be placed as well as calibration test in order to evaluate sensitivities, coupling error and nonlinearity errors have been performed. The finite element mesh can be seen in Figure 2.16.

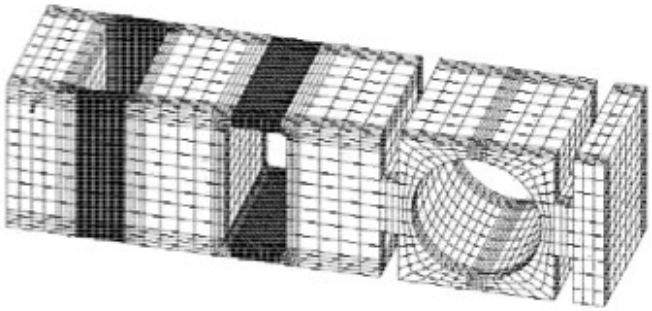

Figure 2.16. Finite element mesh of the final model [8].

The main advantage of this load cell is the weight of it being much lighter than other designs. In order to minimize coupling errors the location of the strain gages have been determined using Finite Element Analysis. A strain measurement has been done for all six component of forces and moments which has reduced coupling behavior errors to 3.8 % which shows that the six-component load cell developed in this study has good performance.

2.3. Problem Statement

Considering the previous works one can see that there are not enough experimental studies in this field and in some limited cases which use experimental methods, the results have not been compared to those obtained from numeric and algorithmic analysis. Physical testing has not been done and in most cases designs have been based purely on theoretical studies. In some cases mechanical structures including various hinges, pivots, or other mechanisms have been used in order to decouple the force components and to permit them to be measured independently from one another [29]. Such mechanical structures are complex to manufacture, and require precise accuracy in dimensions and components to accurately decouple the individual force components. Accordingly, such structures are costly to manufacture and maintain.

The objective of this thesis is to design a multi-axis load cell that is simple in

design and also it should be capable of sensitivity measuring multi-axis loads along a wide dynamic range of load levels and necessary to have a high accuracy reading capability with a very high degree of decoupling between readings along different axes. It should also have a low cross-talk and an accurate, efficient balance calibration system that is inexpensive to manufacture.

Two types of load cells have been designed in this thesis. The first design has been manufactured and tested on a vehicle. The second design is an optimized version of the first one with slots added in order to reduce the crosstalk between the measuring channels and strain gage mounting errors. Also, considering that these load cells are aimed to be used in dynamic load applications, a fatigue analysis is performed in order to assess the durability of the structures.

This thesis is a part of a university-industry collaborative project between Ford Otomotive Sanayi A.Ş. (FORD-OTOSAN) and Boğaziçi University, in the context of a TÜBİTAK TEYDEB 1501 funded project (No 3110258). Within the context of this project, a load cell was designed that was used as a sensor to measure the loads acting on the engine mounts of a engine in the development stage. The load cell was then manufactured and calibrated in the laboratory, an then installed to the vehicle which was driven in the proving ground at various predetermined tracks. The load cell endured the durability test of the vehicle and was able to acquire load data corresponding to these tracks. The load data were then used in the design improvement of the engine mounts.

3. DESIGN AND ANALYSIS OF MULTI-AXIAL LOAD CELL

3.1. The Procedure

A new load cell has been designed and manufactured which is able to measure the three components of force and three components of moment. Strain gages are conveniently located on highly stressed areas. The mechanical behavior of the load cell is described by means of Finite Element Method that allow a quick preliminary design focused on the given technical specifications.

In order to decide on the location of the strain gages, each component of the load vector (F_x, F_y, F_z, M_x, M_y, M_z) has been applied individually on the body, strain fields obtained along the bridges of the cross member have been examined. In order to minimize the number of strain gages, a spot on the body has been chosen on which strain due to each component of loading is close to maximum as shown in Figure 3.1, these regions are suitable for strain gages to be mounted. Decoupling of the inputs is then achieved by some arithmetic operations [8].

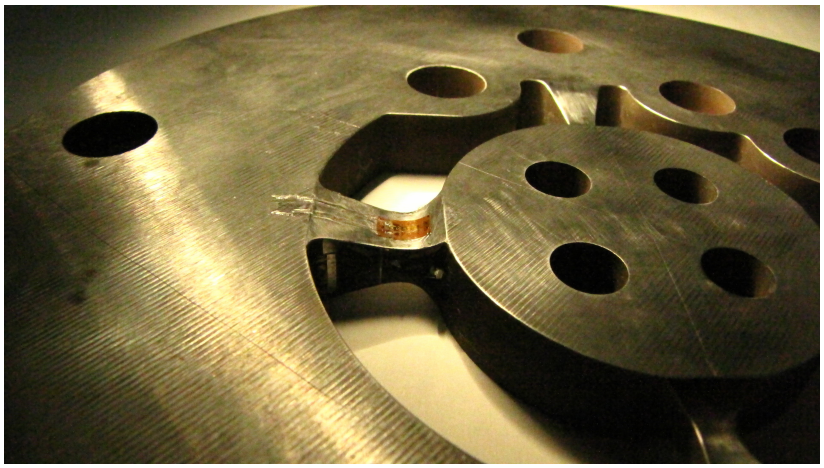

Figure 3.1. Strain Gages attached to the Load-Cell.

For the multi-axis load cell, there are six components of the input vector, namely F_x, F_y, F_z, M_x, M_y and M_z. In order to relate the input load vector to the output strain vector, a matrix must be formed. For this purpose, for each loading case, the values of strain at all the proposed locations of strain gages along the axis of the strain gages have been determined. A virtual calibration has been performed by applying all six load components individually and then recording the responses of the 8 virtual strain gages at the maximum strain locations. [30]

The designs of both the load-cells and the fixtures used for calibration were drawn in Solidworks 3D software and the load cell was manufactured with a CNC milling machine and Wire Electro Discharge Machine (W-EDM). After manufacturing the load-cell a physical calibration has been done in order to apply loads and measure the strains. The testing of the load cell is performed by using a servo-hydraulic testing machine. The load is applied in the form of triangular cyclic loading. In order to investigate the repeatability of the measurements, load has been applied in two cycles with a frequency of 0.1 Hz. This procedure has been carried out for both tension and compression with a cycle count of 2 repeatedly. Load, displacement and strain readings from 12 strain gages have been recorded using a data acquisition device with a sampling rate of 100 Hz.

Strain values that are sensitive only to one load component have been obtained, such that the results are decoupled. Using formulas obtained in the design and analysis, virtual strain values are determined which are sensitive almost to only one force component, and a Calibration Matrix has been formed.

3.2. Design of Multi-axis Load Cell

3.2.1. Design Constraints

The geometry of the load cell that can be used both in the left hand and the right hand side engine mounts is optimized considering the following constraints:

- The maximum loading condition that is provided by FORD-OTOSAN are as follows:
  $F_x = \pm 20kN$
  $F_y = \pm 4kN$
  $F_z = \pm 10kN$

- The location of the strain gages should be determined to obtain a strain level greater than 100 $\mu\varepsilon$ in active strain gages for all loading types.
- The location of maximum strains should be fixed and independent of the loading type, and the strain readings should be between 100-1000 $\mu\varepsilon$ for a reasonable sensitivity and strain signal levels that can be distinguished from background noise.
- The distribution of strain along the active gage length of the strain gage should be as uniform as possible.
- The active gage length should be determined according to the uniformity of strain at the maximum strain location.
- The maximum Von-Misses stress should not exceed 500 MPa. This will guarantee that a suitable steel material and a proper heat treatment method can be selected.
- The maximum Von-Misses stress amplitude should be less than the endurance limit of the steel. This will guarantee an infinite-life under fatigue loading.
- The geometric constraints resulting from packaging should also be considered to avoid interference.

3.2.2. Optimization

In order to obtain the final elastic element geometry, several different geometries have been considered and analyzed to check if they satisfy strain and stress requirements. The illustration of the first model is a simple cross-structured elastic element model shown in Figure 3.2. An analysis of this structure reveals that this geometry is not suitable for the design requirements because it suffers from low strain values on walls of the bridges.

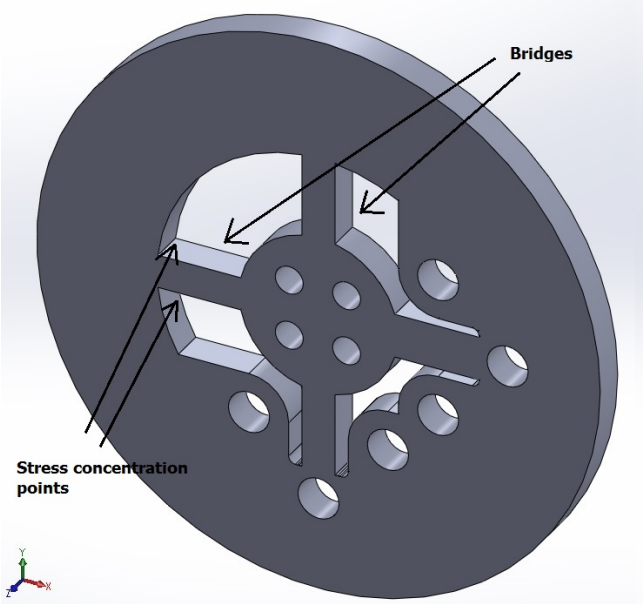

Figure 3.2. Illustration of the cross-structured elastic element model.

A second iteration has been performed with curved bridges to reduce the cross section and increase the strain values, hence sensitivity as shown in Figure 3.3.

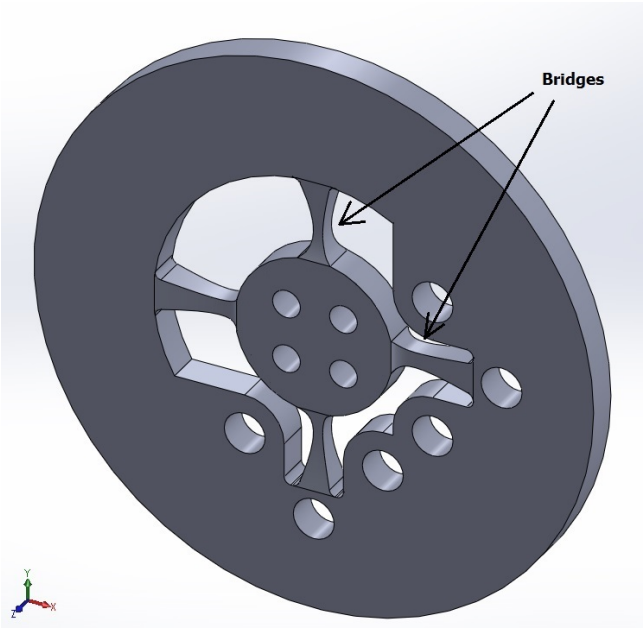

Figure 3.3. Illustration of the load cell design with curved bridges.

Several iterations are performed by increasing the curvature and reducing the length of the bridges. In the final design an appropriate dimension has been chosen in order to decrease the stiffness of the load cell and increase the concentration of stress on the bridges in order to measure high values of strain due to applied loads. A decision has been made to decrease the dimensions of the cross section of the bridges in order to obtain appropriate strain values. The overall thickness of the load cell is decided to be 10 mm in order to reduce the minimum cross section at the bridges without imposing high stress concentrations due to sharp decreases in cross section. The final design is shown in Figure 3.4.

The basic geometry of the load cell to be used both for the right and left hand side mounts consists of an inner ring and an outer ring connected by four bridges as shown in Figure 3.4, and the dimensions are given in mm in Figure 3.5. Note that the cross section of the bridges in the y-direction is smaller for the load cell to be more sensitive in that direction ($F_x = \pm 20kN$ whereas $F_y = \pm 4kN$)

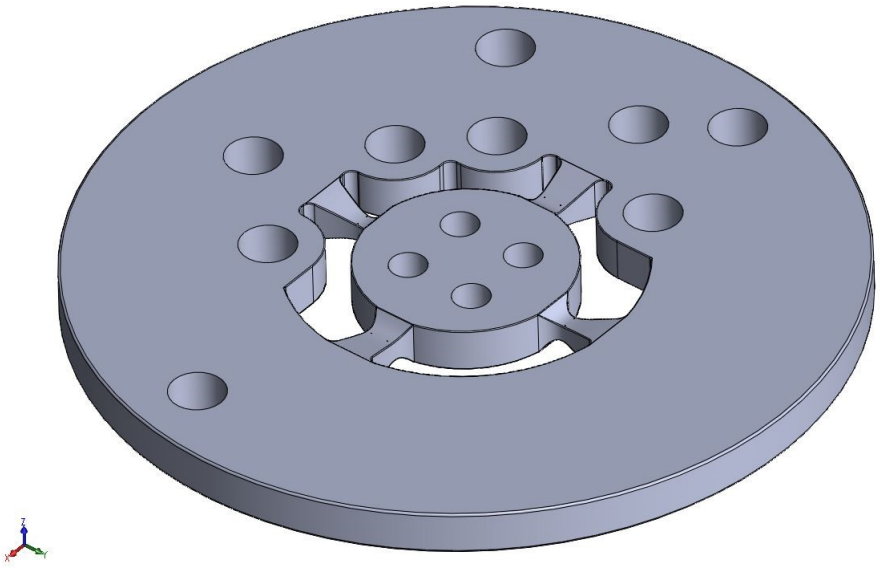

Figure 3.4. Geometry of the load cell.

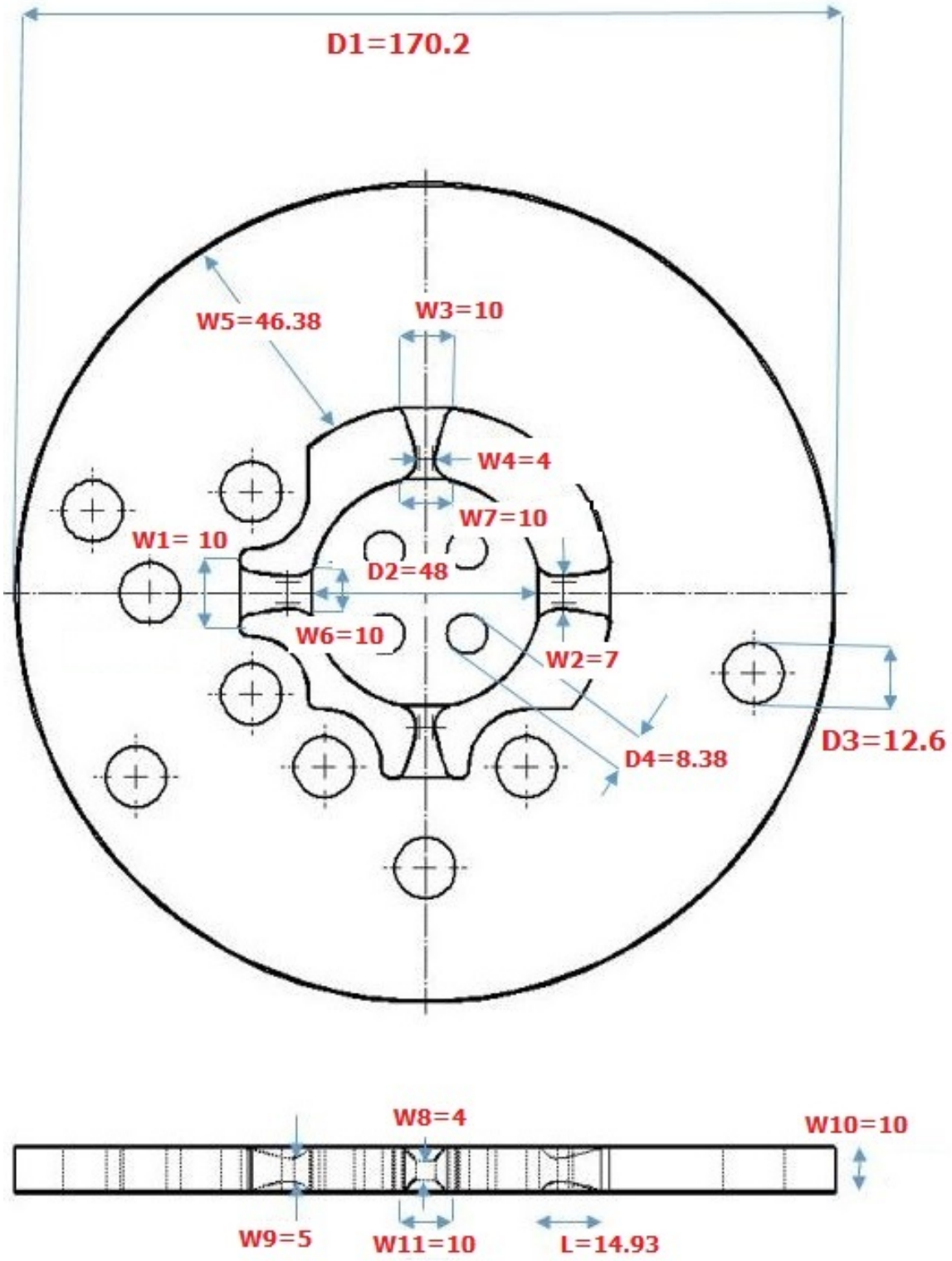

Figure 3.5. Dimensional design parameters for the proposed structure in mm.

In Figure 3.6, Left Hand Side load cell (LC1) engine mount is shown; in this figure, the bracket between the engine mount and the engine is replaced with the proposed load cell. Similarly in Figure 3.7, Right Hand Side load cell (LC2) engine mount is shown; in this figure the bracket between the engine mount and the engine is replaced with the proposed load cell.

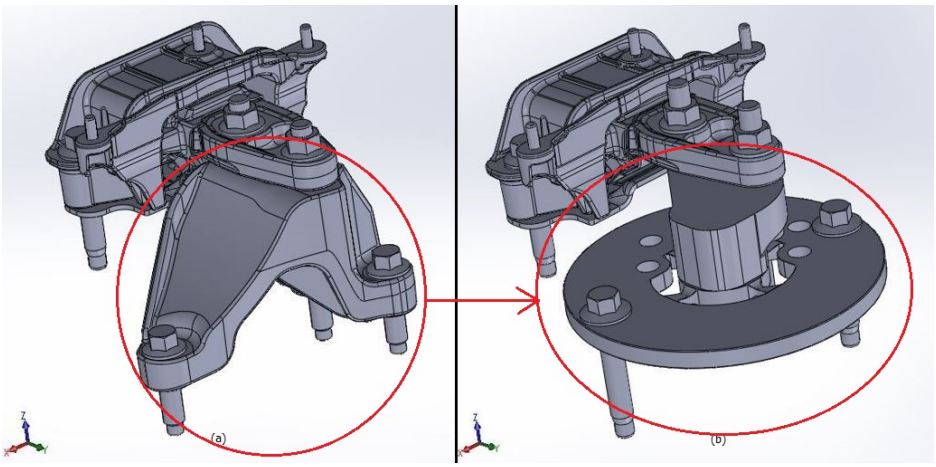

Figure 3.6. (a) Left Hand Side (LC1) engine mount is shown; (b) the bracket between the engine mount ant the engine is replaced with the proposed load cell.

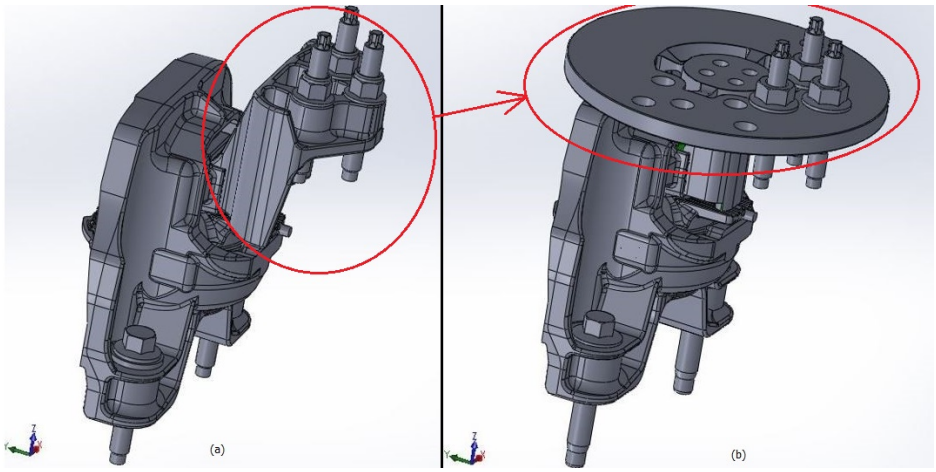

Figure 3.7. (a) Right Hand Side (LC2) engine mount is shown; (b) the bracket between the engine mount and the engine is replaced with the proposed load cell.

A Finite Element Analysis has been carried out in order to calculate the virtual calibration matrix of the proposed load cell by applying appropriate boundary conditions and forces and moments in three Cartesian directions individually. For simplicity in calculations single load cell geometry has been proposed to be used both in the left and right hand side engine mounts.,

The difference between the design given in this thesis and the designs in literatures regarding multi-axial load cells are given below:

- Full bridge is not used in this design because it suffers from low strain values on walls of the bridges.
- Load levels and sensitivities in this design are different in different directions.
- Bridges have a curvature shape which results in a localization of maximum strain values for different loads on the bridges. Stress concentrations are minimized and stress values are sufficient for infinite life.
- The body overall is simple, small and light-weighted comparing with other designs.
- Specially designed slots are added in the optimized design in order to reduce the interference error of bending moments when loads are applied along different axes.

3.2.3. Placement of the Strain Gages

Strains occurring due to applied loads can be decoupled by using 12 strain gages. Locations of these strain gages are illustrated in Figure 3.8. The active area of 1.5 mm x 1.2 mm of two strain gages are shown in Figure 3.9, which shows the strain distribution under F_x, to give an idea of how the strain gages should be located on the bridges.

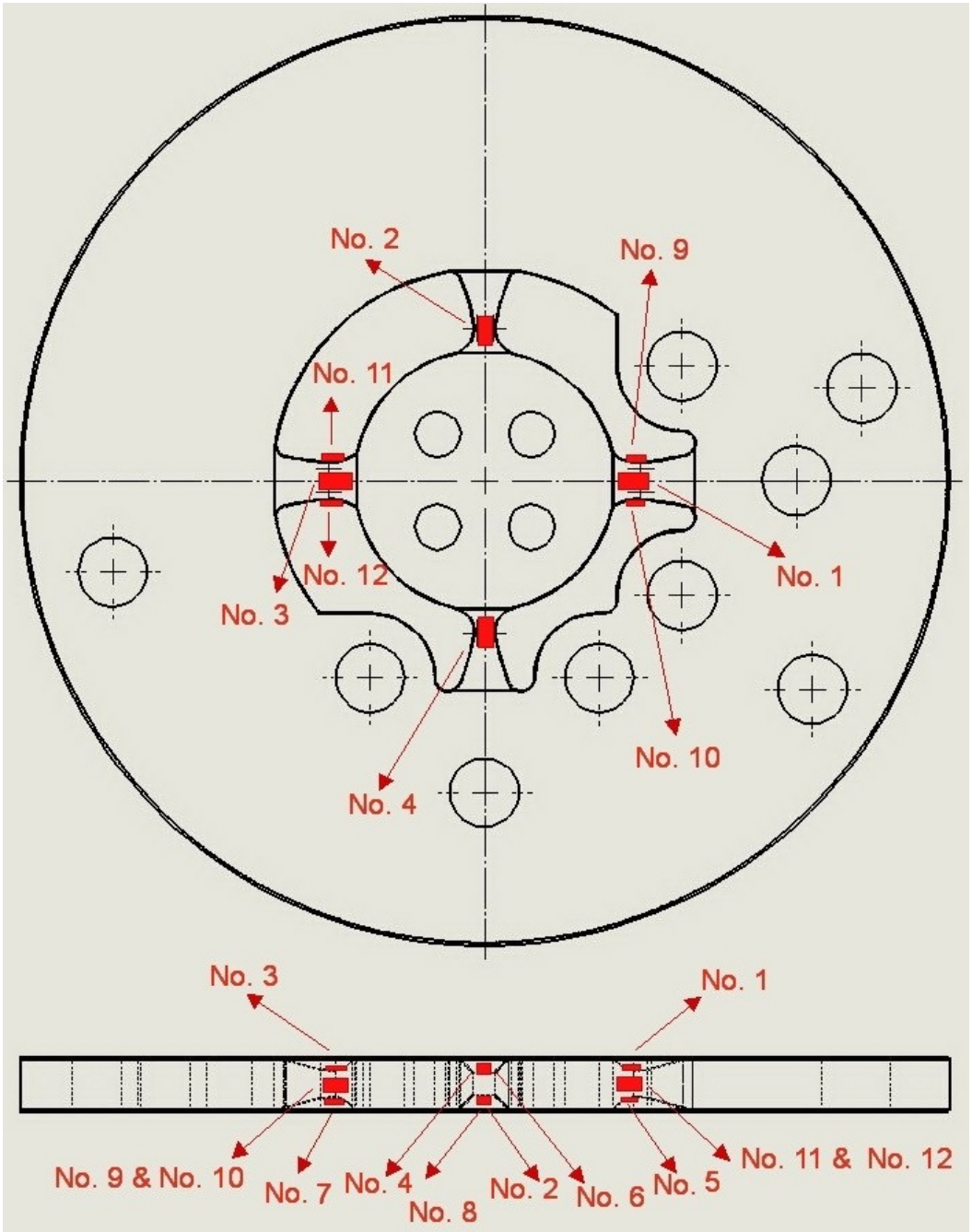

Figure 3.8. Locations of strain gages.

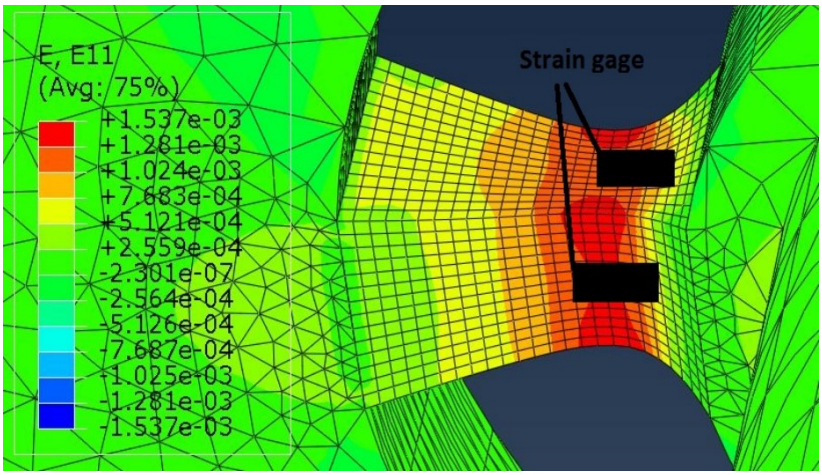

Figure 3.9. The location of the active grid area of the strain gages.

3.2.4. Fixtures To Apply Forces in X and Y Axis

To apply the required loads in desired directions, special fixtures were designed to mount the load-cell on the servo-hydraulic testing machine.

A special fixture shown in Figures 3.10 is designed for applying loads in x and y directions. Bending and torsion moments resulting from an off axis applied force to the top fixture are isolated from the load cell so that only the force itself is measured by the load cell. The upper and lower fixtures are connected to the tensile testing machine, the upper fixture is fixed to the load cell and load is applied by the piston of the testing machine to the lower fixture, both in tension and compression mode. .

In this assembly the load cell is subjected to loads in x-direction and by rotating the load-cell 90^0 clock-wise, in y direction. Two swivels are used to connect the upper fixture to the load cell as shown in Figure 3.11 in order to minimize the bending moments imposed by any possible misalignment of the fixture or load cell during installation.

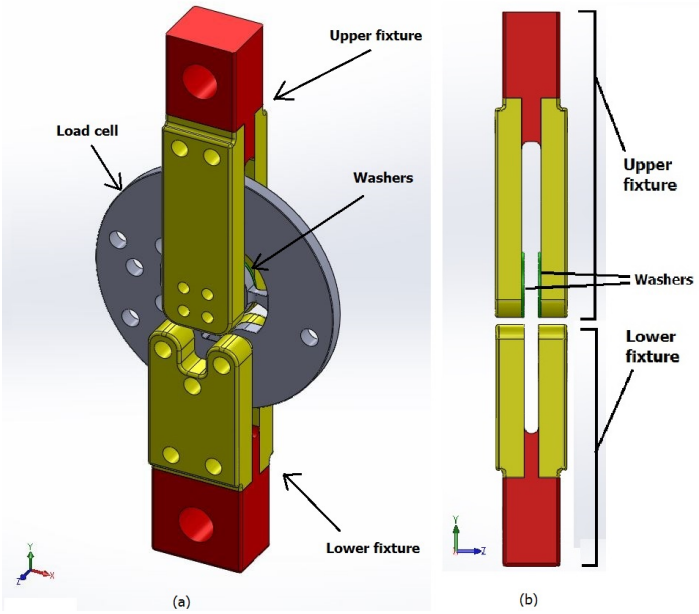

Figure 3.10. (a) Assembly for applying load in x and y directions (modified fixtures), (b) side view cross section of the fixture assembly.

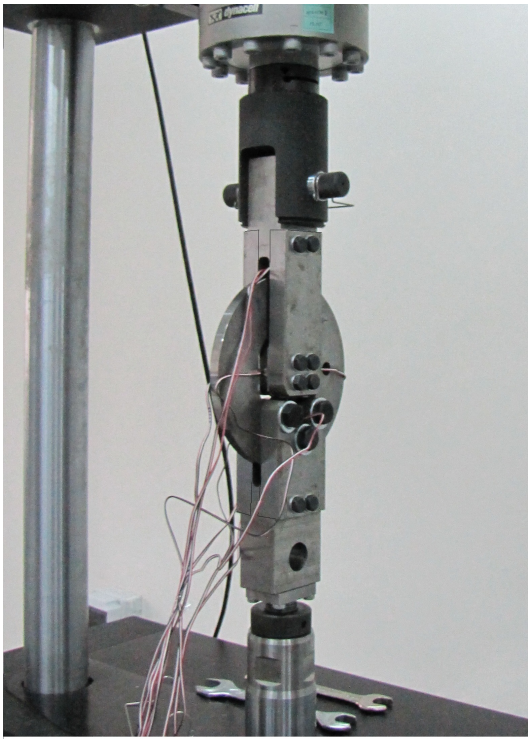

Figure 3.11. Assembly of the modified fixture on the tensile testing machine.

3.2.5. Fixture To Apply Force in Z Direction

For applying a force in z-direction to the load cell, the fixture shown in Figure 3.12 is utilized. Lower fixture is mounted to the piston of the servo-hydraulic tensile testing machine and the upper fixture is fixed to the load-cell and the load cell is connected to the lower fixture using M12 bolts. Two swivels are used to connect the upper fixture to the load cell as shown in Figure 3.12c in order to minimize the bending moments imposed by any possible misalignment of the fixture or load cell during installation.

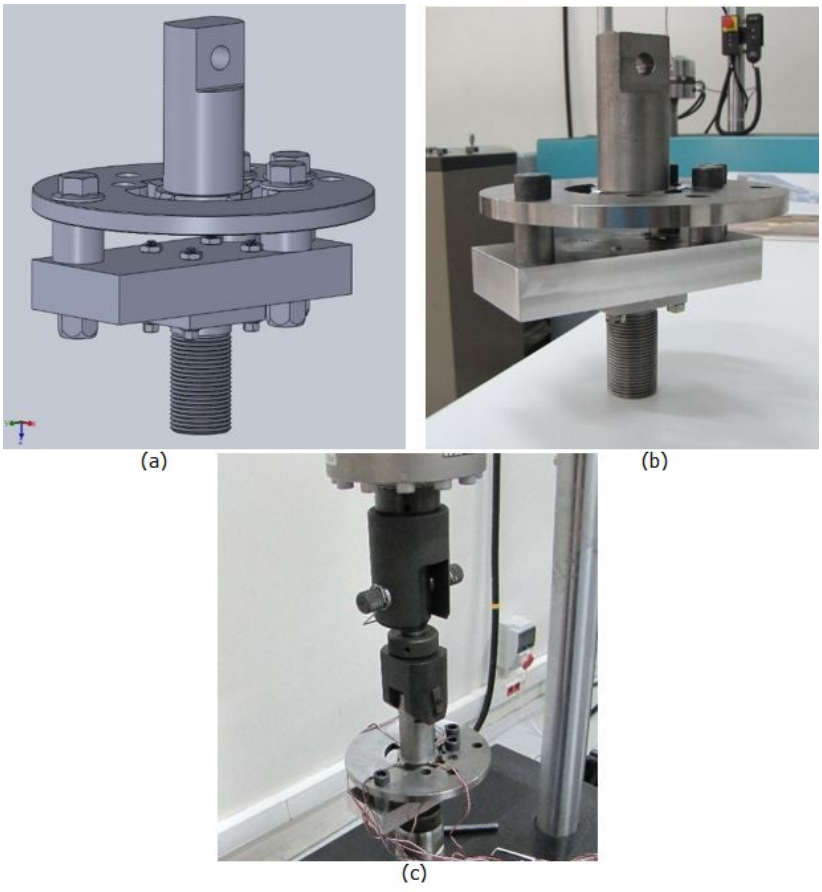

Figure 3.12. Assembly for applying load in z direction, (a) Illustration of the fixture in Solidworks 3D, (b) Fixture assembly and (c) Assembly of the fixture on the tensile testing machine.

3.2.6. Fixture To Apply Moments Around X-, Y- And Z-Axes

Bending moments in x-, y- and z-directions are applied to the load-cell using the fixture shown in Figures 3.13, 3.14 and 3.15. The mounting plate used in the z axis test is utilized to fix the load-cell in its position tightly. Then a one meter steel bar is connected to the middle point of the upper fixture so that proper amounts of weight can be hanged from the loose point of the moment arm.

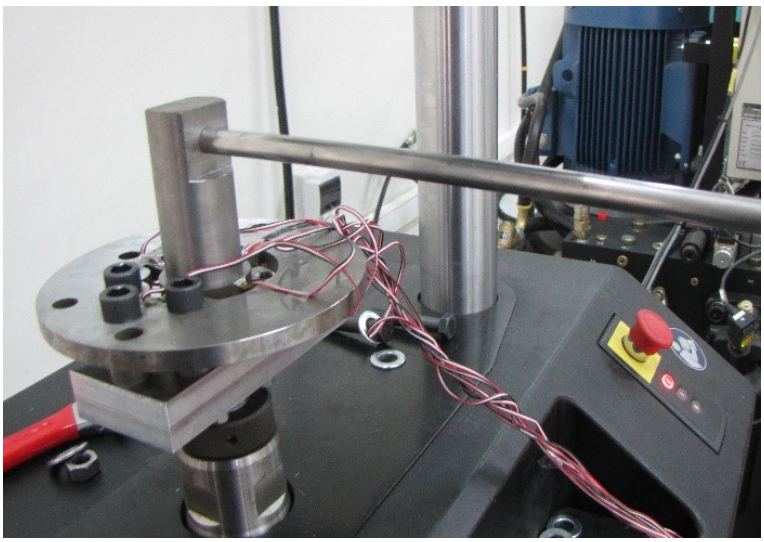

Figure 3.13. Assembly for applying moment in x direction.

The strain readings due to the weight and the moment generated by the weight of the bar is zeroed, so that only the strains due moment generated by the additional weights hanged were measured. The contribution of the weights themselves were minimal as compared to the strains due to moment generated by the weights.

Figure 3.14. Assembly for applying moment in y direction.

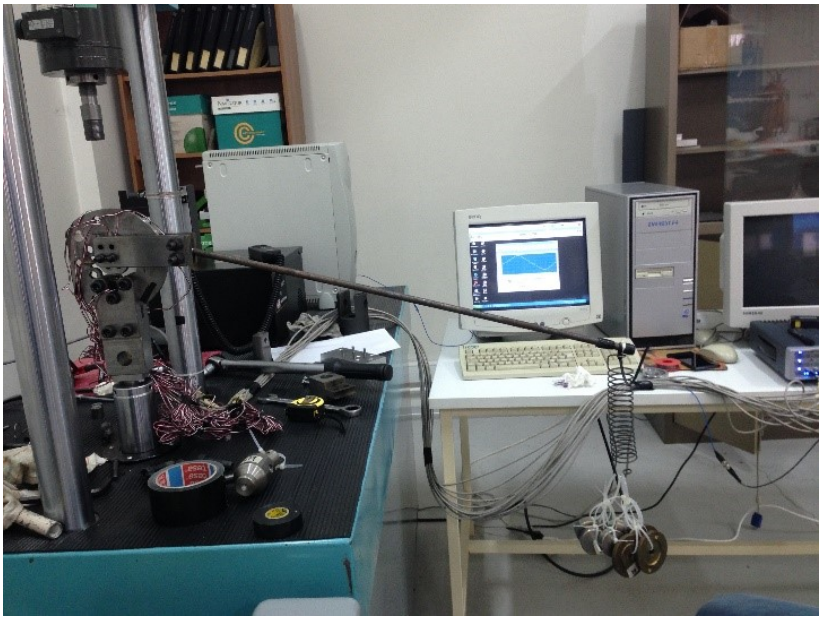

Figure 3.15. Assembly for applying moment in z direction.

3.3. Virtual Calibration of the Load Cells

3.3.1. Boundary Conditions

Figures 3.16, 3.17, 3.18 and 3.19 [31] show the holes the load cell was fixed and the holes in which load was applied. The red colored holes are where the load cell was fixed and the green holes are where the load was applied both in tension and compression.

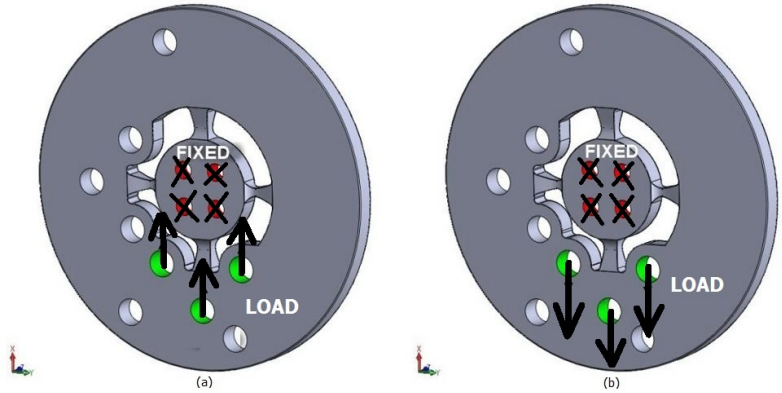

Figure 3.16. Illustration of boundary conditions for virtual calibration in x-direction for tension and compression, (a) compression and (b) tension.

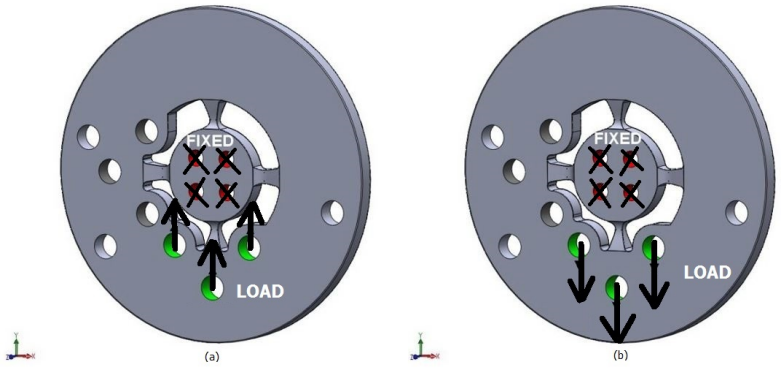

Figure 3.17. Illustration of boundary conditions for virtual calibration in y-direction for tension and compression, (a) compression and (b) tension.

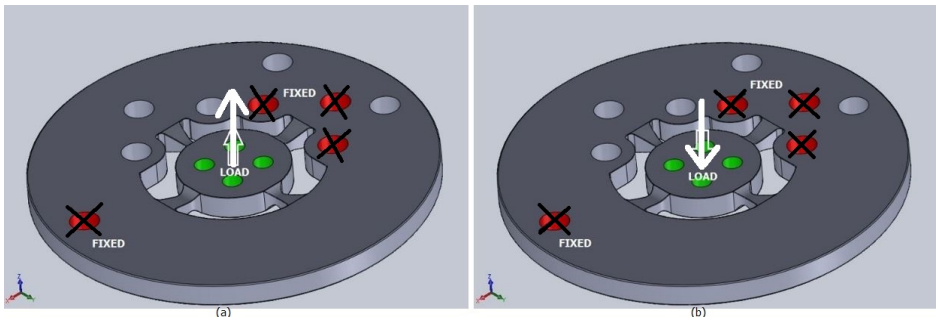

Figure 3.18. Illustration of boundary conditions for virtual calibration in z-direction for tension and compression, (a) tension and (b) compression.

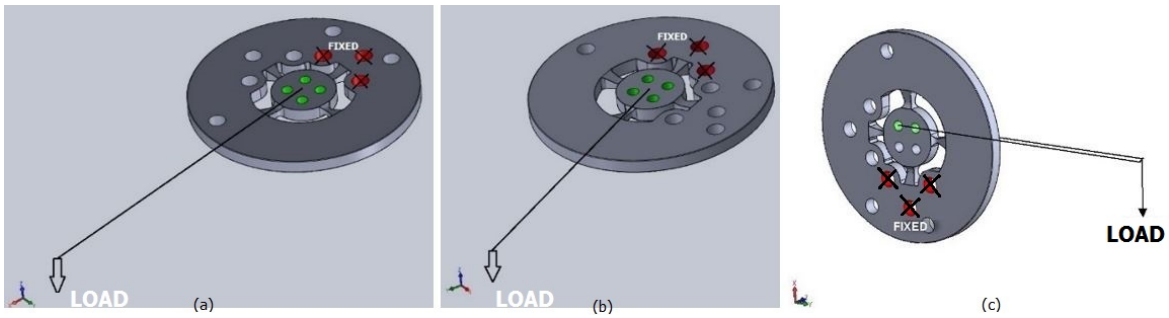

Figure 3.19. Illustration of boundary conditions for virtual calibration for moments in x, y and z directions, (a) M_x, (b) M_y, (c) M_z.

In order to minimize the number of strain gages, a spot on the body is chosen on which strain due to each component of loading is close to maximum. These regions are suitable for strain gages to be mounted. Decoupling of the inputs is then achieved by some arithmetic operations which are described later in the thesis.

3.3.2. Determination of the Calibration Matrix

A finite element analysis has been carried out for the load cell design. The geometry of the design has been meshed coarsely for the initial simulation and then a mesh refinement has been carried out in the bridges. A fine mesh is used in the areas

of high stress gradients and a coarser mesh in areas of low stress gradients where the magnitude of the stresses is not of interest as shown in Figure 3.20. The mesh density has been increased to an efficient amount in order for the numerical solution provided by the model design to converge toward a unique value. The shape of the elements for the mesh on the bridges where strain gages are mounted on are uniform. A structured meshing technique is used to create the mesh with a global element size of 0.2 seeds.

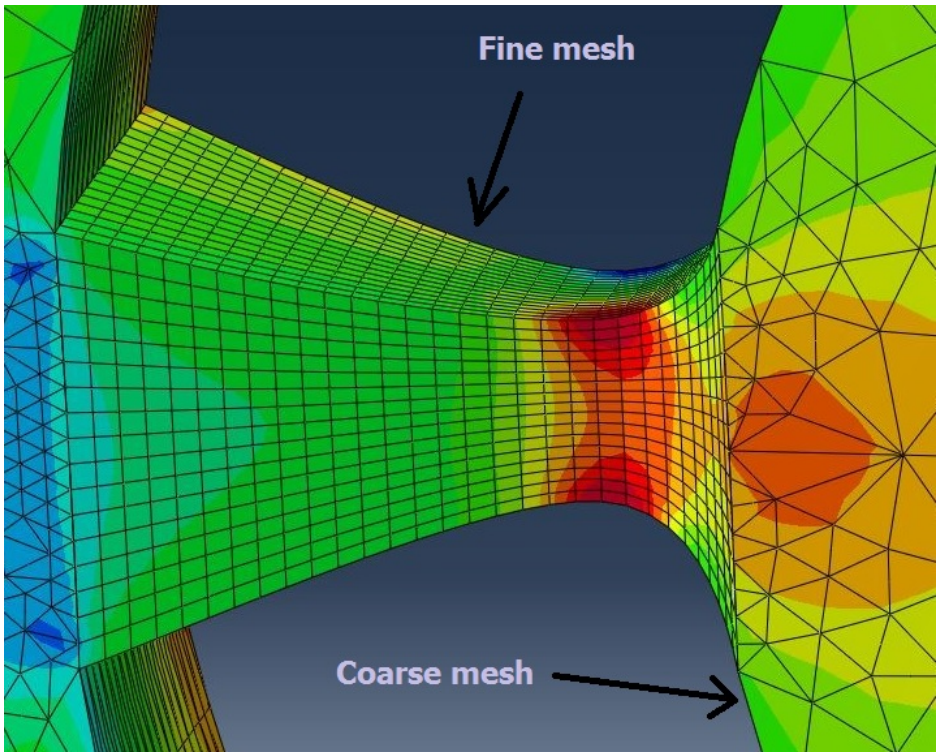

Figure 3.20. Locations of coarse and fine mesh of the design.

The procedure for virtual calibration is described in this section. In order to decide on the locations of the strain gages, each component of the load vector $(F_x; F_y; F_z; M_x; M_y; M_z)$ is applied individually on the body, and strain fields obtained along the bridges of the cross are examined.

For the multi-axis load cells, there are six components of the input vector, namely: $F_x; F_y; F_z; M_x; M_y; M_z$. In order to relate the input load vector to the output strain vector, a transformation matrix must be calculated. For this purpose, for each

loading case, the values of strain at all the proposed locations of strain gages are to be determined [32].

It must be noted that, because of the curvature at locations of the strain gages, the values of normal strains in x- and y-directions must be transformed into a new coordinate system in order to obtain the correct values of the strain to be measured by mounted strain gages. This effect is illustrated in Figure 3.21. This can be done in ABAQUS by defining a local coordinate system located at the node where strain gage is to be mounted on.

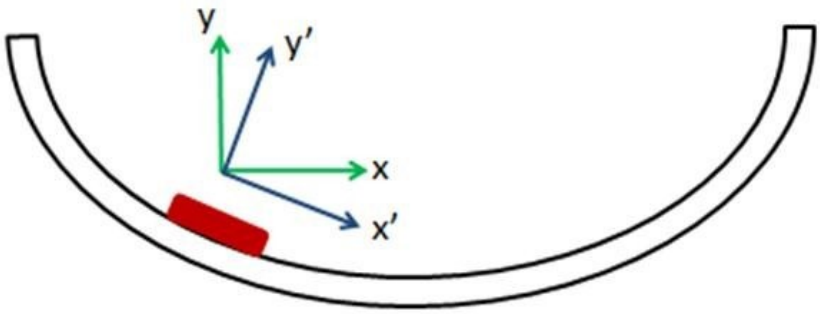

Figure 3.21. Required transformation of strain for correct strain values for strain gages.

Values of strain to be measured by each strain gage must be decoupled in order to obtain the calibration matrix. Calibration matrix is the matrix relating the load vector to the strain values measured by strain gages.

$$\{\mathbf{E}\} = [\mathbf{S}].\{\mathbf{F}\} \tag{3.1}$$

$\{\mathbf{E}\}$ denotes the strain vector obtained from the strain measurement and $[\mathbf{S}]$ is the matrix relating loads to strains. $\{\mathbf{F}\}$ is the vector of loads which has six components

to be measured by the load cell. Calibration matrix is the inverse of **S**,

$$\{\mathbf{F}\} = [\mathbf{S}]^{-1}\{\mathbf{E}\} = [\mathbf{C}]\{\mathbf{E}\} \tag{3.2}$$

The matrix relating load components to strain gage measurements is a 12x6 matrix, hence it cannot be inverted. In order to obtain a square calibration matrix, strain values measured by strain gages are manipulated by arithmetic operations. To form a strain vector of six components, six "virtual" strain gage values are determined by mathematical operations. Strain values are manipulated such that each strain value thus obtained changes with only one force component, which means the calibration matrix must be a diagonal matrix for the ideal case. For the real case, diagonal values of the calibration matrix must be significantly larger than other components of the matrix.

It is then straightforward to obtain the matrix S, which relates forces and moments to virtual strains. A further manipulation is carried out by dividing the strain values by the applied forces in order to obtain the strains per unit force (kN or Nm) and per unit moment (Nm).

3.4. Fatigue Analysis of Multi-Axial Load Cell

Static and fatigue strength analysis of the original load cell and the modified one have been carried out. A material of sufficiently high ultimate tensile and yield strength and the accompanying heat treatment method has been chosen and the manufacturing precision and surface quality has been determined accordingly.

During the analysis the safety factors against yielding under static loading have been calculated. During the static analysis abuse loads provided by FORD-OTOSAN company have been assumed to be the maximum load levels that the engine mounts are going to experience.

During the fatigue analysis, the alternating load magnitudes encountered during the abuse load cycles reported by FORD-OTOSAN company are assumed to determine the alternating stress levels in fatigue loading. The safety factors for infinite fatigue life are calculated under all loading conditions.

Accurate prediction of fatigue life of any structure is not possible due to the statistical nature of fatigue. Well controlled tests on the most simple configurations of test specimens result in a wide scatter band of results. With complex structures typical of a load cell, analysis is even more complex. Theoretical analysis can produce approximations, however, which can be useful in estimating the margin of safety at which a particular load cell design is operating.

3.4.1. Multiaxial Fatigue analysis

This load cell involves a multiaxial state of cyclic stress. This means that at any point, the directions of the principal stresses can vary during the loading cycle and are therefore a function of time. Furthermore, the magnitudes of the principal stresses themselves may no longer be proportional to each other [9, 33].

3.4.1.1. Critical Plane Method. The method used for calculating the fatigue damage under multiaxial loading for this design is the critical plane method. This method is based on predicting the extent of damage in specific directions and planes within the component.

Critical plane approach recognizes that fatigue damage is essentially directional and so considers the accumulation of damage on particular planes. So in other words, damage is calculated for all possible planes and the worst or critical plane is selected. The critical plane is the plane with the most predicted fatigue damage. In this method, the normal stress is calculated and rainflow counted on multiple planes. These planes have normals that lie in the plane of the physical surface [9]. The orientation of each plane is defined by the angle Φ with the local x-axis which is shown in Figure 3.22.

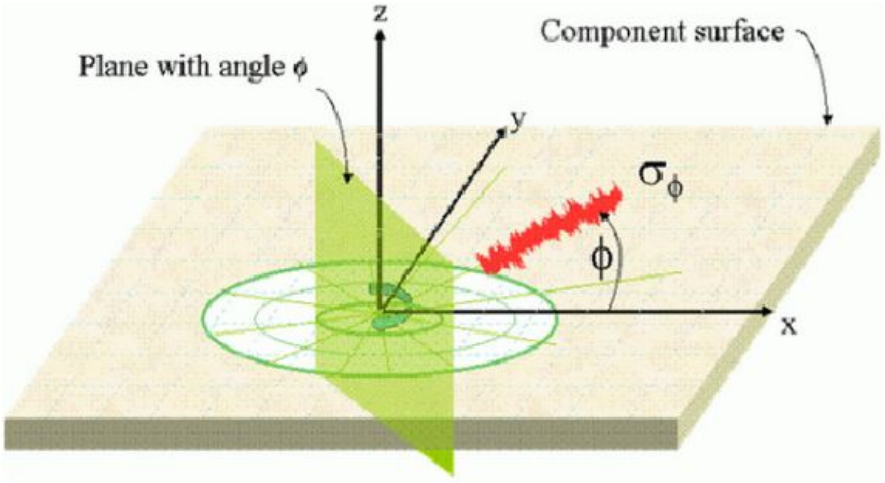

Figure 3.22. Resolution of normal stress for critical plane analysis [9].

The stress on each plane is calculated from:

$$\sigma_\phi = \frac{\sigma_{xx} + \sigma_{yy}}{2} + \frac{\sigma_{xx} - \sigma_{yy}}{2}.cos2\phi + \sigma_{xy}sin2\phi \tag{3.3}$$

where σ_{xx} is the normal stress component on the x-plane in the x-direction and σ_{yy} is the normal stress component on the y-plane in the y-direction. ϕ can take the values 0, 10, 20, 30,..., 170 degrees [9].

3.4.1.2. Mean Stress Correction. The main feature of a stress cycle that affects fatigue damage is its range. Fatigue damage is also influenced by the mean stress of each cycle. Mean stress correction methods allow the effect of mean stress to be modeled and taken into account in the life prediction. The method used in this analysis is the Goodman method [9].

The Goodman mean stress correction calculates an effective stress amplitude based upon the mean stress and ultimate tensile stress of each cycle [9]. This method is used to calculate an effective stress S_e, based upon the stress amplitude S_a, mean

stress S_m, and the materials ultimate tensile stress:

$$S_a + S_m = 1 \tag{3.4}$$

This can work with all SN curves but must include datasets corresponding to zero mean or R=-1 (R-ratio), however, in nCode DesignLife software R-ratio can have any value. This has been shown in Figure 3.23.

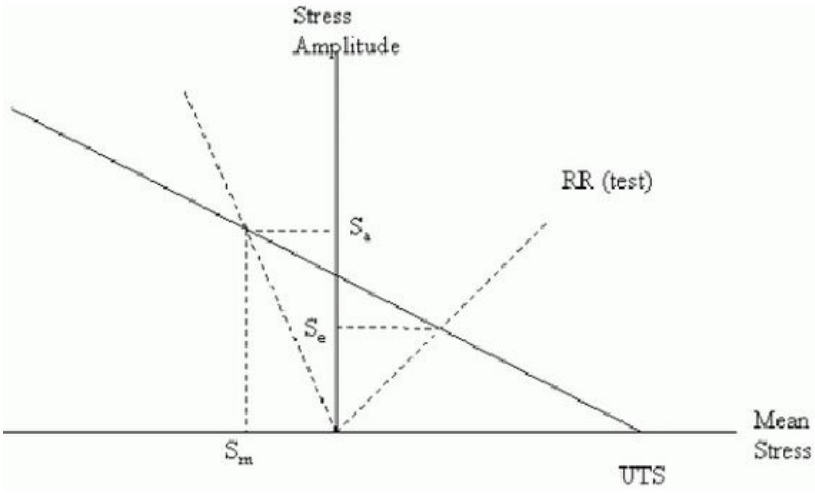

Figure 3.23. Graphical interpretation of Goodman correction [9].

3.4.1.3. Multiaxial Assessment. A standard method of a multiaxial assessment is carried out in the test. This method provides a more robust measure of the biaxiality and non-proportionality of the local loading [9].

Figure 3.24 shows a 3-D scatter plot of σ_{xx} vs σ_{yy} vs σ_{xy} where every point is represented as a point from stress history (cloud data). The biaxiality and non-proportionality of the loading is obtained by the procedure below:

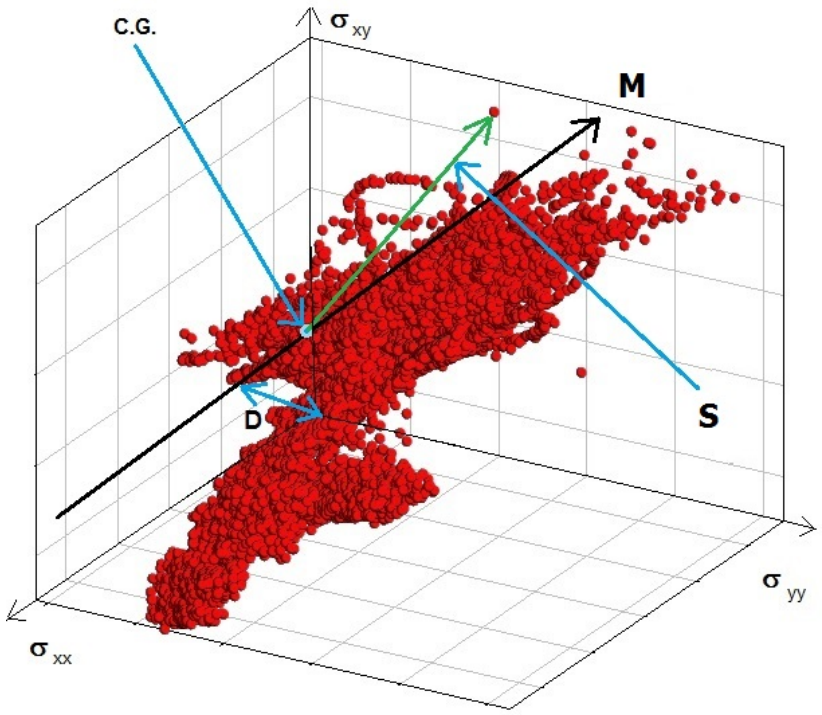

Figure 3.24. Analysis of data cloud for Standard Multiaxiality Assessment [9].

- Determining the position of the center of gravity of the data cloud.
- Determining the principal moments of inertia of the data cloud about the center of gravity $I_1 \geq I_2 \geq I_3$.
- Finding the vector {M} corresponding to the principal axis with the minimum moment of inertia I_3.
- Finding the point with the largest distance S from the center of gravity of the cloud.
- Finding the offset D of {M} from the origin [9].

If the data cloud correlates closely with a straight line through the origin, the loading is proportional. The larger the offset from the origin, the more non-proportional the loading. The orientation of the vector {M} tells us the average biaxiality [9]. The calculation is as follows:

The cloud aspect ratio is defined as:

$$A = \frac{I_3}{I_1} \tag{3.5}$$

The cloud offset factor is defined as:

$$O_f = \frac{D}{2.S} \tag{3.6}$$

The non-proportionality factor is defined as:

$$f = \sqrt{A + {O_f}^2} \tag{3.7}$$

The three components (σ_{xx} vs σ_{yy} vs σ_{xy}) of the vector {M} defines a 2-D stress tensor σ_{ij} from which the 2 principal stresses σ_1 and σ_2 are obtained where $|\sigma_1| \geq |\sigma_2|$. The mean biaxiality is then calculated from:

$$\lambda = \frac{\sigma_2}{\sigma_1} \tag{3.8}$$

The orientation of the plane corresponding to vector {M} meaning the orientation of σ_1 which gives the dominant stress direction, corresponds to the most likely critical plane orientation. The mean biaxiality and non-proportionality factors are reported in the fatigue analysis results, together with the dominant stress direction in Chapter 4.

3.4.2. Loads and material properties

- Loads

The maximum loads reported by FORD-OTOSAN company are shown in Table 3.2.

- Material Properties

Material is chosen to be Uddeholm Alvar which is a chromium-nickel-molybdenum-vanadium alloyed steel because of its good toughness, good resistance to high thermal stresses, good stability in hardening and good through-hardening properties which are important parameters determining the fatigue behavior of the part. The material has been used "as received" so it is reported to have a hardness of 500 HRB according to the manufacturer's data sheet [34] from which the ultimate tensile strength is calculated to be:

$$UTS = 3.48 \times HRB = 1720Mpa \tag{3.9}$$

The properties of Uddeholm Alvar alloyed steel is given in Table 3.1.

Table 3.1. Material properties for fatigue analysis.

Material type:	Uddeholm Alvar 14
σ_u**: Ultimate Tensile Strength (Mpa)**	1720
E: Elastic Modulus (GPa)	205
A: Stress Range Intercept (Mpa)	7714
b_1**: First Fatigue Strength Exponent**	-0.1339
b_2**: Second Fatigue Strength Exponent**	0
Nc_1 **: Fatigue Transition Point (cycles)**	10^6
SE: Standard Error of Log (N)	0.1
Nf_c**: Fatigue CutOff**	10^{30}
me: Poisson's Ratio	0.29

Figure 3.25 shows the S-N curve for Uddeholm Alvar 14 which consists of three linear segments on a log-log plot. The central section has the formula:

$$\Delta\sigma = A(N_f)^{b1} \tag{3.10}$$

Where N_f is the number of cycles to failure. NC_1 shows the point on the curve where it the curve goes to the second slope b_2. b_2 is set to zero which acts as a fatigue limit.

The fatigue cutoff is a numerical limit which is set to 10^{30} cycles. It has no physical interpretation. RR is the R-ratio or load ratio ($\sigma_{min}/\sigma_{max}$) of the tests used to determine the S-N curve.

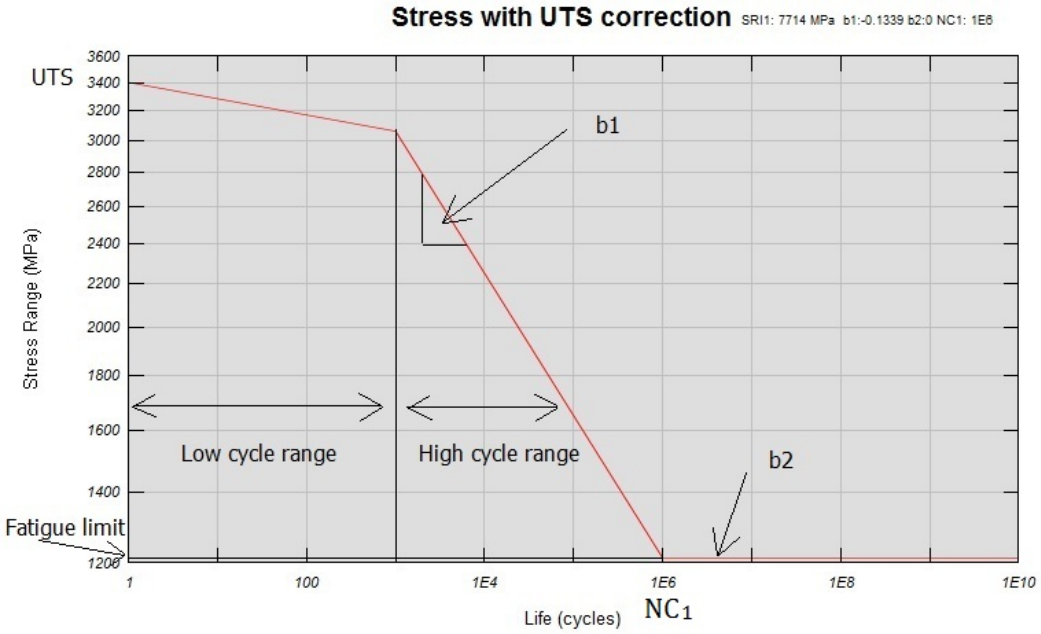

Figure 3.25. Wöhler S-N curve for Uddeholm Alvar 14 [9].

3.4.3. Failure Analysis Procedure

A damage calculation has been done on the load cell using the nCode DesignLife software. It is to be noted that nCode DesignLife simulates the life of the load cells by combining FEA results with a fully detailed loading history that the load cells undergo during their usage and experimentally obtained material data that describes the material response to repeated loadings. In order to establish a relationship between input loads and the resulting strain response, the strain transfer matrix is used. Once calculated for unit load cases on the FE model, the strain transfer matrix is used in conjunction with measured physical strain gage histories from proving ground to reconstruct in-service load histories. In this case the load cells are mounted on the vehicle and then the vehicle has been driven on various testing tracks, and the strain data is obtained. These predicted load histories can then be used as realistic inputs

to the FE model, even as designs change, or as loading profiles for laboratory testing.

The procedure for calculating the load inputs is shown schematically in Figure 3.26. Both virtual and physical calibration matrix has been used in this procedure.

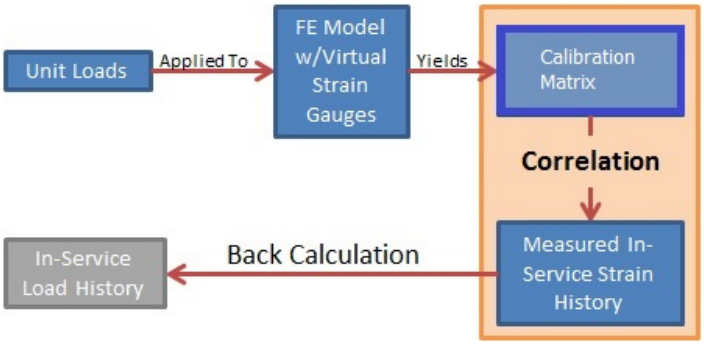

Figure 3.26. Construction of load history input.

- S-N Approach

The approach used in this method is the SN (or Nominal Stress) infinite life approach which is the oldest method of fatigue estimation. It is a graphical representation of the number of load cycles required to break a specimen, at a range of peak cyclic stress levels. It is limited to high-cycle fatigue. In SN approach, the calculated elastic stress range is used with a Wöhler S-N curve (log-log graph of stress range versus number of cycles to failure) to determine the damage per stress range, which can be seen in Figure 3.25. The damage is accumulated throughout the operational history to determine the total damage. The basic steps in SN are:

(i) Calculate linear elastic stress histories.
(ii) Extract fatigue cycles (generally using the rainflow algorithm).
(iii) Assess damage caused using stress range and S-N curve.
(iv) Accumulate the damages (generally using Miner's rule) [10].

The S-N approach typically relates nominal stresses to total failure and is suited pri-

marily to problems where there are a large number of cycles to failure. Regardless of the particular analysis technique applied, similar types of inputs are required. These can be described using the "5-Box Trick" shown in Figure 3.27. [10]

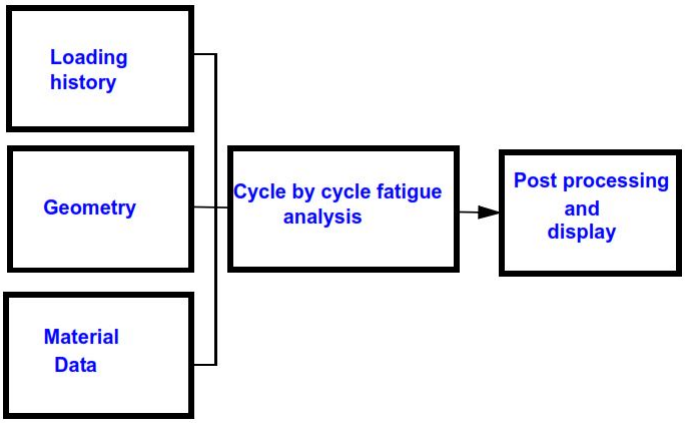

Figure 3.27. The fatigue analysis "5-Box Trick" [10].

In each case, the loading environment of the design has been defined (the Loading History Box). The geometry factor and description of the design has been made (The Geometry box) which in this case the FE analysis of the design has been considered. The response of the material to cyclic loading has been defined in the material data box as an S-N curve (Material Data). These three inputs have been combined in a cycle-by-cycle fatigue analysis and an initial result presented for post processing and display.

- The stress history of each element in the ABAQUS ODB file has been calculated by multiplying the stress by time domain force data for 6 degrees of freedom (DoF).
- Then the time domain critical plane method has been calculated and a rainflow cycle count has been conducted.
- At the end a damage calculation by Miner's rule using SN curve of the selected material has been obtained.

Miner's rule is one of the most widely used damage models for failures caused by fatigue. If there are k different stress levels and the average number of cycles to failure at the i_{th} stress, S_i, is N_i, then the damage fraction, C, is shown as:

$$\sum_{i=1}^{k} \frac{n_i}{N_i} = C \tag{3.11}$$

Where n_i is the number of cycles at stress S_i. C is the fraction of life to the cycles at the different stress levels. In general, when the damage fraction reaches 1, failure occurs.

The damage is defined as the product of stress and the number of cycles operated under this stress, which is:

$$W_i = n_i S_i \tag{3.12}$$

Assuming that the critical damage is the same across all the stress levels, then:

$$W_{Failure} = N_i S_i \tag{3.13}$$

3.5. Error Analysis of Multi-Axial Load Cell

No measurement of a physical quantity can be entirely accurate. It is important to know, therefore, just how much the measured value is likely to deviate from the unknown, true value of the quantity. This chapter contains brief discussions about what kinds of errors that can occur, how they can be estimated, and how to carry error estimates into calculated results.

3.5.1. Root mean square error (RMSE)

In strain gage measurements errors arise from misalignment of the strain gage with respect to the axis along which strain is to be measured. Error refers only to the uncertainty in measurements, regardless of what the expected value is supposed to be.

The Root Mean Square Error (RMSE) (also called the root mean square deviation, RMSD) is a frequently used measure of the difference between values predicted by a model and the values actually observed from the environment that is being modeled. These individual differences are also called residuals, and the RMSE serves to aggregate them into a single measure of predictive power.

The RMSE values can be used to distinguish model performance in a calibration period with that of a validation period as well as to compare the individual model performance to that of other predictive models which have been implemented and presented in this report.

3.5.2. Error Analysis Procedure

The aim of the error analysis performed is to understand the effect of misalignments in strain gage bonding. For this purpose, three hypothetical cases are considered:

(i) All the strain gages are bonded perfectly to the central axis of the bridge as shown in Figure 3.28.

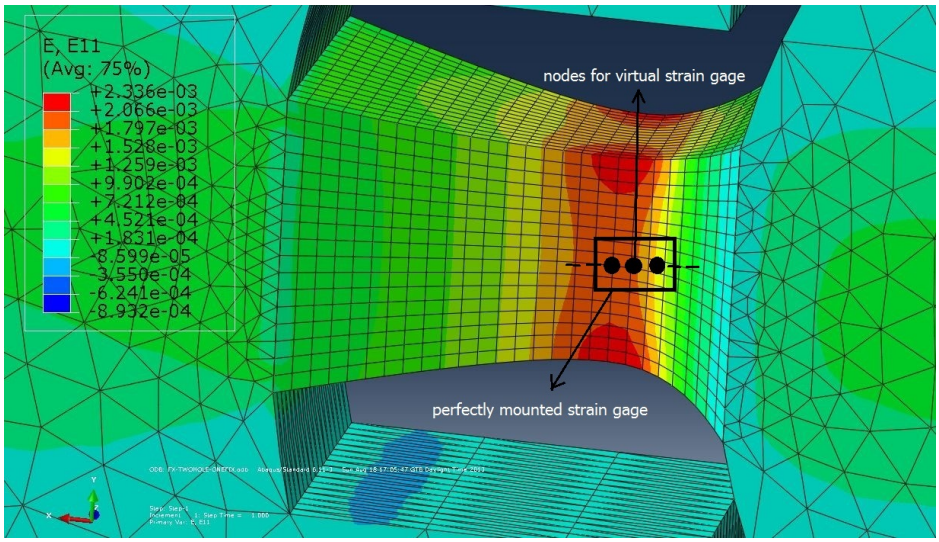

Figure 3.28. Nodes to obtain average strain values for perfectly bonded strain gage.

(ii) All the strain gages are bonded with an angle of 33 degrees to the central axis of the bridge as shown in Figure 3.29.

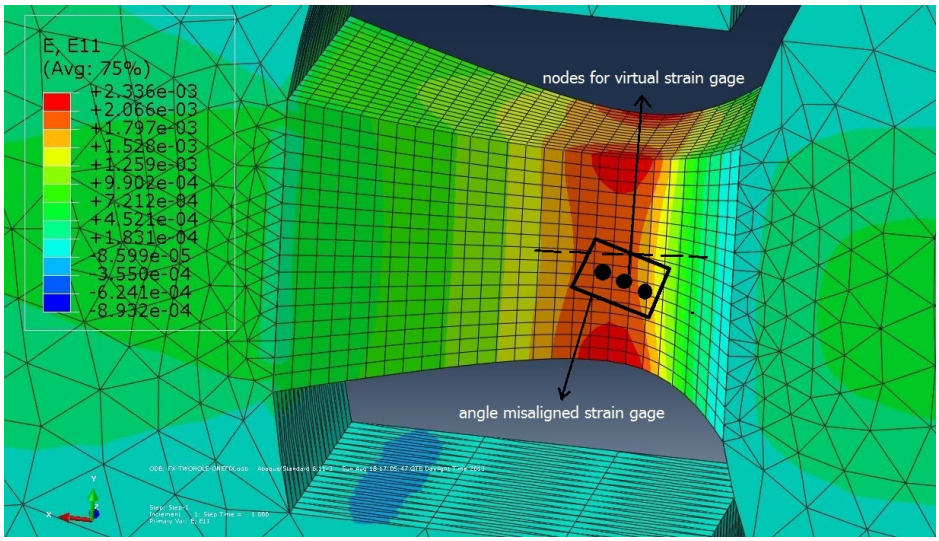

Figure 3.29. Nodes to obtain average strain values for angle misaligned strain gage.

(iii) All the strain gages are bonded with an offset of 1.25 mm to the central axis of the bridge as shown in Figure 3.30

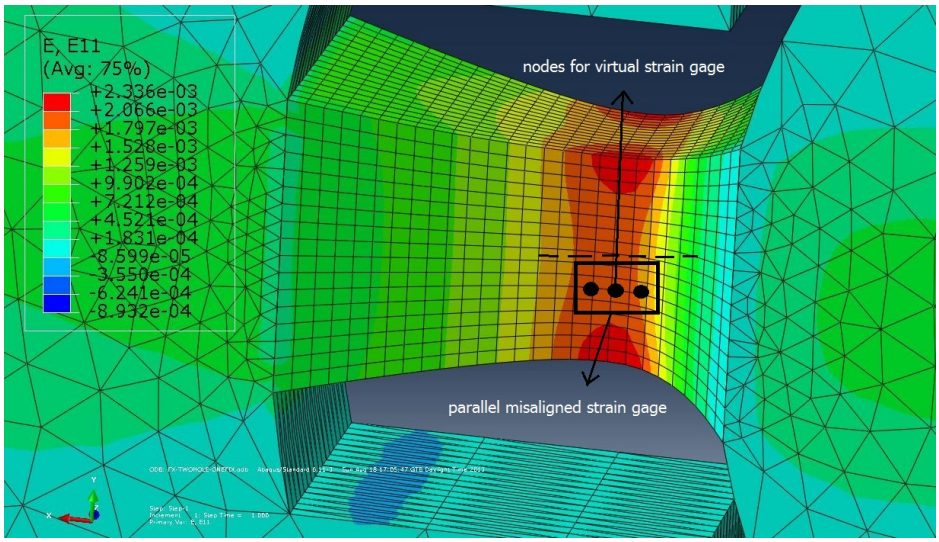

Figure 3.30. Nodes to obtain average strain values for perfectly bonded and parallel misaligned strain gages.

The strain readings over the indicated nodes are averaged to find the average strain measurement from the strain gage used. The following procedure is used in error analysis:

(i) Six channel random load signal was generated with three channels of load and three channels of moment using a code written in MATLAB application. The duration was chosen to be 10 seconds and the signal is generated with a sampling rate of 10 Hz.

(ii) The bandwidth of the loads are chosen to be representing the abuse loading case supplied by FORD-OTOSAN as shown in Table 3.2.

(iii) The 12 channel strain response was calculated by using the two erroneous calibration matrices for perfectly positioned and misaligned strain gage cases as described above, obtained from FEA.

(iv) Using the original calibration matrix, the load signal was regenerated.

(v) The percent RMS error was then calculated for each time series according to the formula below.

$$\%RMSError = \sqrt{\frac{\sum_{i=1}^{n}(y_i - \hat{y}_i)^2}{n}} \frac{1}{\Delta y} \times 100 \tag{3.14}$$

where n is the number of samples (10 Hz sampling rate x 10 s = 100 data points), y_i is the value for real force and $\hat{y_i}$ is the value for erroneous force in i-th data point and Δy is the bandwidth.

RMS error assessment is needed when there is no physical calibration testing. Virtual calibration is used in order to convert 12 channel strain data to three force and three moment components. When physical tests and calibration matrices are available, using the physical calibration matrices prevents error coming from mis aligned-positioned strain gages.

RMS error was calculated for each load component shown in Table 3.2.

Table 3.2. Bandwidth for all channels of six channel random load signal.

F_x	F_y	F_z	M_y	M_x	M_z
± 20 kN	±8 kN	±10 kN	±20 Nm	±40 Nm	±20 Nm

4. RESULTS

4.1. Finite Element Analysis of the Load Cell

The outputs of six different loading cases are given below:

- F_x= +20kN , other components are zero

When the body is subjected to a maximum abuse force in x-direction, the bridges on one side of the x-axis is under compression while the ones on the other side is in tension. This is shown in Figure 4.1. The strain distribution in the tension side and compression side are shown in Figures 4.2 and 4.3 respectively. There are negligible strains in the y-direction bridges, along the length of the bridges.

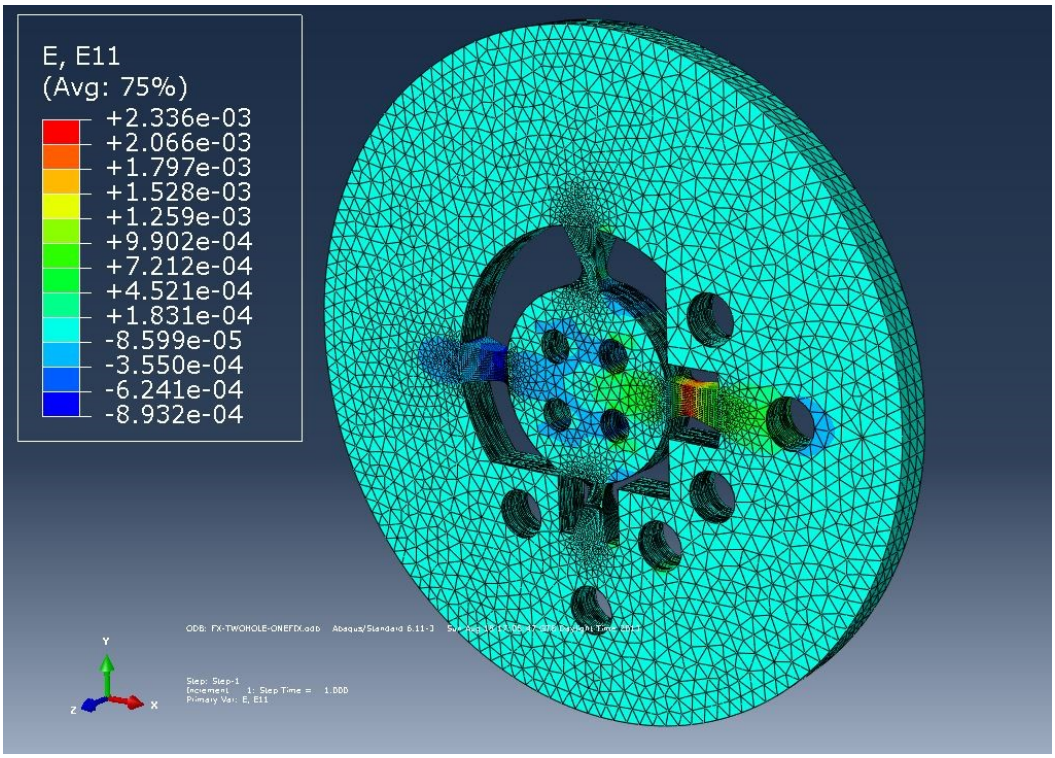

Figure 4.1. Strains under the effect of F_x= +20kN.

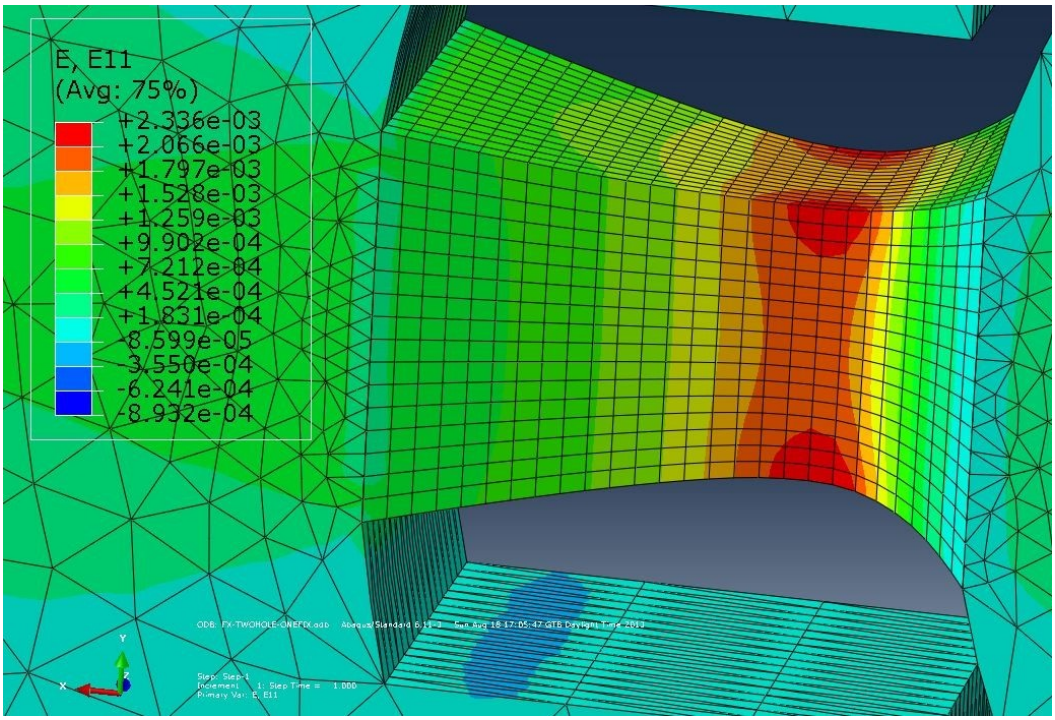

Figure 4.2. Strains under the effect of F_x= +20kN (Tension side).

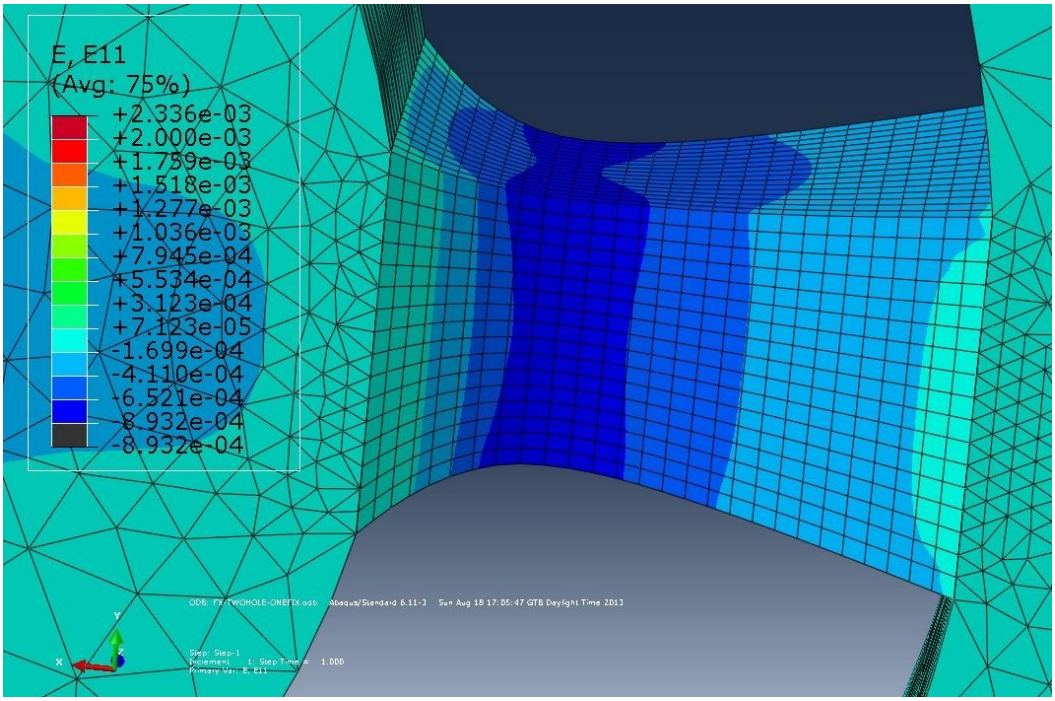

Figure 4.3. Strains under the effect of F_x= +20kN (Compression side).

- F_y= +5 kN, other components are zero

When the elastic element is loaded by a force in y-direction, a similar distribution of strain is obtained as in force in x-direction case. One of the bridges is compressed while the other one is in tension.

- F_z= -10 kN , other components are zero

When the body is subjected to a force in z-direction, deformation can be observed on all the bridges. Under the effect of a force in –z direction, strains in the body are as shown in the Figure 4.4. From the figure it can be seen that bottom sides of the bridges are in compression while upper sides are is in tension. The regions close to the fillets toward the inner rings experience higher strain, thus these regions are suitable candidates for strain gages to be located.

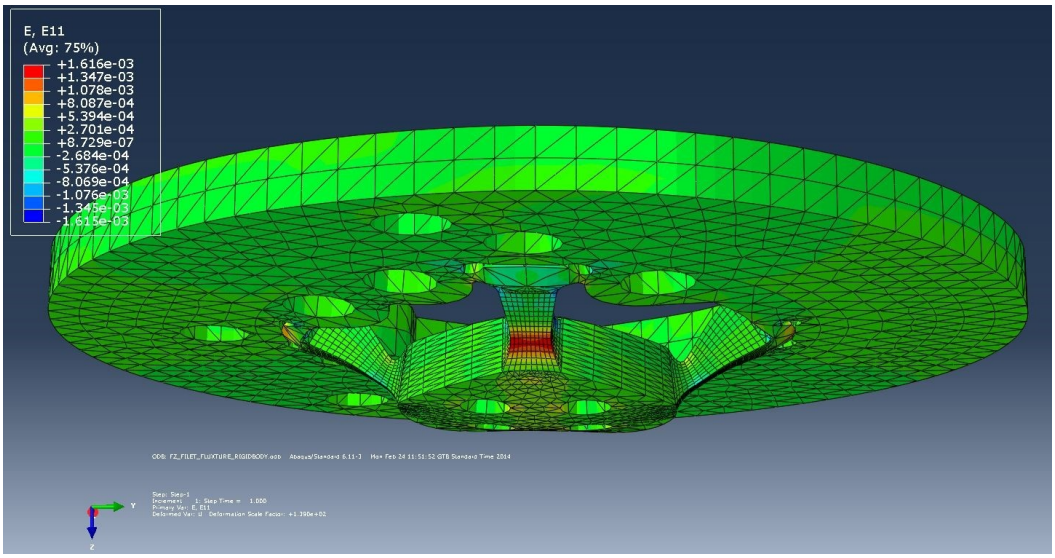

Figure 4.4. Strains under the effect of F_z= -10 kN.

- Moments

Although in the engine mounts, the exact magnitude of the moments applied in the x-direction, or whether or not there exists a moment at all is not known, estimated

moments of 40, 20, and 20 Nm are applied in x- y- and z- directions respectively and the resulting strains on the bridges are acquired. Figure 4.5 shows strains under the effect of M_z= 20 Nm.

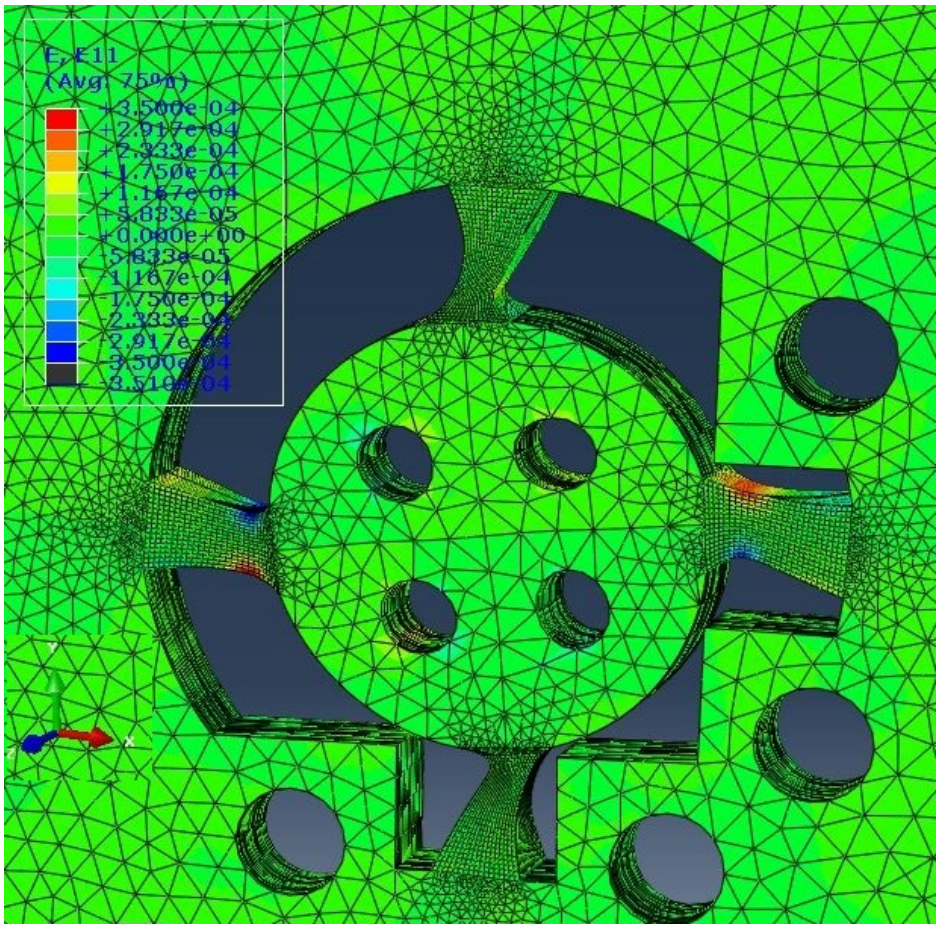

Figure 4.5. Strains under the effect of M_z= 20 Nm.

4.2. Virtual Calibration of the Load Cell

Table 4.1 shows the values of strain to be measured by each strain gage for each loading case in FEA.

The manipulated strain values, which can be considered as measurement obtained

Table 4.1. Strain values obtained at each strain gage location for each loading cases.

	Fx (20 kN)	**Fy (8 kN)**	**Fz (10 kN)**	**My (20 Nm)**	**Mx (40 Nm)**	**Mz (20 Nm)**
SG1	1891	-45	-1070	1	451	14
SG2	-366	-680	-2485	409	39	-1
SG3	-724	-60	-2063	1	-523	12
SG4	-368	1135	-2410	-414	34	-24
SG5	1892	-61	1062	1	-451	1
SG6	-331	-679	2467	-409	27	-27
SG7	-724	-45	2145	1	523	1
SG8	-368	1135	2396	414	19	-17
SG9	1724	-175	3	-3	-59	127
SG10	1738	275	9	2	-49	-130
SG11	-660	-172	75	0	-24	-126
SG12	-668	273	67	-2	-23	139

from virtual strain gages, are calculated as follows:

$$e_1 = (\varepsilon_1 + \varepsilon_5) - (\varepsilon_3 + \varepsilon_7) \tag{4.1}$$

$$e_2 = (\varepsilon_4 + \varepsilon_8) - (\varepsilon_2 + \varepsilon_6) \tag{4.2}$$

$$e_3 = (\varepsilon_1 + \varepsilon_2 + \varepsilon_3 + \varepsilon_4) - (\varepsilon_5 + \varepsilon_6 + \varepsilon_7 + \varepsilon_8) \tag{4.3}$$

$$e_4 = (\varepsilon_2 - \varepsilon_4) - (\varepsilon_6 - \varepsilon_8) \tag{4.4}$$

$$e_5 = (2\varepsilon_1 - \varepsilon_3) - (2\varepsilon_5 - \varepsilon_7) \tag{4.5}$$

$$e_6 = (\varepsilon_9 - \varepsilon_{10}) - (\varepsilon_{11} - \varepsilon_{12}) \tag{4.6}$$

In Equation 4.5, ε_1 and ε_5 have been multiplied by 2 in order to diagonalize the strain values in Table 4.2. By using the values presented in Table 4.1, the entries of the Matrix S are given in Table 4.2.

Table 4.2. The entries of the Matrix S for design 1.

	Fx (1 kN)	**Fy (1 kN)**	**Fz (1 kN)**	**My (1 Nm)**	**Mx (1 Nm)**	**Mz (1 Nm)**
e1	261	0	-9	0	0	0
e2	-2	907	0	-1	0	1
e3	-2	0	-1610	-2	-2	1
e4	0	0	-15	82	0	0
e5	0	12	-6	0	51	0
e6	-1	-1	-1	-1	0	11

It should be noted that the order of loads is as $F_x; F_y; F_z; M_y; M_x; M_z$; and the reason for this is because when M_x comes before M_y the matrix does not become diagonal. The strain values are divided to the applied load values in order to determine the unit response. After that, by calculating the inverse of that matrix, calibration matrix is obtained. Calibration matrix [C1] for tension, based on FEA strain values at maximum load from Equation 3.2 is obtained as follows:

$$\begin{Bmatrix} F_x \\ F_y \\ F_z \\ M_y \\ M_x \\ M_z \end{Bmatrix} = \begin{bmatrix} \mathbf{3823} & 1 & -21 & 2 & -8 & 22 \\ 8 & \mathbf{1102} & 0 & 19 & 5 & -31 \\ -4 & 0 & \mathbf{-621} & -50 & -25 & -13 \\ 81 & 3 & -110 & \mathbf{12127} & 8 & -113 \\ 6 & -181 & -49 & -4 & \mathbf{14032} & -154 \\ 162 & 51 & -35 & 147 & 119 & \mathbf{38311} \end{bmatrix} X10^{-6}. \begin{Bmatrix} e_1 \\ e_2 \\ e_3 \\ e_4 \\ e_5 \\ e_6 \end{Bmatrix} \quad (4.7)$$

Calibration matrix [C2] for compression, based on FEA strain values at maximum load is obtained as follows:

$$\begin{Bmatrix} F_x \\ F_y \\ F_z \\ M_y \\ M_x \\ M_z \end{Bmatrix} = \begin{bmatrix} \mathbf{-3846} & -2 & 21 & 2 & 0 & -22 \\ 9 & \mathbf{-1077} & 0 & -1 & -4 & 31 \\ 5 & -5 & \mathbf{621} & 5 & -25 & 14 \\ -59 & -1 & 110 & \mathbf{-12127} & -8 & 115 \\ 0 & 52 & 49 & 3 & \mathbf{-14032} & 161 \\ 0 & -21 & 35 & -149 & -122 & \mathbf{-39060} \end{bmatrix} X10^{-6}. \begin{Bmatrix} e_1 \\ e_2 \\ e_3 \\ e_4 \\ e_5 \\ e_6 \end{Bmatrix} \quad (4.8)$$

Where the strains are unit-less and forces are in kN and moments are in Nm.

4.3. Physical Calibration

Two identical load cells, LC1 (Load Cell 1) and LC2 (Load Cell 2) shown in Figures 3.6 and 3.7 from chapter 3.2 have been manufactured and physically calibrated. In order to calibrate the multi-axis load cells, strains occurring due to different loading types have been measured with strain gages as described in Chapter 3.2. However, the calibration results for only one of the load cells (LC1) are presented here. Table 4.3 compares the strain values obtained from Finite Element Analysis with those taken from strain gages during calibration tests for the maximum load applied during the tests for LC1. From the data, it can be seen that measured values are very close to FEA results.

Although some data differ slightly from FEA results, in general FEA results and measured values are in close correspondence.

From Table 4.3, it can be seen that strain values are coupled which means several strain gages indicate strain for every type of loading. These values of strain must be decoupled in order to obtain the calibration matrix.

Examining the data obtained from measurements and referring to Figure 3.6

Table 4.3. Strain gage values for maximum load in Tension (values in parenthesis are obtained by measurement (LC1).

	F_x **(20 kN)**	F_y **(8 kN)**	F_z **(10 kN)**	M_y **(20 Nm)**	M_x **(40 Nm)**	M_z **(25 Nm)**
SG1	1891 (2192)	-45 (-79)	-1070 (-961)	1 (1)	451 (455)	14 (7)
SG2	-366 (-288)	-680 (-667)	-2485 (-2259)	409 (385)	39 (40)	-1 (-16)
SG3	-724 (-984)	-60 (-120)	-2063 (-2290)	1 (1)	-523 (-558)	12 (10)
SG4	-368 (-567)	1135 (1224)	-2410 (-2484)	-414 (-417)	34 (40)	-24 (-20)
SG5	1892 (1958)	-61 (-167)	1062 (1003)	1 (1)	-451 (-477)	1 (1)
SG6	-331 (-242)	-679 (-712)	2467 (2245)	-409 (-417)	27 (39)	-27 (-20)
SG7	-724 (874)	-45 (-123)	2145 (2345)	1 (1)	523 (560)	1 (1)
SG8	-368 (-561)	1135 (1338)	2396 (2428)	414 (417)	19 (20)	-17 (-10)
SG9	1724 (1910)	-175 (-427)	3 (-8)	-3 (-3)	-59 (-70)	127 (114)
SG10	1738 (1832)	275 (308)	9 (-125)	2 (11)	-49 (-42)	-130 (-122)
SG11	-660 (-731)	-172 (-437)	75 (218)	0 (6)	-24 (-32)	-126 (-119)
SG12	-668 (-717)	273 (328)	67 (170)	-2 (-2)	-23 (-40)	139 (-132)

for locations of strain gages, it can be stated that strain gages 1 and 5 work in the same direction as the load applied whereas strain gages 3 and 7 work in the opposite direction, as expected. Other strain gages are expected to read strain values close to zero but measurements indicates that they are strained as well during the test. Another unexpected aspect of the data is that although the strain gages bonded at the opposite faces of the bridges of the load cell (SG1 and SG5 for example) are expected to read the same values, the strain values slightly deviate from each other as the load increases and they yield different slopes for load versus strain curves. These aspects indicate that there may be still slight misalignment in the fixture resulting in

unexpected moments or there may be slight misalignment during strain gage bonding.

As stated in the Section 3.3.2, in order to calibrate a multi-axis load cell, one needs to obtain strain values that are sensitive only to one load component, such that the results are decoupled. Using the formulas obtained in Equations 4.1 to 4.6, six virtual strain values are determined which are sensitive almost to only one force component.

The procedure to be followed to build the calibration matrix is same as numerical calibration. It is worth noting that in case of numerical calibration for finite element analysis strain values at different loads and are perfectly linear, thus there is only one calibration matrix. But in real case, the strain values are not perfectly linear. In this analysis, it is assumed that strain values behave linearly in tension and compression, and the two calibration matrices are obtained for tension and compression. They are then compared to virtual calibration matrix, which is unique for both tension and compression.

Table 4.4. Rendered Strain values used for calibration matrix (in Tension, values in parenthesis is obtained by measurement (LC1).

	Fx **(1 kN)**	**Fy** **(1 kN)**	**Fz** **(1 kN)**	**My** **(1 Nm)**	**Mx** **(1 Nm)**	**Mz** **(1 Nm)**
e1	261 (213)	0 (0)	-9 (-1)	0 (0)	0 (0)	0 (0)
e2	-2 (-30)	907 (988)	0 (-4)	-1 (1)	0 (0)	1 (0)
e3	-2 (3)	0 (5)	-1610 (-1601)	-2 (-2)	-3 (-4)	1 (0)
e4	-0 (-2)	0 (40)	-15 (40)	82 (81)	0 (0)	0 (0)
e5	0 (122)	12 (75)	-6 (-28)	0 (0)	51 (86)	0 (0)
e6	-1 (5)	-1 (7)	-1 (7)	-1 (-1)	0 (-1)	11 (26)

By using the values presented in Table 4.4, it is then straightforward to obtain the matrix C, which relates forces and moments to virtual strains. A further manipulation

is carried out by dividing the strain values in Table 4.4, by the applied forces in order to obtain the strains per unit force (kN) and per unit moment (Nm). The entries of the Matrix C for LC1 Load Cell is given below. The strain values are divided to the applied load values in order to determine the unit response. After that, by calculating the inverse of that matrix, calibration matrix is obtained.

Physical calibration matrix [C3] for tension, based on measured strain values at maximum load for LC1 from Equation 3.2 is obtained as follows:

$$\begin{Bmatrix} F_x \\ F_y \\ F_z \\ M_y \\ M_x \\ M_z \end{Bmatrix} = \begin{bmatrix} \mathbf{3323} & -28 & -2 & 2 & 23 & 22 \\ 10 & \mathbf{1011} & -3 & 19 & 5 & -1 \\ 11 & 0 & \mathbf{-624} & -12 & -29 & 11 \\ 28 & -45 & 31 & \mathbf{12235} & 76 & -120 \\ 6 & -192 & -62 & 8 & \mathbf{11575} & -146 \\ -71 & -36 & 184 & 147 & 54 & \mathbf{41042} \end{bmatrix} X10^{-6}. \begin{Bmatrix} e_1 \\ e_2 \\ e_3 \\ e_4 \\ e_5 \\ e_6 \end{Bmatrix} \quad (4.9)$$

Physical calibration matrix [C4] for compression, based on strain values at maximum load calculated by measured for LC1 is obtained as follows:

$$\begin{Bmatrix} F_x \\ F_y \\ F_z \\ M_y \\ M_x \\ M_z \end{Bmatrix} = \begin{bmatrix} \mathbf{-3446} & -16 & 56 & -33 & 29 & 27 \\ 25 & \mathbf{-100}1 & -10 & 0 & 25 & -12 \\ -35 & -19 & \mathbf{630} & 4 & 11 & 20 \\ -83 & -65 & -16 & \mathbf{-12655} & -20 & -123 \\ 109 & 315 & -27 & 112 & \mathbf{-13389} & -250 \\ -23 & 30 & 23 & -34 & 125 & \mathbf{-35986} \end{bmatrix} X10^{-6}. \begin{Bmatrix} e_1 \\ e_2 \\ e_3 \\ e_4 \\ e_5 \\ e_6 \end{Bmatrix} \quad (4.10)$$

Comparing matrices from virtual and physical calibration it can be seen that the

entries are in close correspondence. Forces and moments are coupled but the effect of this coupling is not extremely significant due to the difference in ranges of measured forces and moments. The large off-diagonal terms are due to slight misalignment in fixtures and can be improved with modifying the fixtures in order to reduce bending moments when loads are applied in testing. Only tension calibration matrices have been used for error analysis.

4.3.1. Comparison Figures of Physical and Virtual Calibration

Figures 4.6 to 4.11 show the comparison of response of the strain gages with the strains calculated by FEA for LC1 at maximum load:

During the calibration procedure in x-direction, force is varied between 0.2 N to 20 kN in tension and -0.2 to -20 kN in compression.

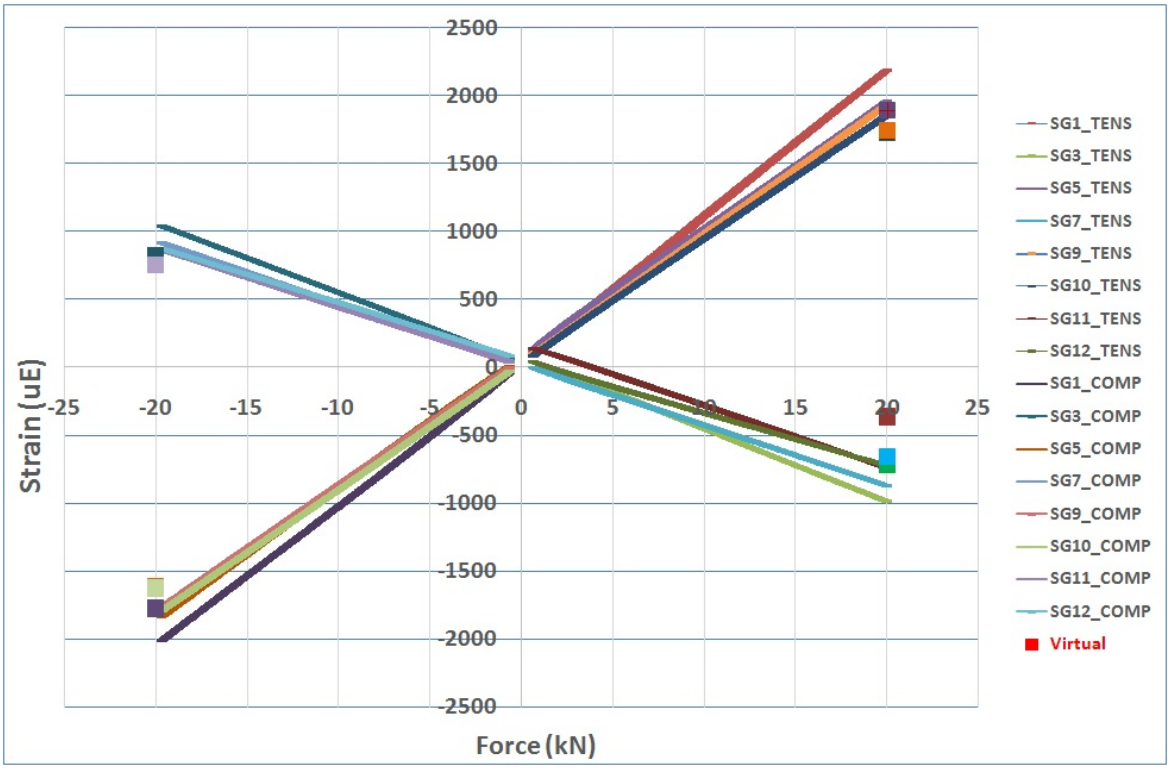

Figure 4.6. Comparison of the measured values with FEA in x-direction (LC1).

Force in y-direction is applied by utilizing the same fixture and rotating the load cell 90 degrees in clockwise direction. The load is varied from 0.1 N to 8 kN in tension and -0.1 to -8 kN for compression. The comparison can be seen in Figure 4.7.

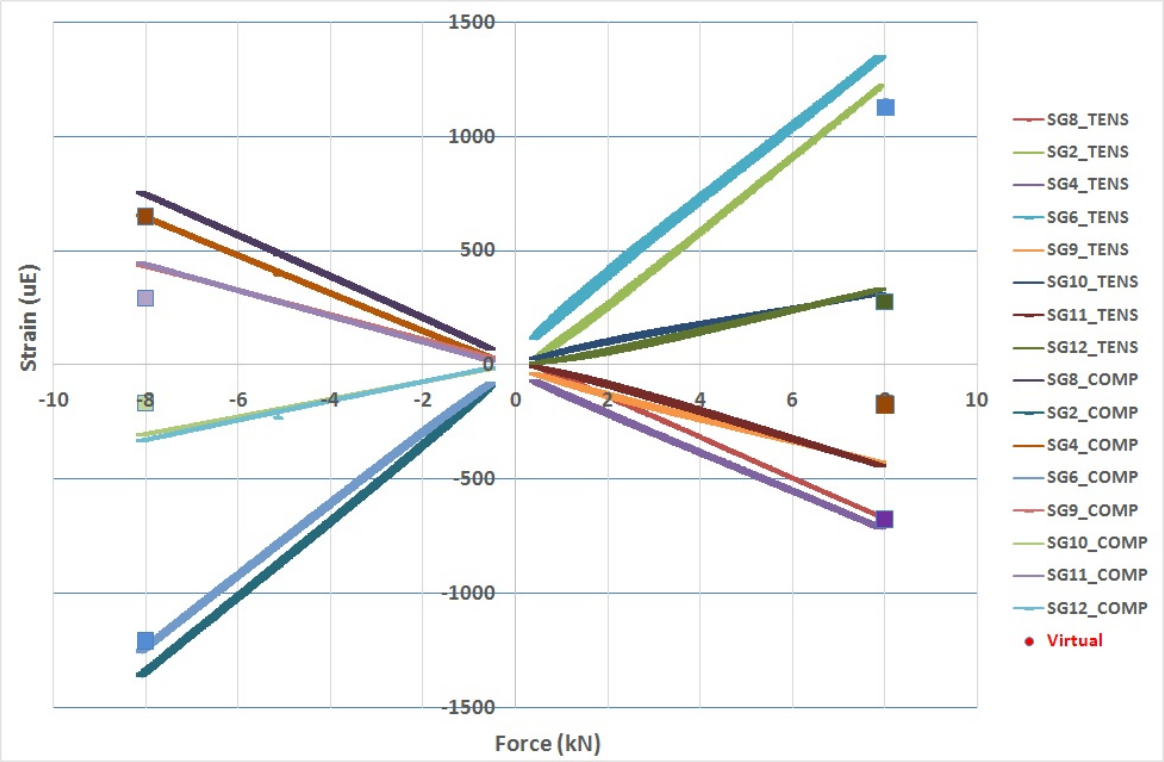

Figure 4.7. Comparison of the measured values with FEA in y-direction (LC1).

Examining the data obtained from measurements, it can be stated that strain gages 2 and 6 work in the same direction as the load is applied whereas strain gages 4 and 8 work in the opposite direction, as expected. Although the strain gages bonded at the opposite faces of the bridges of the load cell (SG4 and SG8 for example) are expected to read the same values, the strain values deviate from each other as the load increases and they yield different slopes for load versus strain curves. These aspects indicate that there may be still slight misalignment in the fixture resulting in unexpected moments.

Force in z-direction is varied between 0.1 N to 10 kN in tension and -0.1 to -10 kN in compression. From the Figure 4.8 and it can be seen that outputs behave almost perfectly as expected, strain gages 5,6,7,8 read positive strain values while 1,2,3,4 strain gages read negative strain values.

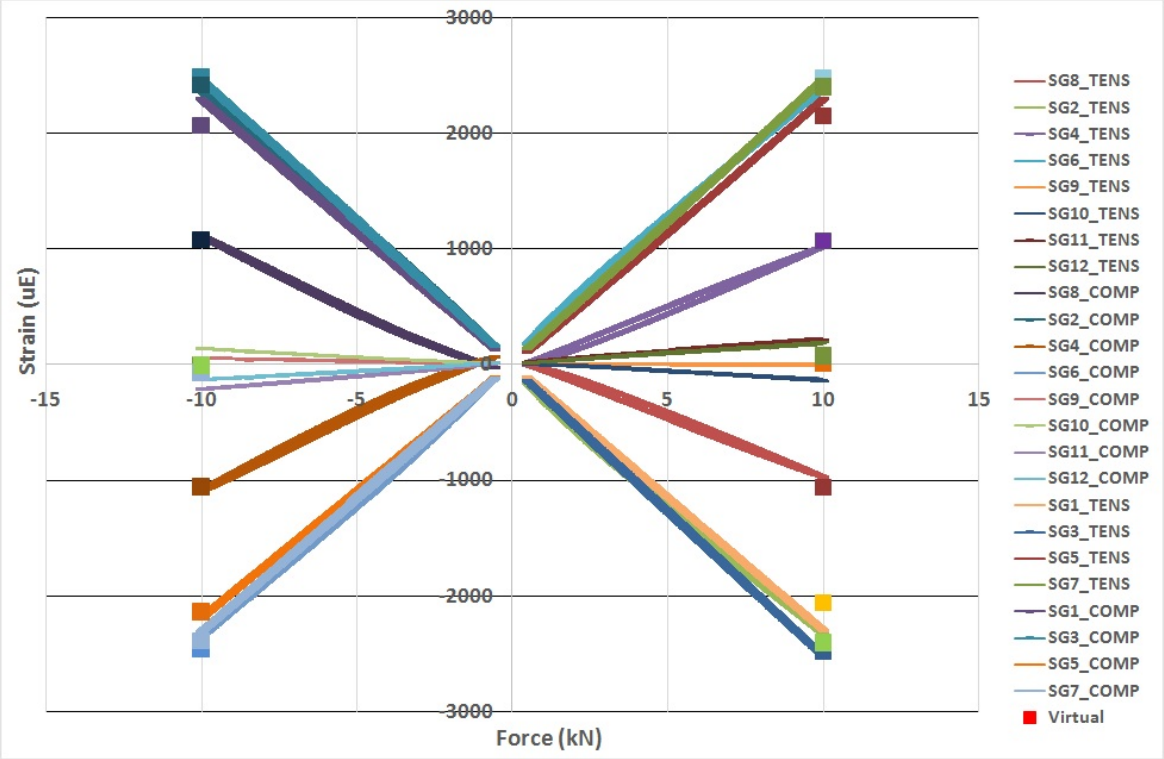

Figure 4.8. Comparison of the measured values with FEA in z-direction (LC1).

In order to obtain the data for pure moment, strain values corresponding to each force value is subtracted from the measurement thanks to linear superposition theory. Knowing that the moment arm is 1 meter, moments vary between 0 Nm and 40 Nm for M_x, 20 Nm for M_y, and 25 Nm for M_z due to weights of 0.8 kg hanged during the test. Figures 4.9, 4.10 and 4.11 show the comparison of physical and virtual calibration for moments for LC1.

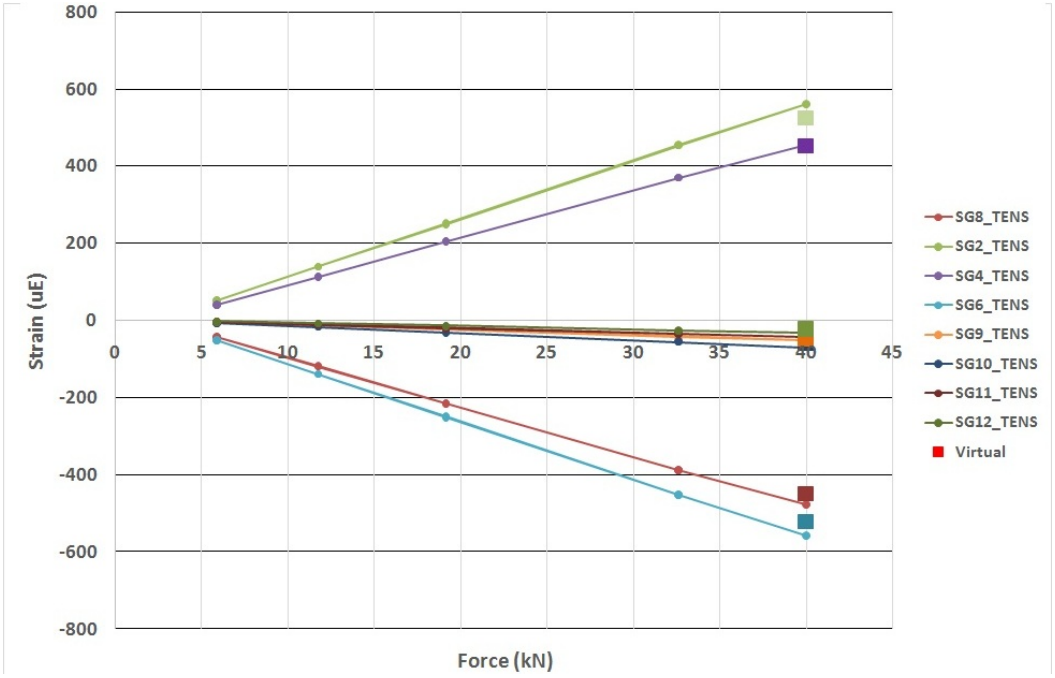

Figure 4.9. Comparison of the measured values with FEA for moment in x-direction (LC1).

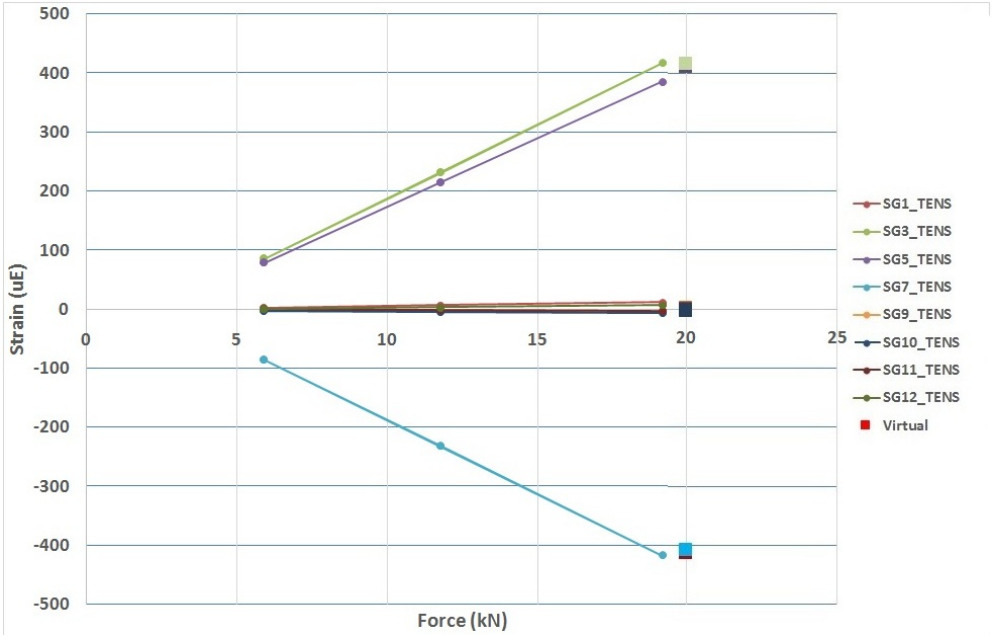

Figure 4.10. Comparison of the measured values with FEA for moment in y-direction (LC1).

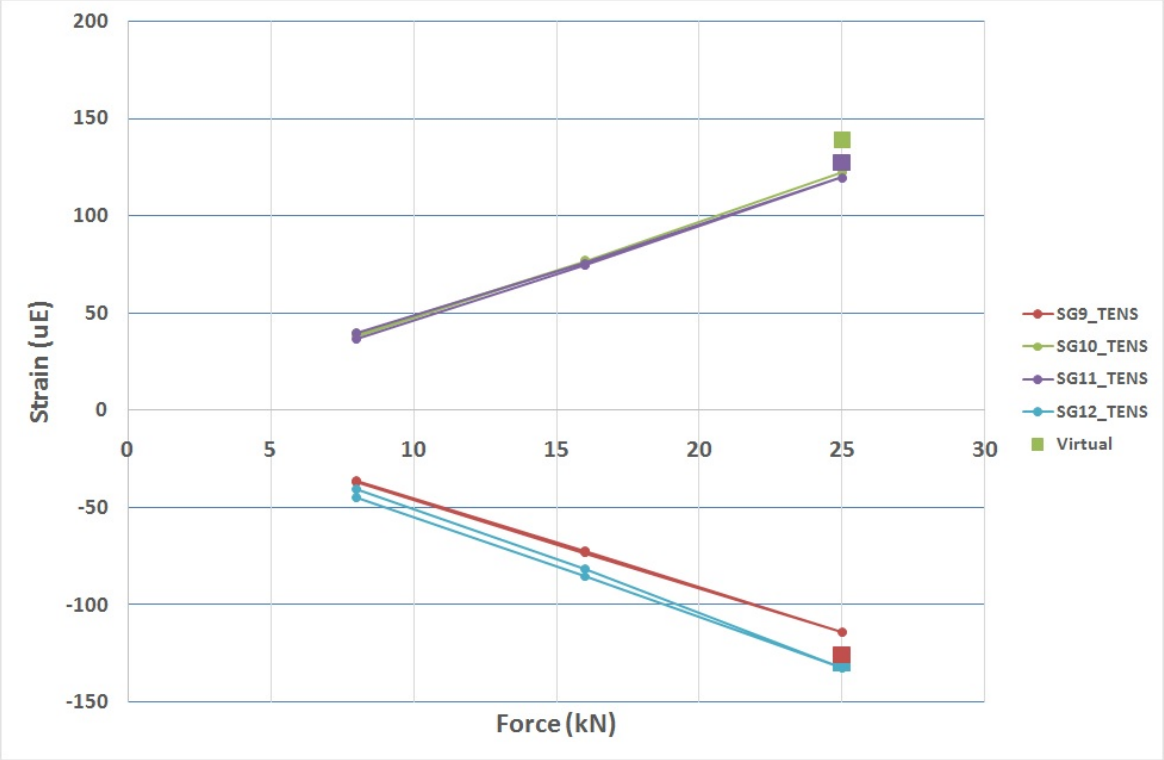

Figure 4.11. Comparison of the measured values with FEA for moment in z-direction (LC1).

It can be stated that although there is a discrepancy between the measured response of the strain gages and the strain at maximum load calculated by FEA, the sensitivity of the load cell for different load components is reasonably accurate. Nevertheless, data analysis of the load cell revealed that it can be used in force and moments. Although the discrepancy between the measured and simulated values are small, it is believed that this discrepancy results from the misalignments in the test fixture and the virtual calibration Matrix can be used for force and moment measurements.

4.4. Fatigue Analysis Results

4.4.1. Fatigue Calculations for Abuse Loading

Before beginning with determination of safety factors against fatigue failure, corrected endurance limit for this design must be calculated [35]. Corrected endurance limit is given by:

$$S_n = S_{n'} C_L C_G C_S C_T C_R \tag{4.11}$$

Where C_L is the load factor, C_G is the gradient(size) factor, C_S is the surface factor, C_T is the temperature factor and C_R is the reliability factor. C_L, C_G and C_T can be taken to be equal to 1. Surface factor C_S is taken to be 0.85 for a machined and then commercially polished surface. C_R is chosen to be 0.897 for 90% reliability. Endurance limit $S_{n'}$ is found for steels as follows:

$$S_{n'} = 0.5 S_u for S_u \leq 1400 MPa \tag{4.12}$$

$$S_{n'} = 700 Mpa for S_u \geq 1400 MPa \tag{4.13}$$

Since the ultimate tensile strength of the selected material is higher than 1400 MPa, the uncorrected endurance limit, $S_{n'}$, comes out to be 700 MPa.

The corrected endurance limit is:

$$S_n = (700 MPa) X (0.897) X (0.85) = 533.7 Mpa \tag{4.14}$$

For simplicity, cyclic loads are assumed varying between maximum and minimum values which are opposite in signs and there is no mean stress. Variation of stress as a function of time for loading between F_{max} and $-F_{min}$ is illustrated in Figure 4.12.

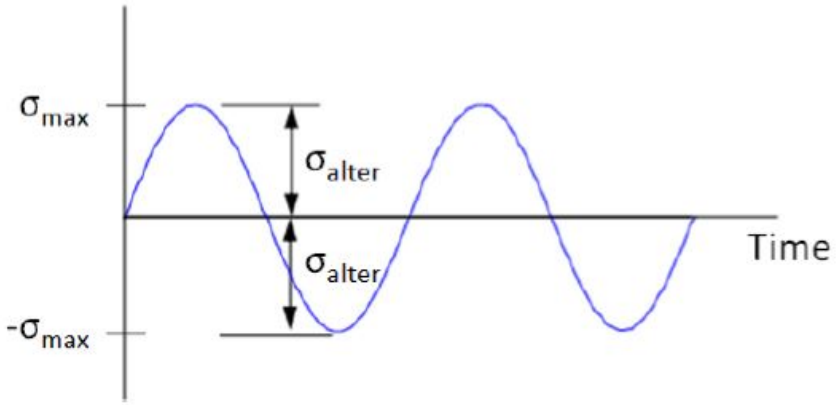

Figure 4.12. Cyclic loading showing the alternating stress

Table 4.5 presents the factors of safety against fatigue for all loading cases.

Table 4.5. Safety factors against fatigue for several loading states for Load Cell.

Loading state	**von Mises Stress (MPa)**	**Endurance Limit**	**Safety Factor Against Fatigue**
$F_x = \pm 20$	508	533.7	1.05
$F_y = \pm 8$	153	533.7	3.48
$F_z = \pm 10$	411	533.7	1.29
$M_x = \pm 40$	111	533.7	4.80
$M_y = \pm 20$	78	533.7	6.84
$M_z = \pm 20$	73	533.7	7.31

It should be kept in mind that these load amplitudes are for low cycle fatigue under abuse loading for accelerated durability tests. In service history, the load amplitudes will probably never encounter and they are just a rough estimate anyway. Hence it is concluded that the design is safe and durable for service history determination.

- Damage Analysis Results For Test Track

The strain data is obtained from one of the test tracks which is shown in Figure 4.13.

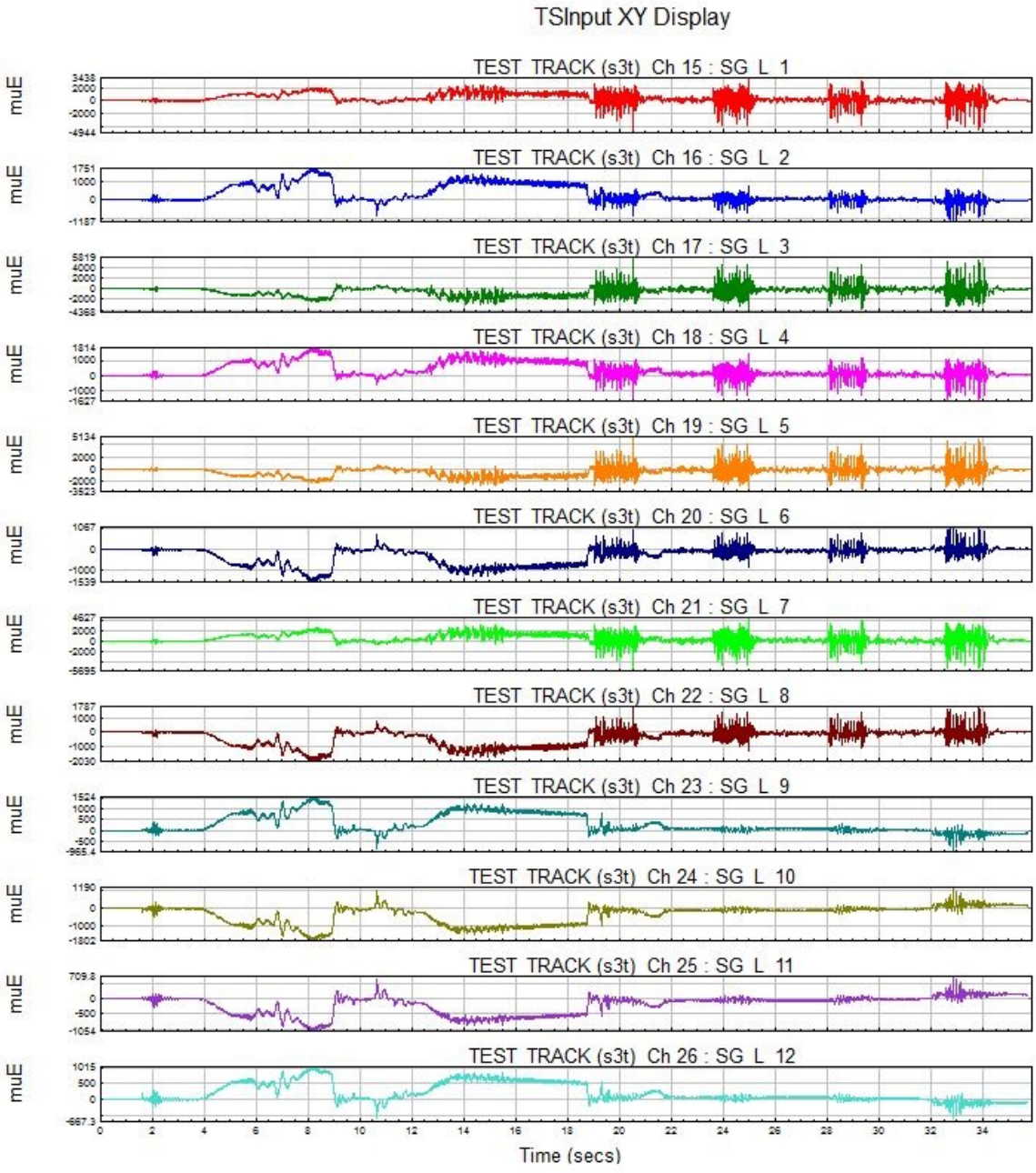

Figure 4.13. Strain signals obtained from the test track.

These strain inputs are then subjected to manipulation using Equations 4.7 to 4.12. The strain values can be considered as measurement obtained from virtual strain gages from the test track. It is to be noted that both the virtual and physical calibration matrix is used. Figure 4.14 shows the load history that is obtained by

using the calibration matrix.

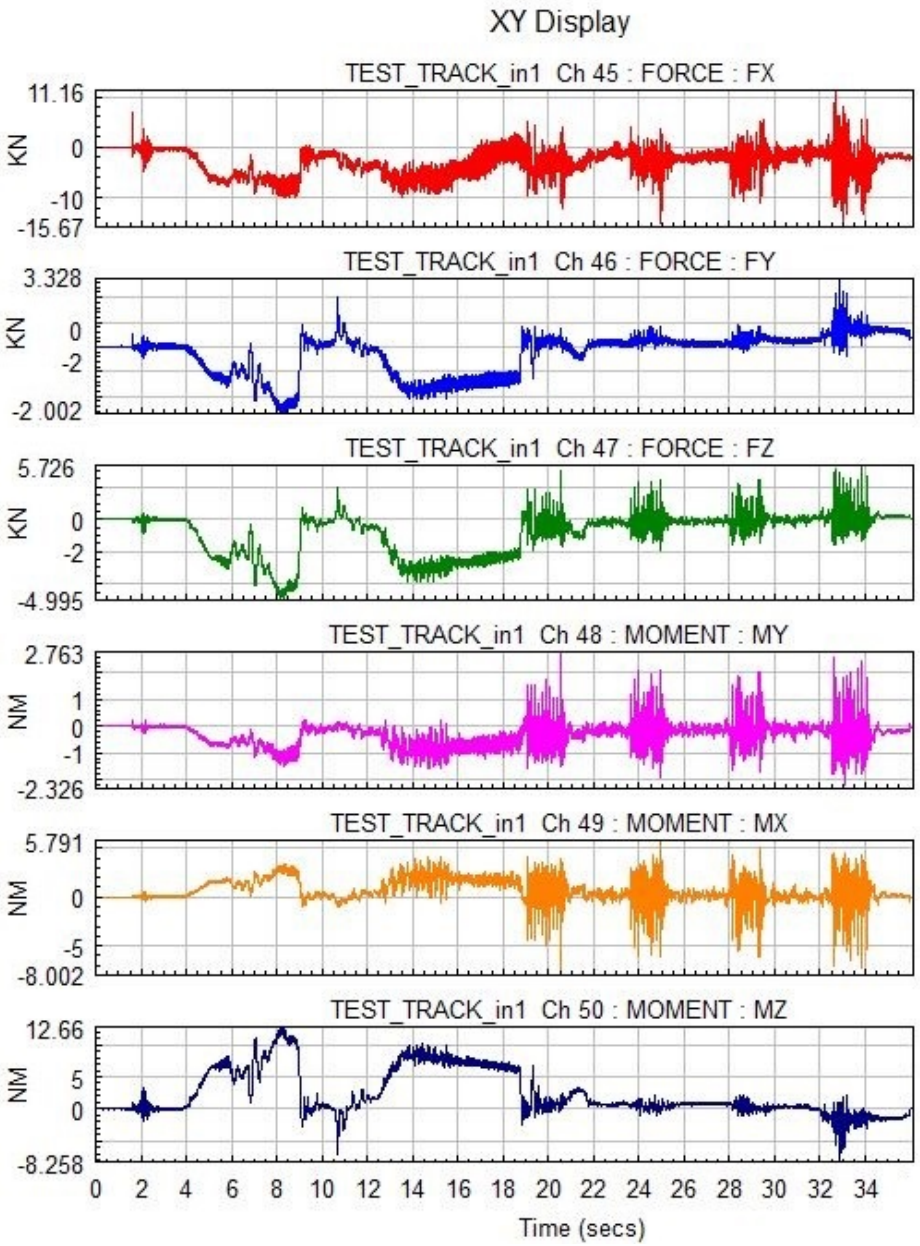

Figure 4.14. Load signals obtained from back calculation.

The 10 most damaged regions of the model (hotspots) are presented in Tables 4.6 and 4.7. These are the parts that are most likely to fail, or which are the weakest parts of the design.

Table 4.6. Fatigue life estimation of hot spots based on physical calibration matrix (design 1).

Hotspots	Node Number	Damage	Plane angle (degrees)	Mean biaxiality ratio	Non-proportionality	Dominant stress degree	Max Stress (Mpa)	Life (repeats)
1	482	4.96e-06	170	0.2659	0.07158	-14.51	1471	3.371e+05
2	481	4.824e-06	160	0.2659	0.07158	-14.51	1469	3.283e+05
3	5791	4.479e-06	160	0.3139	0.07526	-23.9	1462	3.06e+05
4	5790	4.282e-06	150	0.3139	0.07526	-23.9	1458	2.935e+05
5	7743	3.794e-06	100	0.4935	0.07968	-78.96	1416	2.636e+05
6	7742	3.613e-06	110	0.5458	0.07458	-73.72	1342	2.768e+05
7	5761	3.434e-06	100	0.5458	0.07458	-73.72	1337	2.912e+05
8	5762	3.332e-06	0	0.2659	0.07158	-14.51	1330	3.001e+05
9	346	3.236e-06	110	0.3139	0.7526	-78.96	1324	3.091e+05
10	5732	3.133e-06	150	0.4529	0.07859	-14.51	1320	2.343e+05

Table 4.7. Fatigue life estimation of hot spots based on virtual calibration matrix (design 1).

Hotspots	Node Number	Damage	Plane angle (degrees)	Mean biaxiality ratio	Non-proportionality	Dominant stress degree	Max Stress (Mpa)	Life (repeats)
1	482	6.276e-06	170	0.2659	0.07158	-14.51	1464	4.281e+05
2	481	6.151e-06	160	0.2659	0.07158	-14.51	1460	4.213e+05
3	5791	5.69e-06	160	0.3139	0.07526	-23.9	1454	4.058e+05
4	5790	5.438e-06	150	0.3139	0.07526	-23.9	1452	3.839e+05
5	7743	3.88e-06	100	0.4935	0.07968	-78.96	1410	3.578e+05
6	7742	3.694e-06	110	0.5458	0.07458	-73.72	1380	3.707e+05
7	5761	3.509e-06	100	0.5458	0.07458	-73.72	1382	3.849e+05
8	5762	3.405e-06	0	0.2659	0.07158	-14.51	1362	2.937e+05
9	346	3.306e-06	110	0.3139	0.7526	-78.96	1330	3.025e+05
10	5732	3.2e-06	150	0.4529	0.07859	-14.51	1320	3.192e+05

Figures 4.15 and 4.16 show the damage FE display based on physical and virtual calibration matrices respectively. The nodes are the hotspots indicated in Tables 4.6 and 4.7.

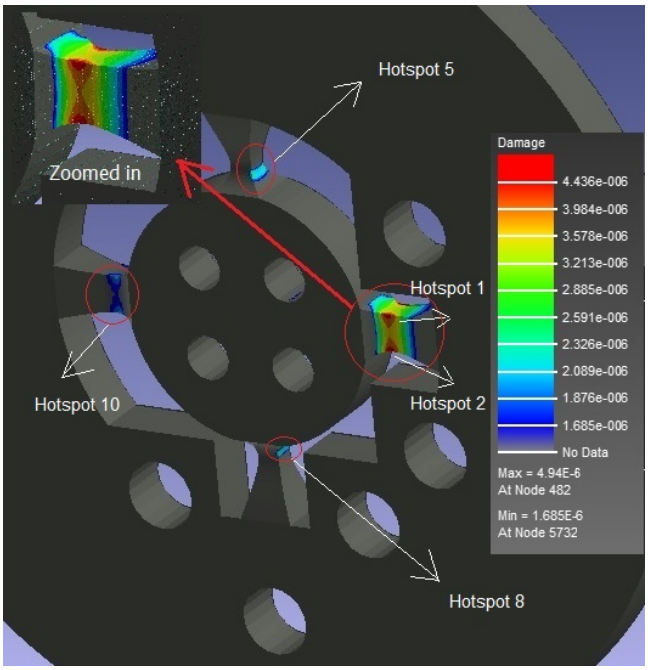

Figure 4.15. Damage calculation of combined loads based on physical calibration matrix (Design 1).

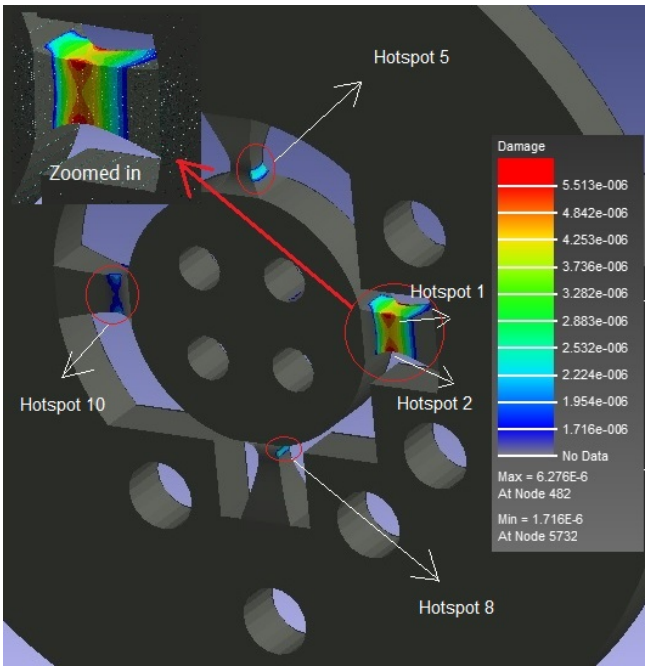

Figure 4.16. Damage calculation of combined loads based on virtual calibration matrix (Design 1).

Comparing the Tables 4.6 and4.7 we can see that the life cycle repeats are lower based on virtual matrix and the damages are higher accordingly. This shows that using physical calibration matrix results in shorter lives. It is to be noted that the total damage is inverse of the number of repeats. Analysis of the Figures 4.15 and 4.16 above shows that there are no indications of fatigue failure nor degradation of load cell performance outside specified limits, which is 10000 cycles in this particular test track. Actually the load cells survived the durability test without any fatigue damage, during the verification test program.

4.5. Error Results

The aim of the error analysis performed is to understand the effect of misalignments in strain gage bonding.

4.5.1. Estimating Errors

Table 4.8 shows the RMS error of the load cell in F_x, F_y, F_z, M_x, M_y, M_z directions for Parallel, Angle Misaligned and Physical calibration strain gages in a test.

Table 4.8. Percent RMS error in load cell due to parallel, angle misalignment and physical calibration.

		F_x	F_y	F_z	M_y	M_x	M_z
Design-1	**Parallel**	2.34	1.125	0.39	3.6	23.6	17.5
	Angle	8.6	2.5	1.66	5.09	27.14	10
	Physical	3.91	1.032	2.85	8.39	2.22	1.61

Below Figures 4.17 to 4.22 compare the force versus time graphs of perfectly bonded strain gages of virtual calibration for physical calibration test. The blue lines represent the loads expected to be read if the strain gages are perfectly bonded for virtual calibrated test given in Equation 4.7 (FE), whereas the red lines represent perfectly bonded strain gages for physical calibrated tests given in Equation 4.9 (EXP).

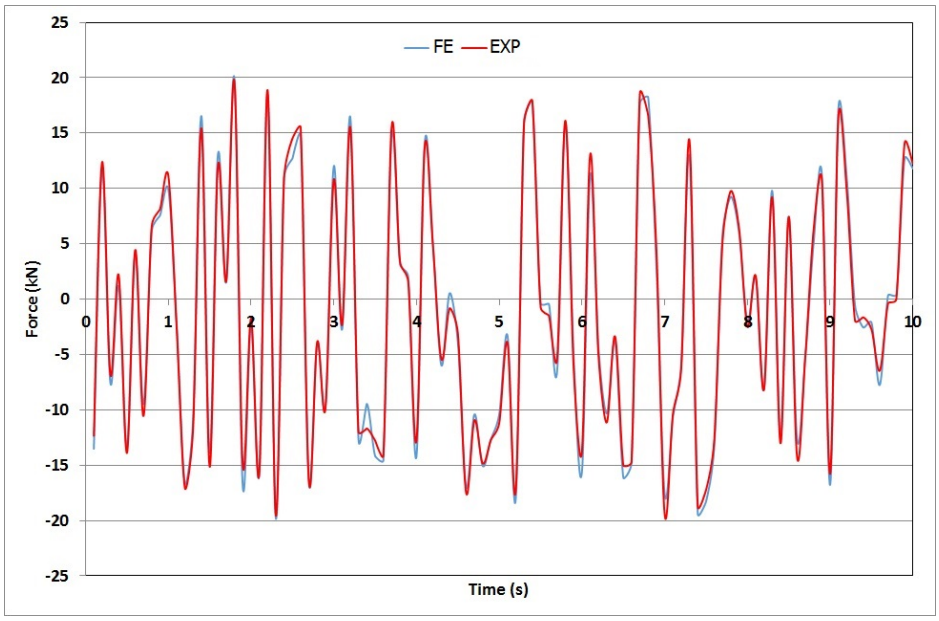

Figure 4.17. Real and measured load signals of F_x for physical calibration of load cell Design 1.

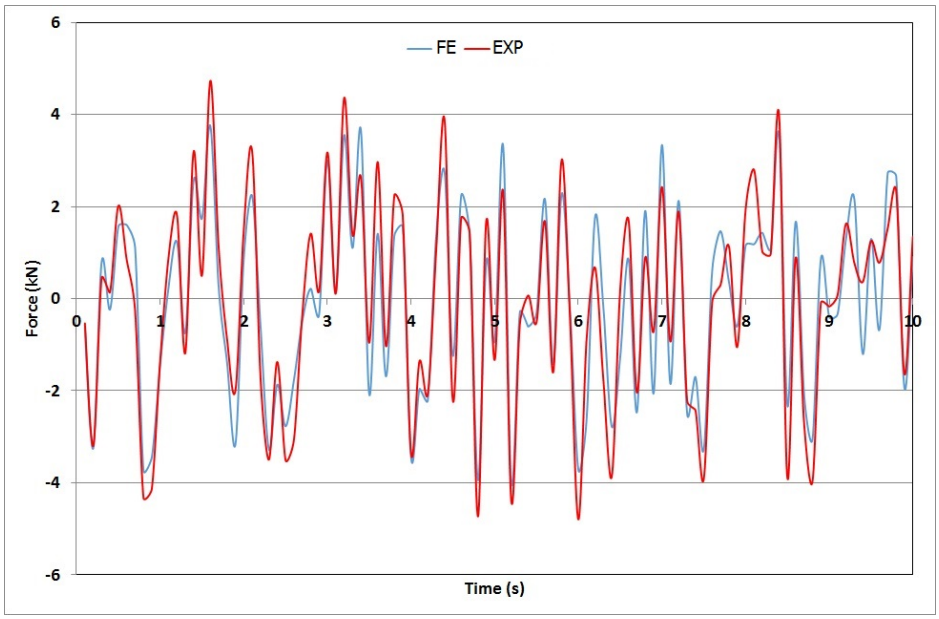

Figure 4.18. Real and measured load signals of F_y for physical calibration of load cell Design 1.

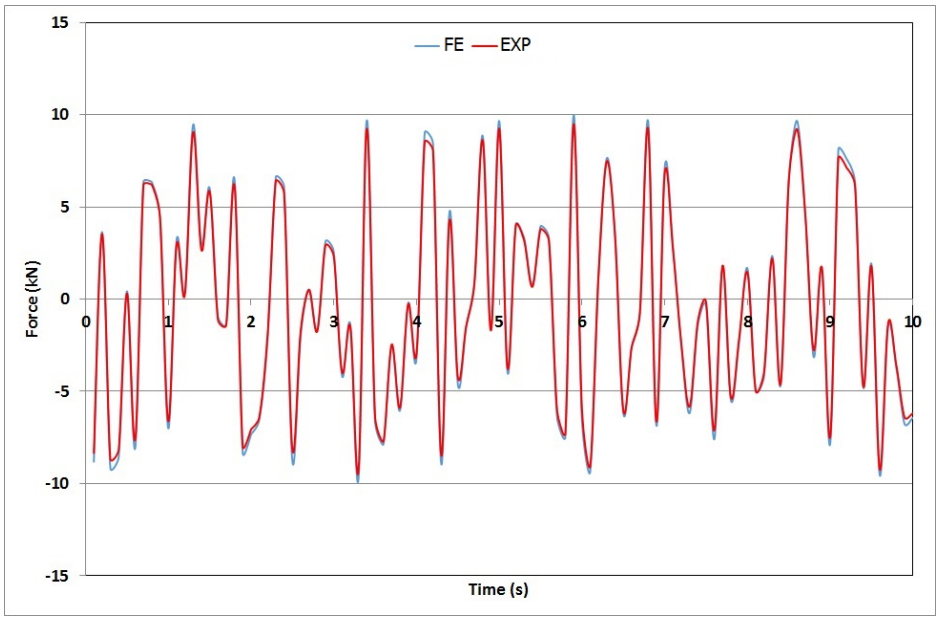

Figure 4.19. Real and measured load signals of F_z for physical calibration of load cell Design 1.

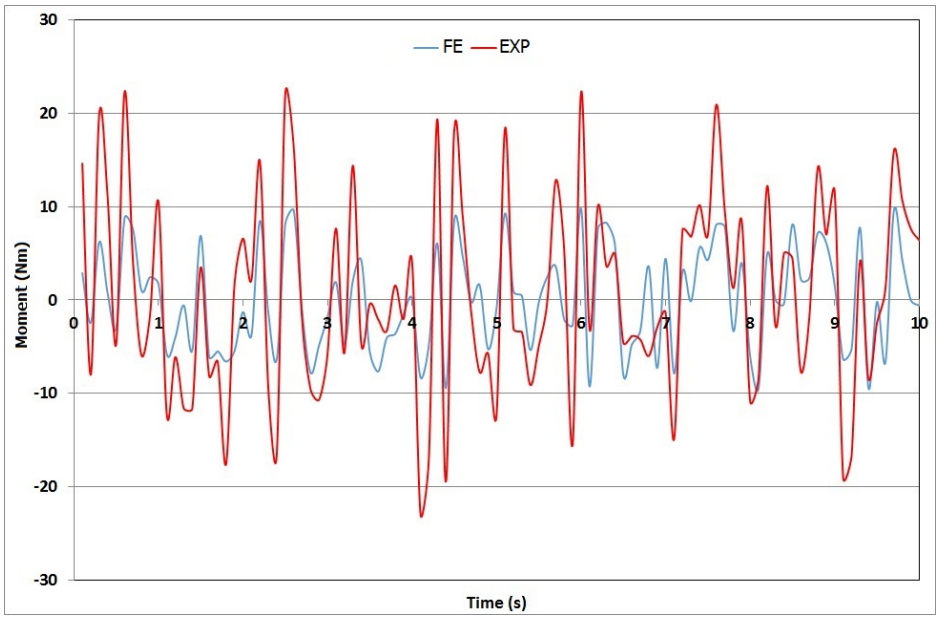

Figure 4.20. Real and measured load signals of M_y for physical calibration of load cell Design 1.

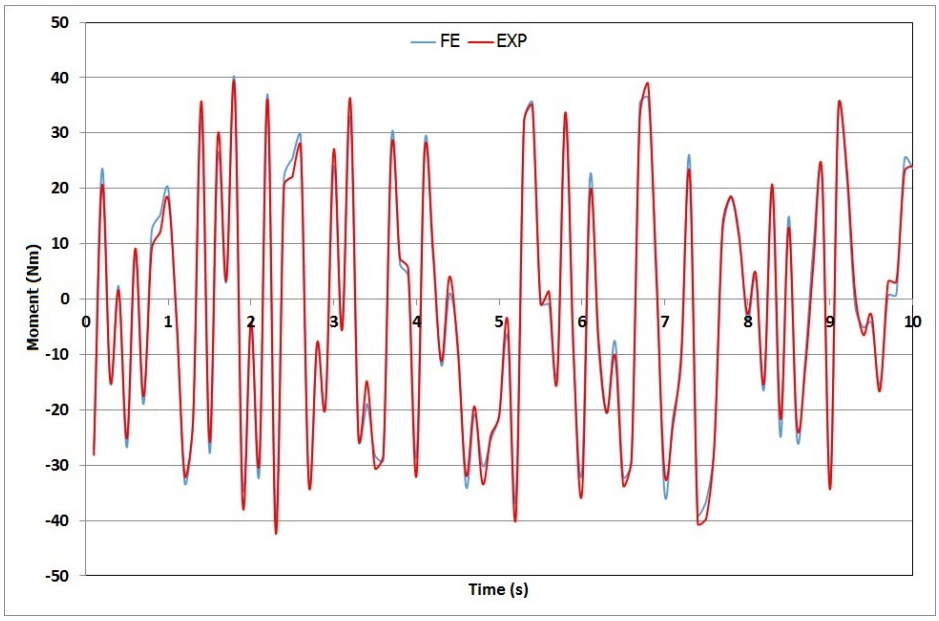

Figure 4.21. Real and measured load signals of M_x for physical calibration of load cell Design 1.

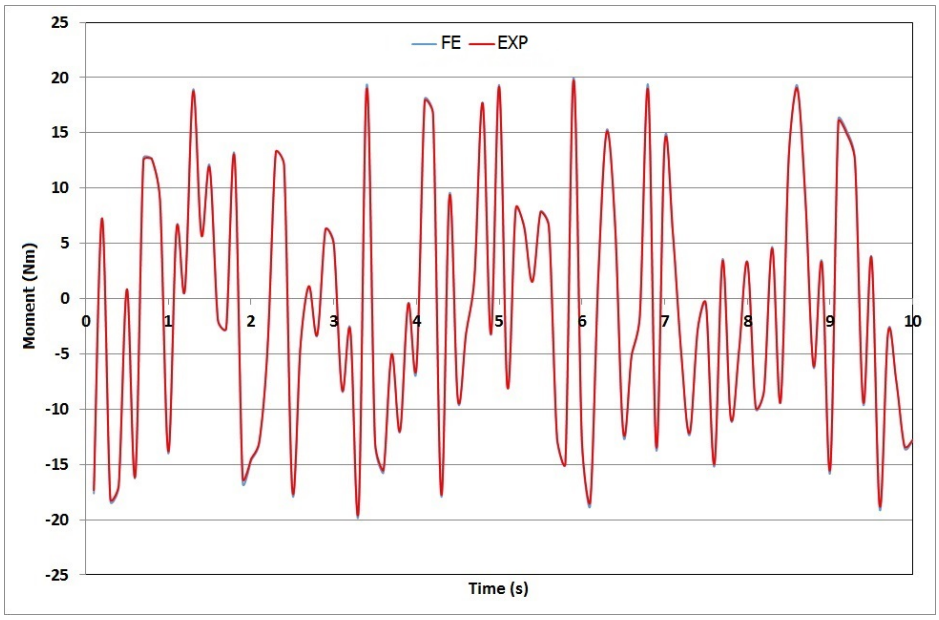

Figure 4.22. Real and measured load signals of M_z for physical calibration of load cell Design 1.

Graphs above show that the highest error is in the M_x error graph which is more sensitive than the others. A new design of the load cell that is discussed in Section 5.11 gives better error results when compared with this load cell. Figures 4.23 to 4.28 show the percentage of difference between real and measured load data for 100 data points obtained from physical calibrations:

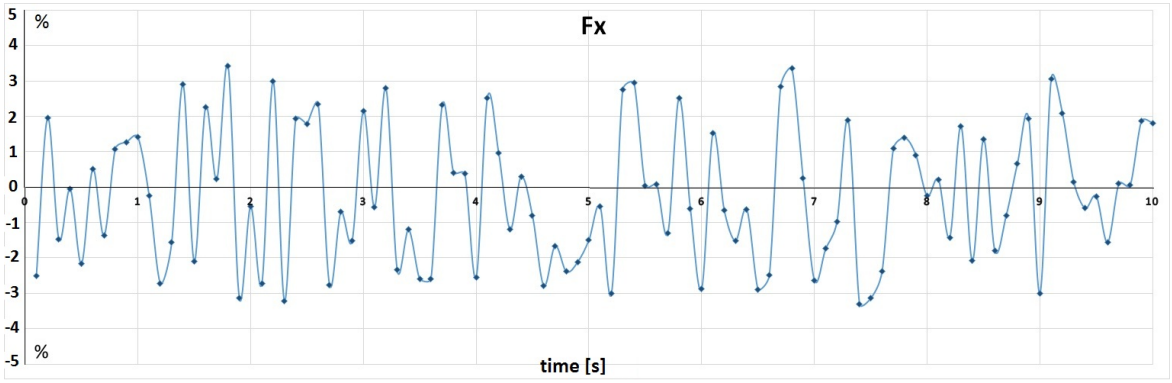

Figure 4.23. Percent difference of real and measured load values of F_x for physical calibration of load cell Design 1.

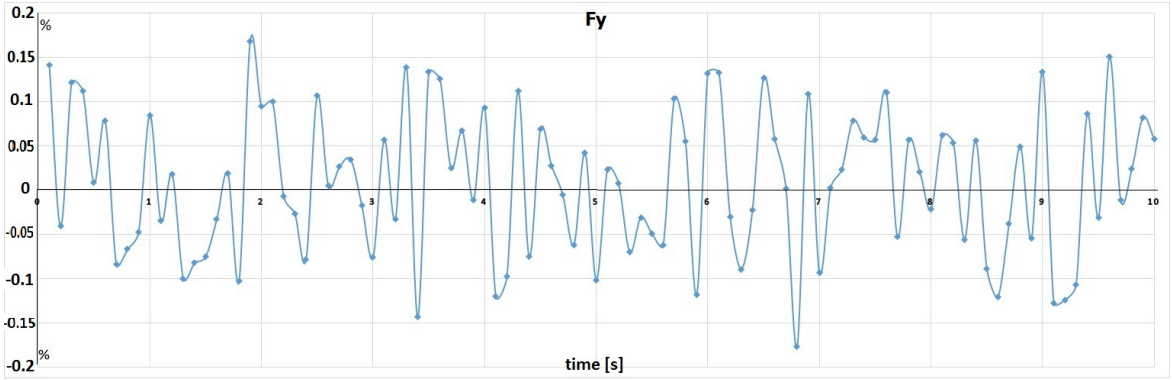

Figure 4.24. Percent difference of real and measured load values of F_y for physical calibration of load cell Design 1.

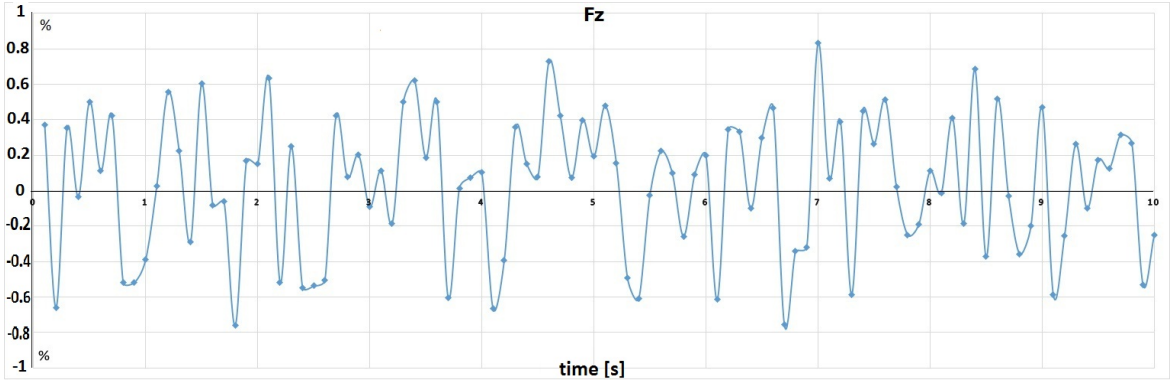

Figure 4.25. Percent difference of real and measured load values of F_z for physical calibration of load cell Design 1.

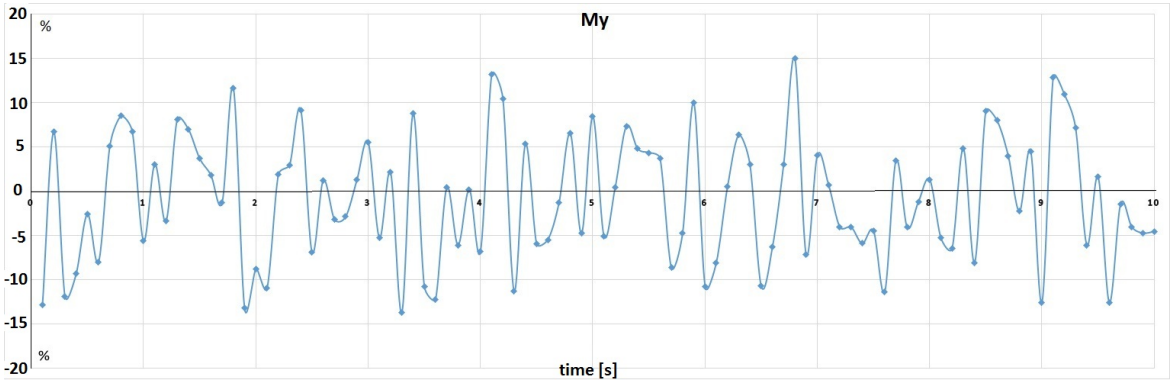

Figure 4.26. Percent difference of real and measured load values of M_y for physical calibration of load cell Design 1.

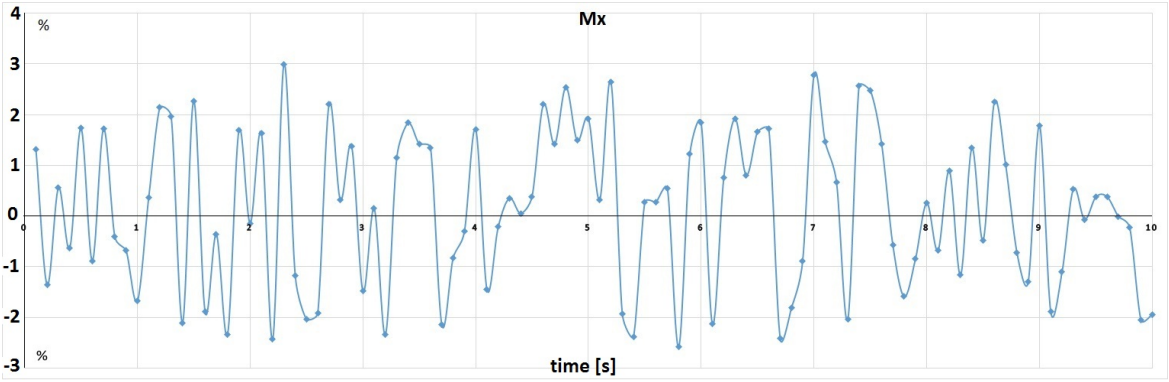

Figure 4.27. Percent difference of real and measured load values of M_x for physical calibration of load cell Design 1.

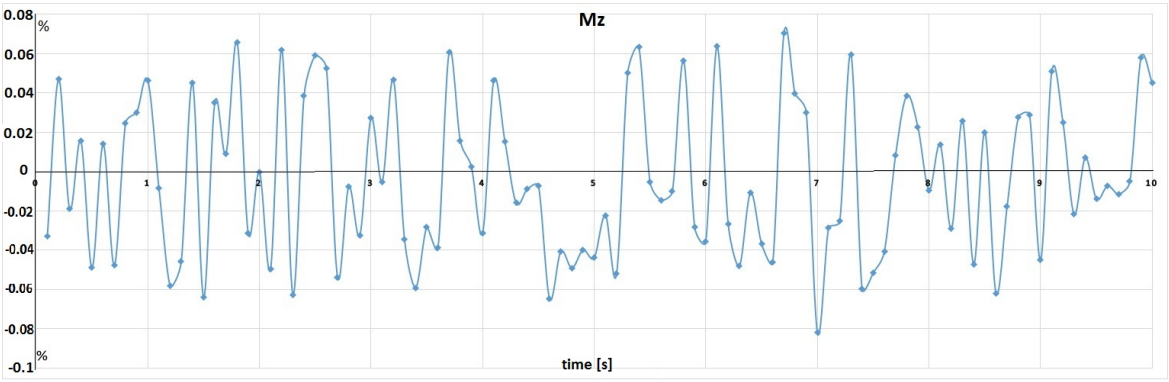

Figure 4.28. Percent difference of real and measured load values of M_z for physical calibration of load cell Design 1.

5. DISCUSSION

5.1. Modification of the Load Cell

5.1.1. Added Features

The load cell geometry proposed has been altered by adding some slots behind the measuring bridges in order to reduce the crosstalk between the measuring channels and strain gage mounting errors and to reduce the interference error of bending moment when forces are applied along different axes.

Several different slots with different dimensions have been drawn using 3D software and analyzed with a finite element method and the final optimized design is shown in Figure 5.2. The dimensions of the slots have been chosen regarding the thickness of the load cell and the placement of holes on the outer ring, where fixtures are fixed to during , shown in calibration as Figure 5.1.

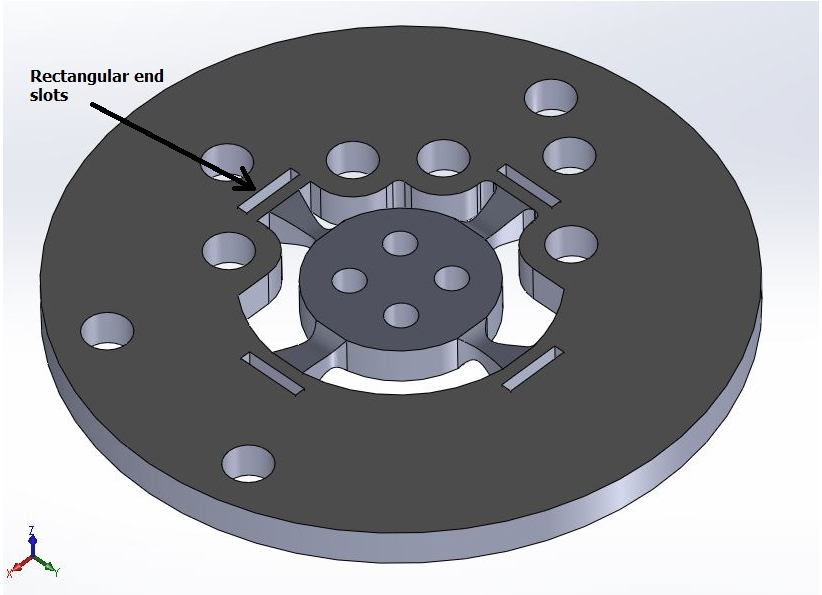

Figure 5.1. Geometry of the load cell with rectangular slots.

The end of the slots have been changed to a circular form for better fatigue durability and freedom of the movement of the bridges when loads are applied specially in x and y axes. This is shown in Figure 5.2.

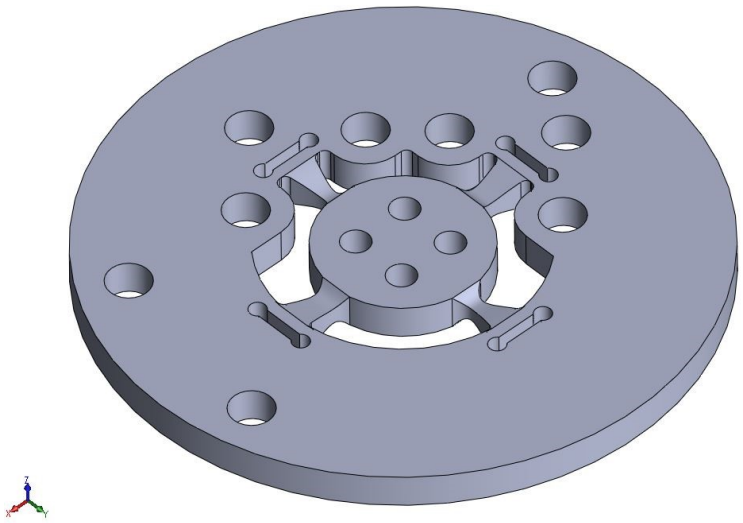

Figure 5.2. Final geometry of the load cell with circular end slots.

The basic dimensions of the load cell is given in Figure 5.3. The dimension measurements are in mm. This design enables displacement of the center ring and reduces cross-talk between the load channels as well as errors in moment measurements due to strain gage misalignment. [36]

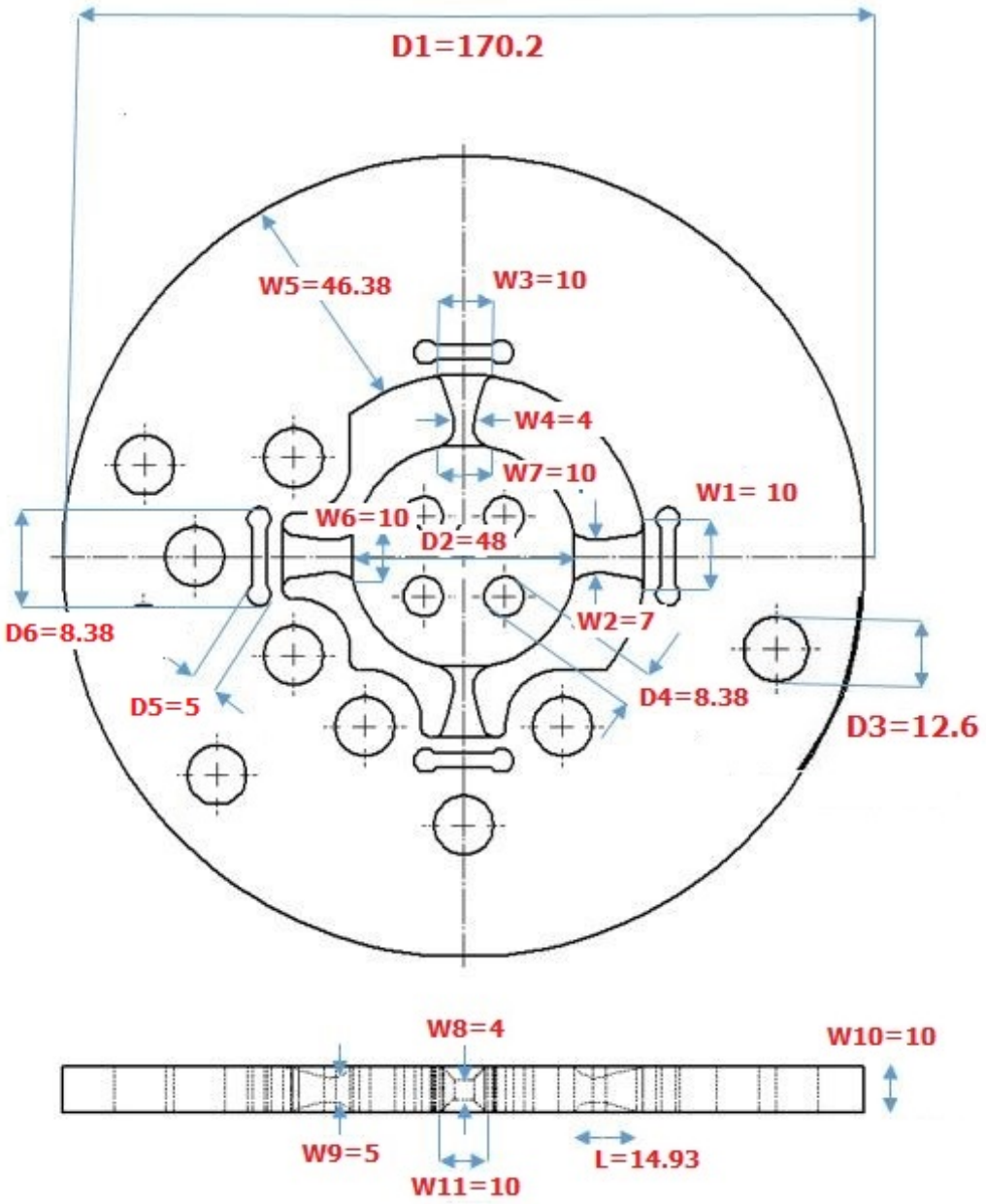

Figure 5.3. Dimensional design parameters for Design 2.

The placement of the strain gages is exactly the same as the manufactured load cell. Locations of these strain gages are illustrated in Figure 5.4.

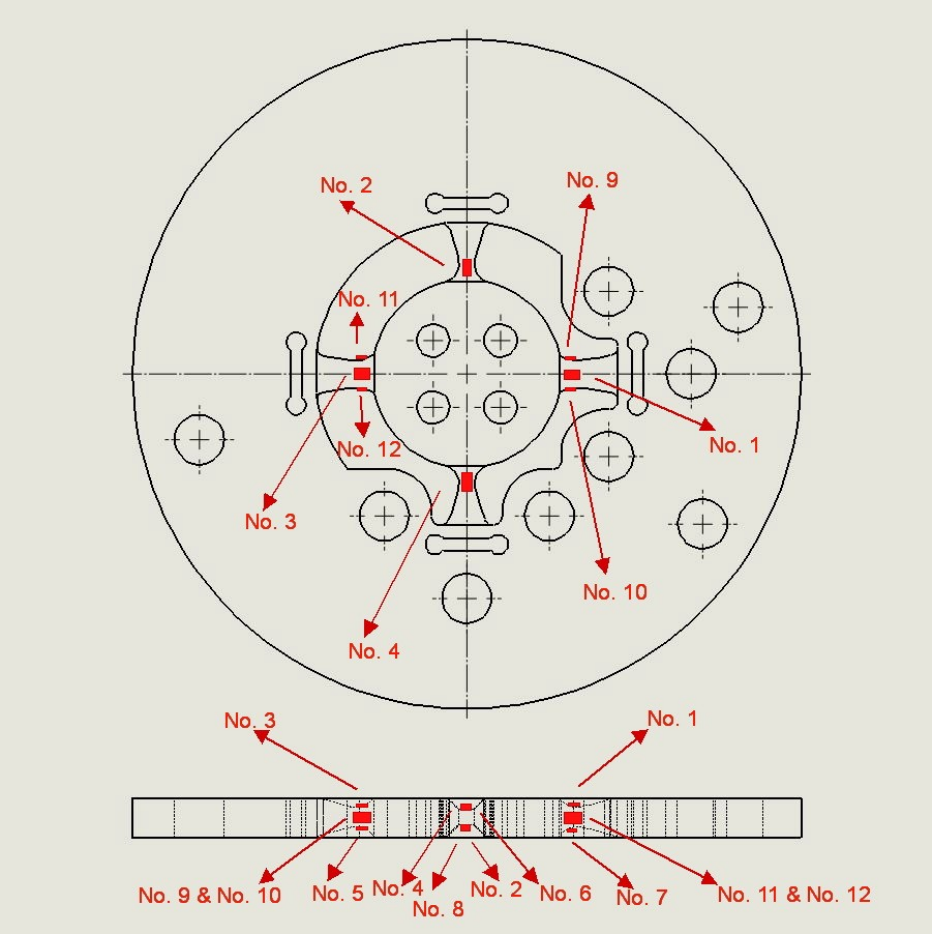

Figure 5.4. Locations of strain gages.

5.1.2. Virtual Calibration of the Load Cell

The procedure for calculating the calibration matrix for Design 2 load cell is the same as the one done for the manufactured load cell as explained in chapter 3 section 3.2. Calibration matrix is the matrix relating the load vector to the strain values measured by strain gages. Table 5.1 shows the values of strain to be measured by each strain gage for each loading case in FEA.

Table 5.1. Strain values obtained at each strain gage location for each loading cases.

	$\mathbf{F}_x$ **(20 kN)**	$\mathbf{F}_y$ **(8 kN)**	$\mathbf{F}_z$ **(10 kN)**	$\mathbf{M}_y$ **(20 Nm)**	$\mathbf{M}_x$ **(40 Nm)**	$\mathbf{M}_z$ **(20 Nm)**
SG1	1398	18	-1585	7	394	-6
SG2	-148	-284	-1790	317	1	-1
SG3	-816	17	-1516	5	-397	-7
SG4	-165	467	-1461	-327	5	0
SG5	1390	18	1590	7	-394	-6
SG6	-147	-284	1798	-317	1	-1
SG7	-815	18	1520	5	397	-6
SG8	-166	465	1468	328	5	0
SG9	1250	181	-3	0	0	222
SG10	1242	-216	-3	0	0	-236
SG11	-718	185	-3	0	0	-203
SG12	-744	-217	-4	0	0	191

By using the values presented in Table 5.1, the entries of the Matrix S are given in Table 5.2.

Table 5.2. The entries of the Matrix S for design 2.

	$\mathbf{F}_x$ **(20 kN)**	$\mathbf{F}_y$ **(4 kN)**	$\mathbf{F}_z$ **(10 kN)**	$\mathbf{M}_y$ **(20 Nm)**	$\mathbf{M}_x$ **(40 Nm)**	$\mathbf{M}_z$ **(20 Nm)**
e1	221	0	0	0	0	0
e2	-2	375	0	0	0	0
e3	0	0	-1273	-1	0	0
e4	0	-1	-24	64	0	0
e5	0	0	-9	0	40	0
e6	-1	-1	0	0	0	43

As can be seen from the Table 5.1, The manipulated strain values, which can be considered as measurement obtained from virtual strain gages, are calculated from Equations 4.1 to 4.6. For this design Equation 4.5 is changed as shown below:

$$e_5 = (2.5\varepsilon_1 - \varepsilon_3) - (2.5\varepsilon_5 - \varepsilon_7) \tag{5.1}$$

In Equation 4.5, ε_1 and ε_5 have been multiplied by 2.5 in order to diagonalize the strain values in Table 5.2. By calculating the inverse of that matrix, calibration matrix [C5] is obtained. Virtual calibration matrix for the load cell in tension is shown in Equation 5.2 for tension, and 5.3 for compression:

$$\begin{Bmatrix} F_x \\ F_y \\ F_z \\ M_y \\ M_x \\ M_z \end{Bmatrix} = \begin{bmatrix} \mathbf{4526} & -4 & 1 & -12 & 1 & 0 \\ 22 & \mathbf{2665} & 0 & 0 & -14 & -4 \\ 1 & 0 & \mathbf{-785} & -13 & -3 & -1 \\ 12 & 24 & -83 & \mathbf{15507} & -6 & -1 \\ -51 & -11 & -42 & -4 & \mathbf{25299} & -20 \\ 94 & 73 & -2 & 0 & 0 & \mathbf{23483} \end{bmatrix} X10^{-6}. \begin{Bmatrix} e_1 \\ e_2 \\ e_3 \\ e_4 \\ e_5 \\ e_6 \end{Bmatrix} \quad (5.2)$$

$$\begin{Bmatrix} F_x \\ F_y \\ F_z \\ M_y \\ M_x \\ M_z \end{Bmatrix} = \begin{bmatrix} \mathbf{-4497} & 1 & -2 & -1 & -5 & 0 \\ -11 & \mathbf{-2660} & 0 & 0 & -14 & 0 \\ 0 & 0 & \mathbf{779} & 10 & 1 & 5 \\ 1 & -16 & 29 & \mathbf{-15501} & 8 & 2 \\ 27 & -11 & 13 & 2 & \mathbf{-25287} & -6 \\ -68 & -44 & 1 & 0 & 0 & \mathbf{-23476} \end{bmatrix} X10^{-6}. \begin{Bmatrix} e_1 \\ e_2 \\ e_3 \\ e_4 \\ e_5 \\ e_6 \end{Bmatrix} \quad (5.3)$$

5.1.3. Fatigue Analysis Results

Table 5.3 presents the factors of safety against fatigue for all loading cases.

The safety factor for F_x is lower than unity. It should be kept in mind that these load amplitudes are for low cycle fatigue under abuse loading for accelerated durability tests. In service history, the load amplitudes will probably never encounter, and the magnitude for F_x is just an rough estimate anyway. Hence it is concluded that the design is safe and durable for service history determination.

Table 5.3. Safety factors against fatigue for several loading states for Load Cell Design 2.

Loading state	**von Mises Stress (MPa)**	**Endurance Limit**	**Safety Factor Against Fatigue**
$F_x = \pm 20$	590	533.7	0.90
$F_y = \pm 4$	125	533.7	4.26
$F_z = \pm 10$	514	533.7	1.03
$M_x = \pm 40$	529	533.7	1.01
$M_y = \pm 20$	520	533.7	1.02
$M_z = \pm 20$	525	533.7	1.01

- Damage Analysis Results

Figure 5.5 shows the damage FE display based on virtual calibration matrix.

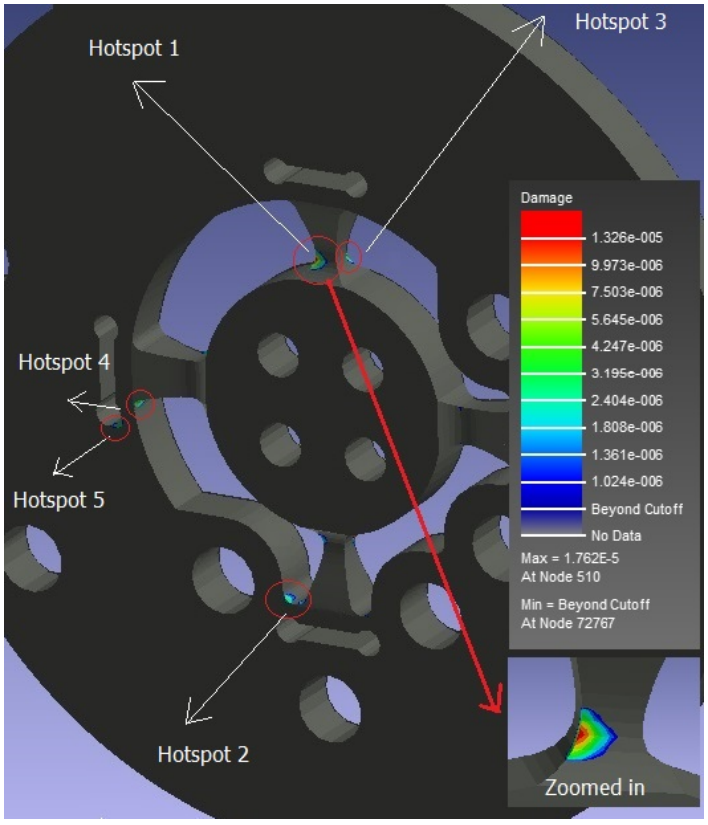

Figure 5.5. Damage calculation of combined loads based on virtual calibration matrix (Design 2).

The 10 most damaged regions of the model (hotspots) are presented in Table 5.4. These are the parts that are most likely to fail, or which are the weakest parts of the design.

Table 5.4. Life estimate due to service history for design 2.

Hotspots	**Node Number**	**Damage**	**Plane angle (degrees)**	**Mean biaxiality ratio**	**Non-proportionality**	**Dominant stress degree**	**Max Stress (Mpa)**	**Life (repeats)**
1	510	1.716e-05	160	0.1386	0.08654	-16.67	1686	5.826e+04
2	3546	1.586e-05	170	0.1386	0.08654	-16.67	1674	6.306e+04
3	7042	1.155e-05	150	0.1386	0.08654	-16.67	1662	8.659e+04
4	54574	9.314e-06	160	0.1351	0.08234	-19.41	1654	1.074e+05
5	1189	9.079e-06	0	0.1162	0.08103	-16.67	1641	1.101e+05
6	7043	8.721e-06	160	0.1162	0.08103	-16.31	1636	1.147e+05
7	1297	8.238e-06	170	0.04076	0.06358	-16.31	1624	1.214e+05
8	1586	7.749e-06	170	0.07919	0.05447	-13.51	1620	1.29e+05
9	54559	7.719e-06	170	0.7009	0.1282	-19.41	1613	1.323e+05
10	3848	7.557e-06	170	0.6553	0.05196	-14.58	1612	1.343e+05

As it can be seen from Table 5.4 for Design-2 as compared to Design-1, there is a reduction in damage calculation which shows an improvement in the design. Analysis of the Figure 5.5 above shows that there are no indications of fatigue failure nor degradation of load cell performance outside specified limits, for the critical load cell parameters of output, zero balance, nonlinearity, hysteresis, and creep, during or after completion of the Verification test program.

5.1.4. Error Results

Table 5.5 shows the percent RMS error of the load cell in F_x, F_y, F_z, M_x, M_y, M_z directions for both Parallel and Angle misaligned strain gages.

Table 5.5. Percent RMS error in Design-2 due to Parallel and Angle misalignment (in kN for forces and Nm for moments).

		Fx	**Fy**	**Fz**	**My**	**Mx**	**Mz**
Design-2	**Parallel**	4.25	0.625	5.66	4.95	0.975	6.5
	Angle	2.3	4.25	3.83	1.145	1.025	6.75

Comparing the RMS results for Design-2 given in Table 5.5 with for those for

Design-1 given in Table 4.8, it is obvious that the amount of difference in the original Design-1 load cell and the new Design-2 with fillets and slots enhance the strain distribution while slots make the load cell more flexible with respect to a twisting, hence reduces the RMS error. This comparison shows the significance of having slots at the end of the bridges.

From Figures 5.6 to 5.17 it can be clearly seen that the error is more predominant in moment measurements, and it significantly reduces with the new Design-2. Figures 5.6 to 5.17 compare the force versus time graphs for parallel misaligned, angle misaligned and perfectly bonded strain gages for different loads. The blue lines in these figures represent the loads expected to be read if the strain gages are perfectly bonded for virtual calibrated test given in Equation 5.2 (PB), whereas the red lines represent parallel misaligned (PM) and angle misaligned strain gages (AM), for virtually calibrated tests for Design 2 load cell.

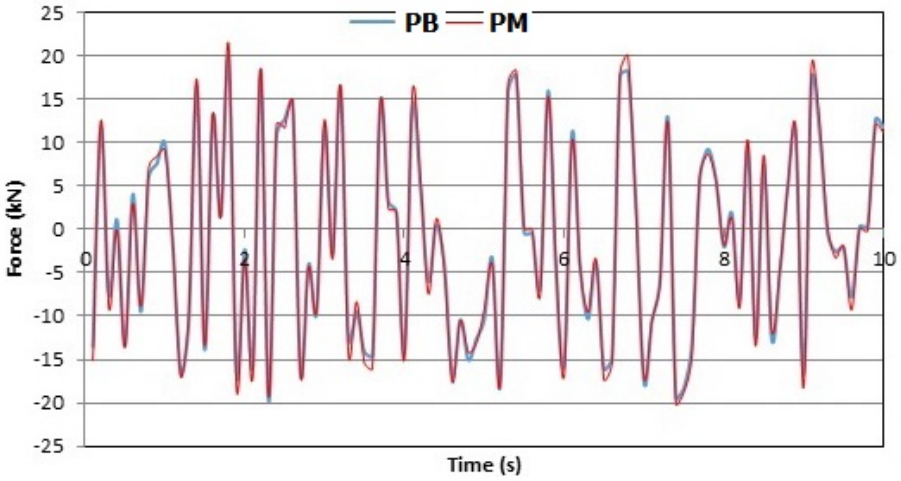

Figure 5.6. Parallel misaligned and perfectly bonded strain gage load signals F_x for Design 2.

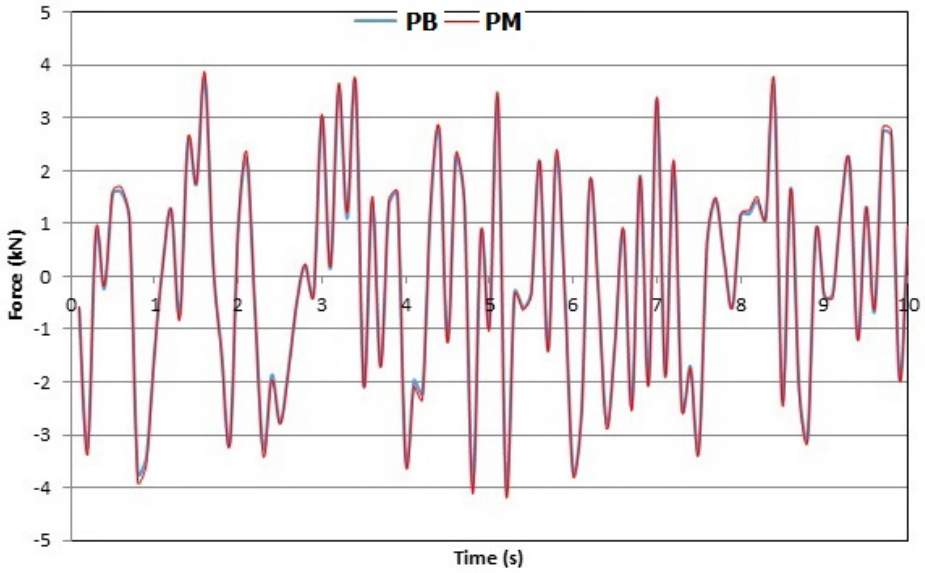

Figure 5.7. Parallel misaligned and perfectly bonded strain gage load signals F_y for Design 2.

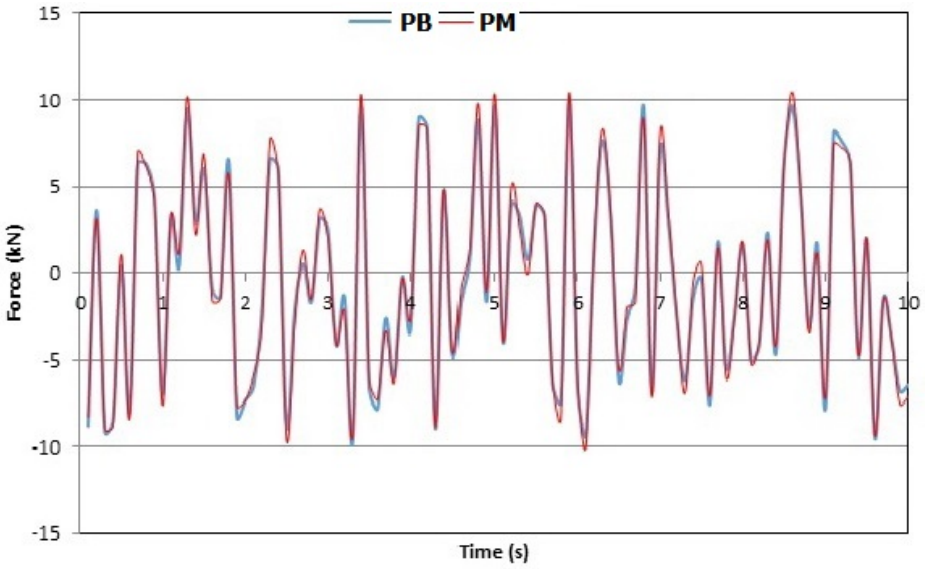

Figure 5.8. Parallel misaligned and perfectly bonded strain gage load signals F_z for Design 2.

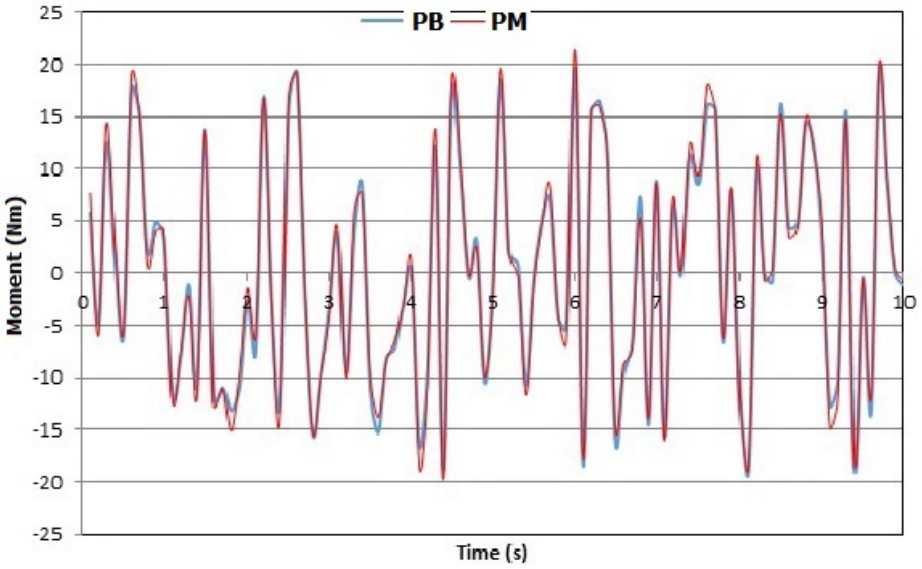

Figure 5.9. Parallel misaligned and perfectly bonded strain gage load signals M_y for Design 2.

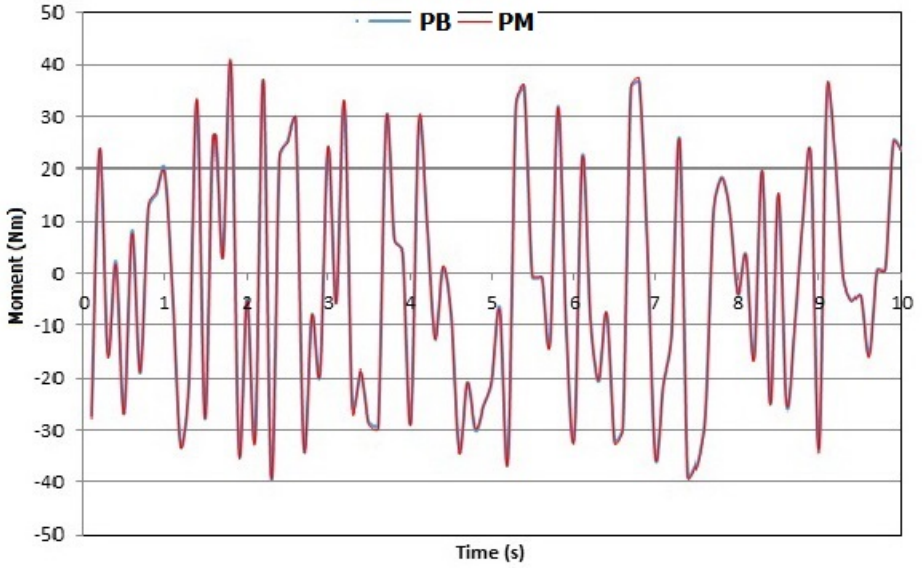

Figure 5.10. Parallel misaligned and perfectly bonded strain gage load signals M_x for Design 2.

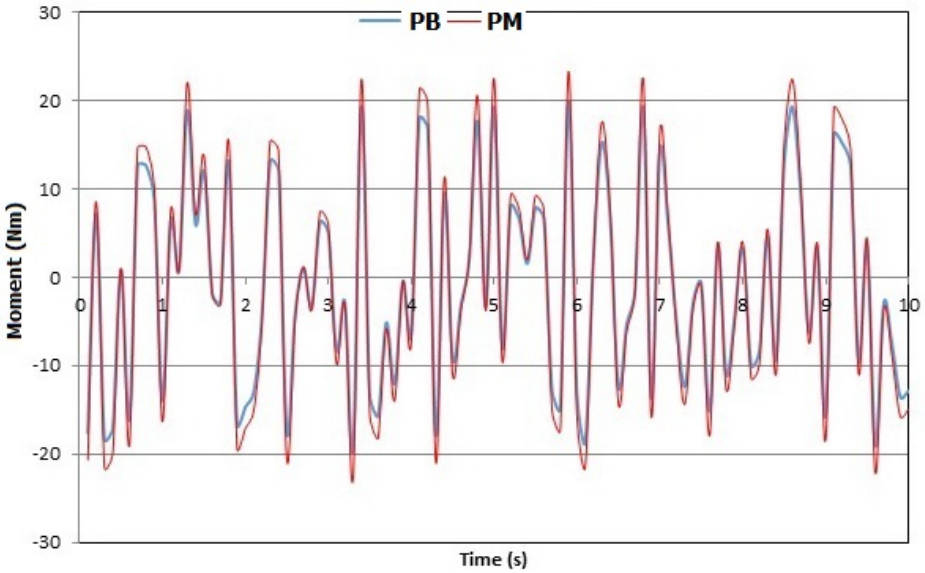

Figure 5.11. Parallel misaligned and perfectly bonded strain gage load signals M_z for Design 2.

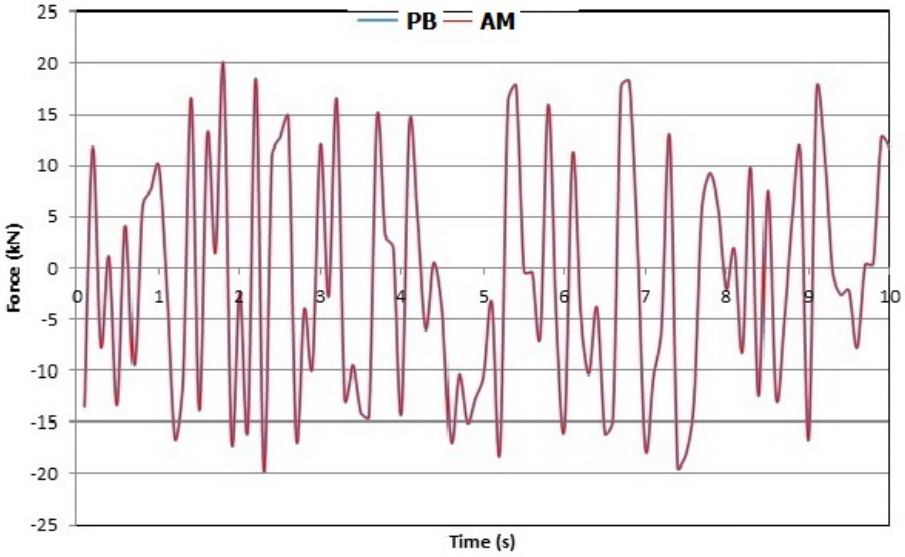

Figure 5.12. Angle misaligned and perfectly bonded strain gage load signals F_x for Design 2.

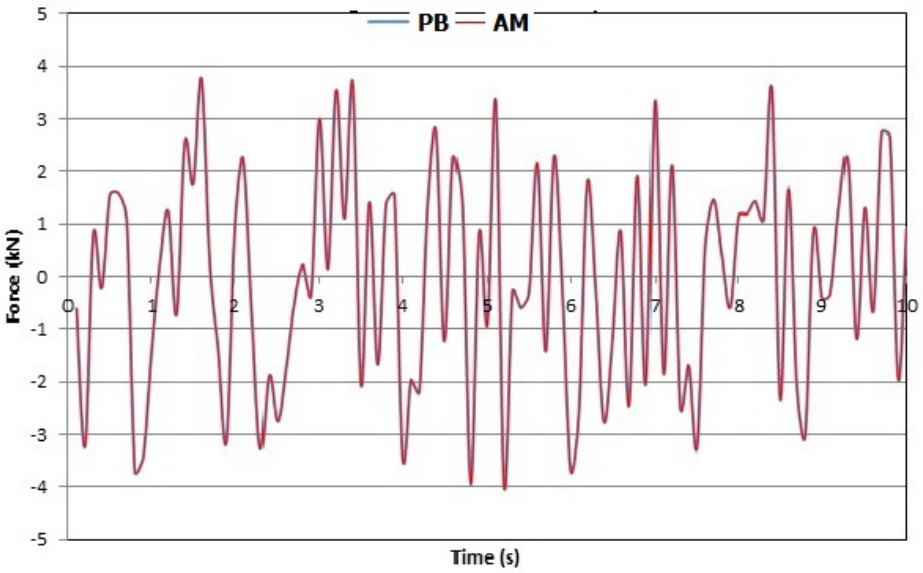

Figure 5.13. Angle misaligned and perfectly bonded strain gage load signals F_y for Design 2.

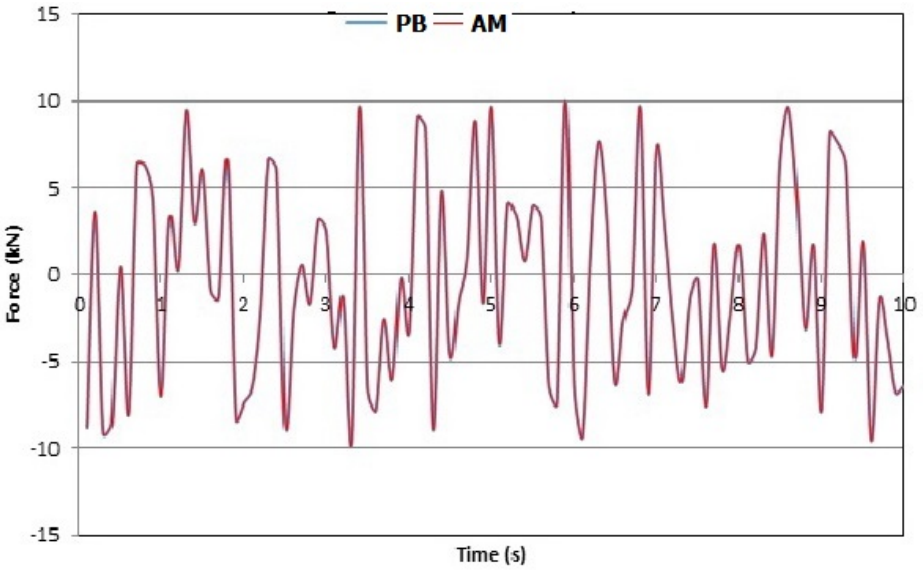

Figure 5.14. Angle misaligned and perfectly bonded strain gage load signals F_z for Design 2.

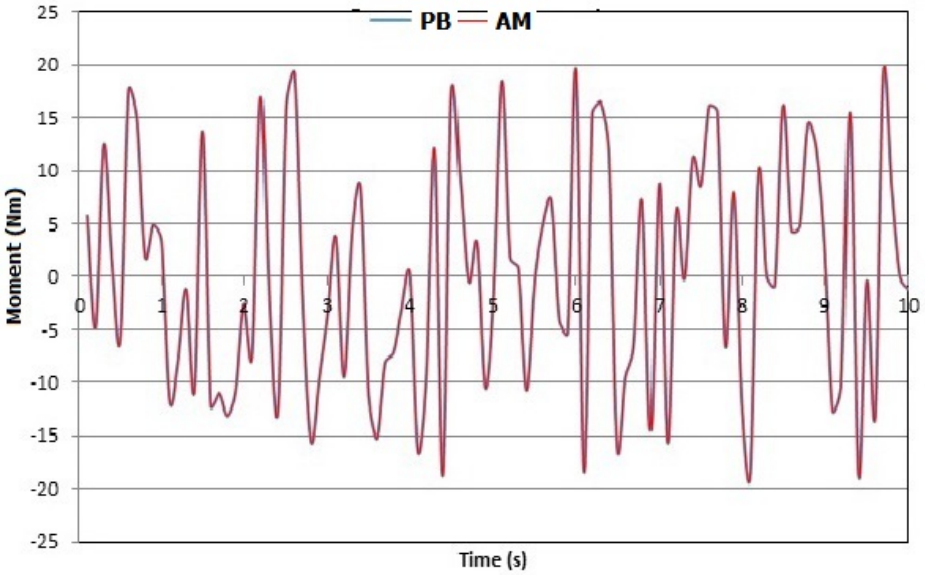

Figure 5.15. Angle misaligned and perfectly bonded strain gage load signals M_y for Design 2.

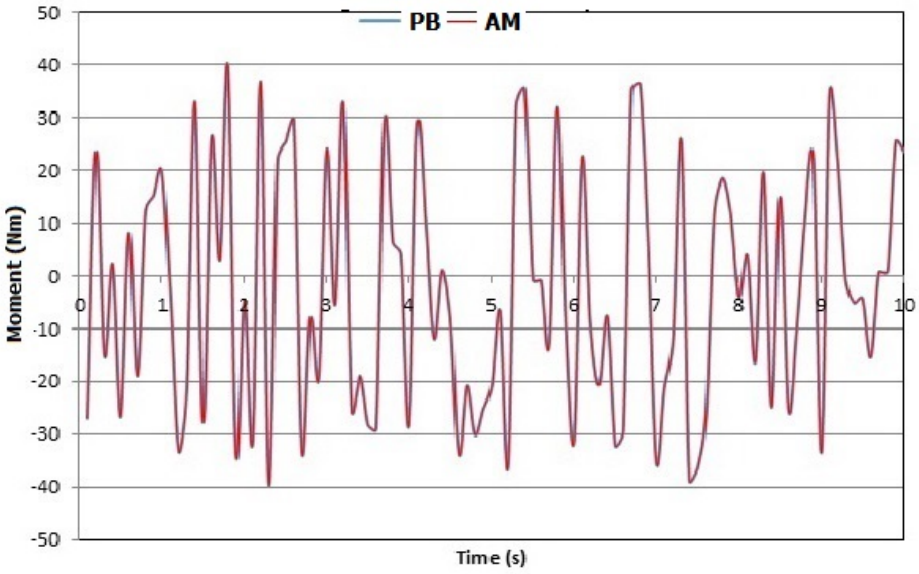

Figure 5.16. Angle misaligned and perfectly bonded strain gage load signals M_x for Design 2.

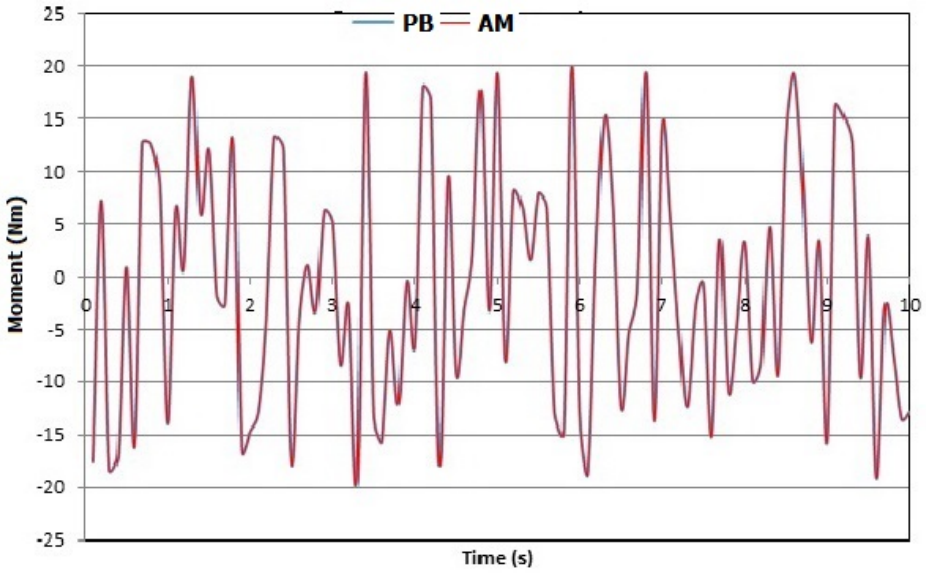

Figure 5.17. Angle misaligned and perfectly bonded strain gage load signals M_z for Design 2.

As we can see from the graphs, the amount of error received from the newly designed load cell, Design-2, has been decreased by an enormous amount especially in M_x and M_z measurements. The new design enhances the accuracy and sensitivity of strain measurement. It is also to be noted that the flexure features in Design-2 are chosen in a way which contributes to the accuracy, uniformity and reduction of transducer crosstalk between various channels in the load cell.

6. CONCLUSION AND FUTURE WORK

The use of a multi-axis load cell has been proposed to be used on specific parts of the engine mount of a vehicle in order to measure three components of force and three components of moment along three axis. Such an application requires a need for a multi-axis load cell that is simple and inexpensive to manufacture, that is unlikely to be damaged by widely varying loads, and that can be readily incorporated into engine mounts.

Two types of load cells have been designed which have been explained in this thesis. The first design has been manufactured and tested on a vehicle. The second design is an optimized version of the first one with slots added in order to reduce the crosstalk between the measuring channels and strain gage mounting errors.

The final elastic geometry of the load cell in this thesis has been compared with previous designs from literature regarding multi-axis load cells, which shows the novelty of this design as compared to other designs. Fatigue and error analysis have been carried out for both load cell designs and results obtained from analysis have been compared in order to better optimize the design of the load cell. Instead of a full bridge design due to the low strain values on walls of the bridges, bridges with a curvature shape has been use instead, which results in a localization of maximum strain values for different loads on the bridges. Stress concentrations are minimized and stress values are sufficient for infinite life. The body overall is simple, small and light-weighted comparing to other designs. Specially designed slots are added in the optimized design in order to reduce the interference error of bending moment when forces are applied along different axes.

The sources of errors obtained from error analysis are due to the misalignment of strain gage bonding and the slight misalignment of the fixtures used in order to mount the load cell to the servo-hydraulic testing machine. In order to minimize the errors the load cell has been optimized by adding slots at the end of the bridges on which

strain gages are bonded, which has given flexibility and has decreased the stiffness of the body of the load cell. Further optimizations can be carried out in the design by using different shapes for the bridges and slots in order to reduce error.

A special calibration fixture has been designed to reduce errors due to moments generated due to misalignment. This will result in the reduction of bending moments occurring when forces are applied on x and y axes. Effect of other sources of electrical and mechanical noise that influence the data received from the load cell, should also be considered in the order to improve the results which can be done in future work.

FORD-OTOSAN company has benefited from this thesis by using the basic design parameters of the load cell in order to design and manufacture other load cells similar to this one and used them in different vehicles. The results obtained from the tests have been satisfactory.

REFERENCES

1. Mettler, "Different Types Of Load Cells", `http://www.de.mt.com/`, Accessed May 2014.

2. Morris, A. S., *Measurement and Instrumentation Principles*, Butterworth-Heinemann, Sheffield, 2001.

3. Im Kang, D., G. S. Kim and H. K. Song, *6-Component Load Cell*, Mar. 30 1999, US Patent 5 889 214.

4. Meyer, R. A., *Multi-Axis Load Cell*, Mar. 21 2000, US Patent 6 038 933.

5. Lowe, A. E. and R. A. Meyer, *Multiple Axis Load Sensitive Transducer*, Feb. 3 1987, US Patent 4 640 138.

6. Drake, S. H. and P. C. Watson, *Method and Apparatus for Six Degree of Freedom Force Sensing*, Jun. 13 1978, US Patent 4 094 192.

7. Chao, L.-P. and K.-T. Chen, "Shape Optimal Design and Force Sensitivity Evaluation of Six-Axis Force Sensors", *Sensors and Actuators A: Physical*, Vol. 63, No. 2, pp. 105–112, 1997.

8. Joo, J., K. Na and D. Kang, "Design and Evaluation of a Six-Component Load Cell", *Measurement*, Vol. 32, No. 2, pp. 125–133, 2002.

9. ANSYS, *DesignLife Theory Guide*, 2000.

10. Ansys, "The Five-Box Trick in an ANSYS nCode DesignLife Fatigue Simulation", `http://www.ansys-blog.com/`, Accessed May 2014.

11. K. Krishnaswamy, S. V., *Industrial Instrumentation*, New Age International Limited, Mumbai, 2005.

12. C. S. Rangan, V. S. V. M., G. R. Sarma, *Instrumentation: Devices Systems*, Tata McGraw-Hill, Mumbai, 2006.

13. OmegaCo, "Introduction to Load Cells", `http://www.omega.com/`, Accessed May 2014.

14. Matsuoka, Y. and M. Shimazoe, *Load Cell*, Jun. 19 1984, US Patent 4 454 771.

15. Shi, W. and S. D. Hall, "A Novel Six Axis Force Sensor for Measuring the Loading of a Racing Tyre on Track", *Proceedings of the First International Conference on Sensing Technology*, 2005.

16. Carignan, F. J. and N. H. Cook, *Force Measuring Platform and Load Cell Therefor Using Strain Gages to Measure Shear Forces*, Jan. 15 1985, US Patent 4 493 220.

17. Declercq, S., D. Lazor and D. Brown, "A Smart 6-DOF Load Cell Development", *Proceedings, International Modal Analysis Conference*, pp. 844–853, 2002.

18. Wohler, "Wöhler Fatique Curves (S-N) for Shearing Stress", `http://www.brighthubengineering.com/`, Accessed May 2014.

19. Weibull, "Miner's Rule and Cumulative Damage Models", `http://www.weibull.com/hotwire/issue116/hottopics116.htm`, Accessed May 2014.

20. Gobbi, M., G. Previati, P. Guarneri and G. Mastinu, "A New Six-Axis Load Cell. Part II: Error Analysis, Construction And Experimental Assessment of Performances", *Experimental mechanics*, Vol. 51, No. 3, pp. 389–399, 2011.

21. Kempainen, A., R. Meyer and D. Olson, *Multi-Axis Load Cell Body*, Jul. 17 2001, US Patent 6 769 312.

22. Zipin, R. B., *Multi-Axis Load Cell*, Feb. 24 1976, US Patent 3 939 704.

23. Fraignier, B. and D. E. Gery, *Multi Axis Force And Moments Transducer*, Nov. 5 1985, US Patent 4 550 617.

24. Meyer, R. A. and D. J. Olson, *Load Transducer*, Apr. 18 1989, US Patent 4 821 582.

25. Larson, B. A., R. A. Meyer, D. J. Olson and J. L. Sommerfeld, *Multi-Axis Load Cell*, Oct. 19 1999, US Patent 5 969 268.

26. Meyer, R. A. and D. J. Olson, *Six Axis Load Cell*, May 31 1994, US Patent 5 315 882.

27. Meyer, R. A., A. J. Kempainen and D. J. Olson, *Multi-Axis Load Cell Body*, Aug. 3 2004, US Patent 6 769 312.

28. Meyer, R. and A. Kempainen, *Multi Axis Load Cell Body*, Nov. 23 2005, US Patent 11 286 697.

29. McDearmon, G. F., D. R. Leeper, D. H. Walter and D. H. Smith, *Multiaxis Ring Load Cell*, Sep. 21 2004, US Patent 6 792 815.

30. Mastinu, G., M. Gobbi and G. Previati, "A New Six-Axis Load Cell. Part I: Design", *Experimental mechanics*, Vol. 51, No. 3, pp. 373–388, 2011.

31. Kim, G.-S. and H.-D. Lee, "Development of a Six-Axis Force/Moment Sensor and Its Control System for an Intelligent Robot's Gripper", *Measurement Science and Technology*, Vol. 14, No. 8, p. 1265, 2003.

32. F.S. Bourgeois, G. B., *A Portable Load Cell For In-Situ Ore Impact Breakage Testing*, 2002.

33. Darrell F. Socie, G. B. M., *Multiaxial Fatigue*, 2000.

34. UddeholmCo, "Uddeholm Alvar 14 Material Safety Data Sheet",

http://www.uddeholm.com/, Accessed June 2014.

35. Dowling, N. E., *Mechanical Behavior of Materials*, 2012.

36. Liu, S. A. and H. L. Tzo, "A Novel Six-Component Force Sensor of Good Measurement Isotropy and Sensitivities", *Sensors and Actuators A: Physical*, Vol. 100, No. 2, pp. 223–230, 2002.